Computers in Biology and Medicine 155 (2023) 106596

Contents lists available at ScienceDirect

Computers in Biology and Medicine

journal homepage: www.elsevier.com/locate/compbiomed

Mechanistic insights of *Cucumis melo* L. seeds for gastrointestinal muscle spasms through calcium signaling pathway–related gene regulation networks in WGCNA and *in vitro*, *in vivo* studies

Muqeet Wahid [a], Fatima Saqib [a,*], Saeed Akhtar [b], Anam Ali [a], Trina Ekawati Tallei [c], Jesus Simal–Gandara [d,**]

[a] Department of Pharmacology, Faculty of Pharmacy, Bahauddin Zakariya University, Multan, 60000, Pakistan
[b] Institute of Food Science and Nutrition, Bahauddin Zakariya University, Multan, 60000, Pakistan
[c] Department of Biology, Faculty of Mathematics and Natural Sciences, Sam Ratulangi University, Manado, 95115, North Sulawesi, Indonesia
[d] Universidade de Vigo, Nutrition and Bromatology Group, Analytical Chemistry and Food Science Department, Faculty of Science, E32004, Ourense, Spain

ARTICLE INFO

Keywords:
Cucumis melo
Irritable bowel syndrome
Antidiarrheal
WGCNA
LC ESI MS/MS

ABSTRACT

Background: In addition to the nutritional benefits of *Cucumis melo* L., herbalists in Pakistan and India employ seeds to treat various ailments. This study aimed to determine the regulatory role of *C. melo* seeds in calcium-mediated smooth muscle contraction.
Methods: We identified and quantified the phytochemicals of *C. melo* with LC ESI–MS/MS and HPLC, then conducted *in vitro* and *in vivo* tests to confirm the involvement in smooth muscle relaxation. Then, diarrhea-predominant irritable bowel syndrome gene datasets from NCBI GEO were acquired, DEGs and WGCNA followed by functional enrichment analysis. Next, molecular docking of key genes was performed.
Results: The quantification of *C. melo* seeds revealed concentrations of rutin, kaempferol, and quercetin were 702.38 μg/g, 686.29 μg/g, and 658.41 μg/g, respectively. *In vitro* experiments revealed that *C. melo* seeds had a dose-dependent relaxant effect for potassium chloride (80 mM)–induced spastic contraction and exhibited calcium antagonistic response in calcium dose-response curves. In *in vivo* studies, Cm.EtOH exhibited antidiarrheal, antiperistaltic, and antisecretory effects. The functional enrichment of WGCNA and DEGs IBS-associated pathogenic genes, including those involved in calcium-mediated signaling, MAPK cascade, and inflammatory responses. MAPK1 and PIK3CG were identified as key genes with greater binding affinity with rutin, quercitrin, and kaempferol in molecular docking.
Conclusions: The bronchodilator and antidiarrheal effects of *C. melo* were produced by altering the regulatory genes of calcium-mediated smooth contraction.

1. Introduction

The irritable bowel syndrome (IBS) is an inflammatory digestive disorder that may be caused by several factors, such as intestinal motility and gut flora changes [1]. The disease can affect anyone, but it mainly affects women under 50 and between 5 and 15% of the Western population [2]. The symptoms of IBS include stomach pains, bloating, urgency, and a feeling of incomplete evacuation. In patients suffering from IBS, there are no indications of organic or metabolic problems. However, their quality of life (QoL) may be negatively affected, as well as their daily ability to work and participate in activities [2]. Several factors are associated with this condition, including changes in gastrointestinal motility, visceral hypersensitivity, SIBO, and intestinal microbiota [2,3].

Cucumis melo Linn belongs to the family Cucurbitaceae; its common name is muskmelon [4]. It is extensively cultivated worldwide as an edible fruit or vegetable [5,6]. *C. melo* is a nutritious and therapeutic fruit with a delicious taste. Due to its high nutritional value, *C. melo* fruit can be consumed fresh, canned, or processed. The pulp of *C. melo* is commonly eaten in the desert, in salads, raw or roasted [6,7]. It has been used in traditional medicine for centuries in Pakistan, Iran, India, and

* Corresponding author.
** Corresponding author.
E-mail addresses: muqeetsoomro@msn.com (M. Wahid), fatima.saqib@bzu.edu.pk (F. Saqib), saeedbzu@yahoo.com (S. Akhtar), anam.ali@live.in (A. Ali), trina_tallei@unsrat.ac.id (T.E. Tallei), jsimal@uvigo.es (J. Simal–Gandara).

https://doi.org/10.1016/j.compbiomed.2023.106596
Received 28 November 2022; Received in revised form 26 December 2022; Accepted 22 January 2023
Available online 2 February 2023

Abbreviations

CCB	Calcium channel blocker
CCh	Carbachol
Cm.EtOH	hydroethanolic extract of *C. melo* seed
DEGs	Differentially expressed genes
DRC	Dose–response curves
FA	Formic acid
GSEA	Gene Set Enrichment Analysis
GO	Gene Ontology
KEGG	Kyoto Encyclopedia of Genes and Genomes
pKi	Predicted Log of Inhibition Constant (Ki)
MM–GBSA	molecular mechanics energies combined generalized Born and surface area
TFA	Trifluoroacetic acid
WGCNA	Weighted Gene Co–expression Network Analysis

China for gastrointestinal, circulatory, neurological, and urogenital problems [8–11]. This study aims to determine whether *C. melo* seeds have antispasmodic properties and identify how calcium-mediated signaling pathways control smooth muscle contraction genes [12,13].

2. Materials and methods

2.1. Preparation of extract

Cucumis melo L seeds and fruit were verified and validated by a botanist from Bahauddin Zakariya University, Multan (60000), Pakistan, during the summer of 2018, obtained from the pulp of the locally framed fruits. A voucher specimen (Sp. Pl. 1011–1753) was placed at the herbarium of the Institute of Biology and Applied Sciences, Bahauddin Zakariya University, Multan (60000), Pakistan. The inner portion of the seeds was manually separated from the husk and processed into a coarse powder using an herbal grinder, then processed in a Soxhlet system using hydroethanolic (70:30) solvent at boiling point for 24 ± 2 h. Solvents were evaporated under reduced pressure at 35 ± 3 °C

Table 1
Identification of phytoconstituents of Cm.EtOH with LC ESI-MS/MS.

Sr. No	Molecular Weight	Observed MS (*m/z*)	Calculated MS (*m/z*)	Error	Proposed compound	Empirical Formula	ESI–IT MS/MS (Ions)	Precursor type	Class
1.	516.4	515.013	515.0119	−2.14	1,4–Dicaffeoylquinic acid	$C_{25}H_{24}O_{12}$	471, 353, 317, 299.25, 255, 203, 179	[M − H]–	Quinic acids
2.	270.24	269.0455	269.0445	−3.72	Apigenin	$C_{15}H_{10}O_5$	269, 255, 151, 117, 107	[M − H]–	Flavonoids
3.	180.16	179.0359	179.0353	−3.35	Caffeic acid	$C_9H_8O_4$	179.17, 135, 107	[M − H]–	Hydroxycinnamic acids
4.	290.27	289.0717	289.0719	0.7	Epicatechin	$C_{15}H_{14}O_6$	290, 289.08, 245.08, 179.08, 165.08, 151.08	[M − H]–	Catechin/ Flavonoids
5.	194.18	193.0505	193.0506	0.52	Ferulic acid	$C_{10}H_{10}O_4$	193, 178, 164, 133, 117	[M − H]–	Cinnamic acids
6.	172.18	503.1617	503.1615	−0.4	Glycyl–l–proline	$C_7H_{12}N_2O_3$	171, 127, 114, 98	[M − H]–	Amino acids derivatives
7.	610.6	609.1817	609.1812	−0.82	Hesperidin	$C_{28}H_{34}O_{15}$	609, 301, 285, 151	[M − H]–	Flavonoid glycosides
8.	286.23	285.0397	285.0395	−0.70	Kaempferol	$C_{15}H_{10}O_6$	285, 215, 185, 164, 153, 151,117	[M − H]–	Flavanols
9.	448.38	447.0943	447.0948	1.12	kaempferol–3–O–glucoside	$C_{21}H_{20}O_{11}$	447.09, 285, 271,219, 193, 179, 151	[M − H]–	Flavonoid glycosides
10.	286.24	285.0402	285.0405	1.05	Luteolin	$C_{15}H_{10}O_6$	285, 175, 169, 151, 133,	[M − H]–	Flavones
11.	448.37	447.0938	447.0931	−1.57	Luteolin 7–O–glucoside	$C_{21}H_{20}O_{11}$	447, 285.08, 256, 217, 151.17	[M − H]–	Flavonoid glycosides
12.	134.09	133.0142	133.0138	−3.01	Malic acid	$C_4H_6O_5$	133, 115, 89, 71	[M − H]–	Carboxylic acid
13.	624.54	623.1628	623.1615	−2.09	Narcissin/Isorhmnetin 3–O–rutinoside	$C_{28}H_{32}O_{16}$	623,315, 300, 271, 285, 255, 151	[M − H]–	Flavonoid glycosides
14.	164.16	163.0401	163.0406	3.07	p–coumaric acid	$C_9H_8O_3$	163.0, 119, 93, 87,	[M − H]–	Hydroxycinnamic acids
15.	302.23	301.0354	301.0349	−1.66	Quercetin	$C_{15}H_{10}O_7$	301.08, 273.08, 179, 151, 121,107	[M − H]–	Flavonoid
16.	192.17	191.0573	191.0576	1.6	Quinic acid	$C_7H_{12}O_6$	191,173, 171, 127, 93, 85	[M − H]–	carboxylic acid
17.	610.5	609.1422	609.142	−0.33	Rutin	$C_{27}H_{30}O_{16}$	609.25, 301.08, 299, 271, 255, 178	[M − H]–	Flavonoid glycosides
18.	412.69	413.8459	413.8467	1.93	Stigmasterol	$C_{29}H_{48}O$	397, 379, 355, 342.1, 297,	[M+H]+	Sterol
19.	162.14	161.0251	161.0249	−1.24	Umbelliferone	$C_9H_6O_3$	161, 133, 123, 117, 97	[M − H]–	Hydroxycoumarins
20.	430.71	431.3886	431.3883	−0.70	α–tocopherol	$C_{29}H_{50}O_2$	432,166, 163, 165, 136,	[M+H]+	Fat–soluble vitamin

Table 2
HPLC Quantification and technique validation of Cm.EtOH for phytochemicals.

Analytes	Wavelength (nm)	Rt (mins)	Linear Regression Data			LOD (μg/ml)	LOQ (μg/ml)	Concentration (μg/g)	Precision (RSD %)		Recovery		Analytes + Cm. EtOH (μg/g)	
			Range (μg/ml)	Equation	r^2				Inter Day	Intra Day	Mean	RSD %	50 μg	100 μg
Stigmasterol	250	18.2	7.81–500	y = 102.98x + 14.70	0.9996	0.95	2.89	289.31	1.48	1.84	99.29 ± 0.48	0.91	338.77	388.57
Umbelliferone	280	5.3	7.81–500	y = 223.13x + 32.28	0.9995	0.88	2.70	263.53	0.85	0.71	99.47 ± 1.12	0.66	313.03	362.84
Caffeic acid		8.3	7.81–500	y = 209.8x + 20.557	0.9999	0.54	1.64	280.16	0.90	1.14	98.79 ± 1.09	0.67	329.63	379.44
Rutin		9.7	7.81–500	y = 199.98x + 23.31	0.9994	0.67	2.02	702.38	1.31	0.30	99.16 ± 0.49	1.87	751.18	800.86
Luteolin		12.4	7.81–500	y = 206.75x + 33.60	0.9993	0.98	2.98	539.12	0.82	1.49	99.45 ± 0.21	0.84	588.18	637.91
Quercetin		13.8	7.81–500	y = 219.58x + 17.27	0.9999	0.41	1.24	658.41	1.34	1.28	98.53 ± 0.86	1.76	707.31	757.01
Apigenin		17.7	7.81–500	y = 143.75x + 25.94	0.9998	1.10	3.35	456.10	1.35	1.33	99.51 ± 0.57	0.59	505.29	555.04
Kaempferol		19.4	7.81–500	y = 203.17x + 20.12	0.9992	0.35	1.05	686.29	1.28	1.75	99.39 ± 0.45	0.83	735.13	784.82
Ferulic acid		21.9	7.81–500	y = 179.53x + 35.80	0.9999	1.24	3.75	344.89	1.07	1.62	98.99 ± 0.87	0.81	394.26	444.04
1,4-Dicaffeoylquinic acid	320	7.2	7.81–500	y = 170.17x + 22.32	0.9996	0.77	2.32	575.61	0.49	1.83	98.86 ± 0.81	1.05	624.61	674.33

All values are mean ± S.D., $n = 3$ for three days.

through rotary evaporation to produce yellowish-brown greasy extracts. The overall yield of *C. melo* seed extract (Cm.EtOH) was 53%. The dried extract thus obtained was stored at −20 °C in an amber glass jar and was later screened for its pharmacological properties. On the day of the experiment, distilled water or normal saline was used to dissolve and dilute the extract to the required concentration.

2.2. Phytochemical analysis

The phytochemical analysis of *C. melo* hydroethanolic extract was determined, characterized, and quantified by LC/ESI-MS/MS and HPLC based on parameters and thresholds discussed in previous publications [14,15].

2.2.1. Preparation of samples

An amount of 1.0 mL of 100% methanol (MeOH) was mixed with Cm.EtOH to prepare samples for chromatographic analysis. We centrifuged the mixture for 12 min at 14,000 rpm and then filtered the supernatant with a 0.22 μm syringe filter.

2.2.2. LC ESI–MS/MS analysis

Cm.EtOH was investigated using LC ESI–MS/MS to determine their phytoconstituents [12]. We injected the sample directly into an ESI probe configured for positive and negative ions. The mobile phases for Cm.EtOH, made up of Solvent A, contains 0.1% formic acid (FA) in MeOH, and Solvent B, which contains 0.1% FA in acetonitrile (ACN) and water (20:80), respectively. Other optimal chromatographic and mass spectroscopic parameters are detailed in earlier reports [14,15].

2.2.3. RP–HPLC quantification and method validation

We performed HPLC analysis to confirm and quantify the phytoconstituents of Cm.EtOH [15,16]. The mobile phases for Cm.EtOH consisted of Solvent-A, which contains 0.1% trifluoroacetic acid (TFA) in MeOH, and Solvent-B contains 0.1% TFA with ACN and water (20:80), respectively. Other optimal chromatographic and analytical method validation are detailed in our previous publications [14,15].

2.3. Ethical committee provision

The animal ethical committee of the Department of Pharmacology permitted the experimental methods for animal studies to vide E.C./04PhDL/S2018. The research was conducted following the Commission on Laboratory Animal Resources [47]. We used albino rabbits weighted 1.26–1.65 kg, Sprague–Dawley rats weight 155–180 g) and albino mice of weight 17–26 g throughout this study. For *in vitro* and *in vivo* testing, rats and mice were dislocated at the cervical spine, and rabbits were sacrificed with a sharp knife. Animals were housed in controlled conditions with a standard prescribed diet.

2.4. Isolated tissue experimentation for smooth muscle contraction

For *in vitro* investigations, we followed the protocols of Saqib and Janbaz [17] and Wahid et al. [16]. We recorded the physiological response of the tissue with an isotonic and isometric transducer.

2.4.1. Isolated rabbit jejunum preparations

Jejunum portions were dissected and placed in a tissue organ containing Tyrode's solution continuously recirculated with the carbogen at 37 ± 0.5 °C to keep them alive and ready for use under preload tension of 1 g. Before administering the Cm.EtOH, the jejunum tissue was equilibrated for 25 ± 5 min. Test samples (extracts) were applied to the bath solution containing the jejunum tissue. The decrease in spontaneous rhythmic contractions for each tested sample was measured with repeated flushes of Tyrode solution every 10 min [18]. As reported previously, the calcium-mediated signaling pathways are involved in smooth muscle contraction by triggering the calcium ion channel closing

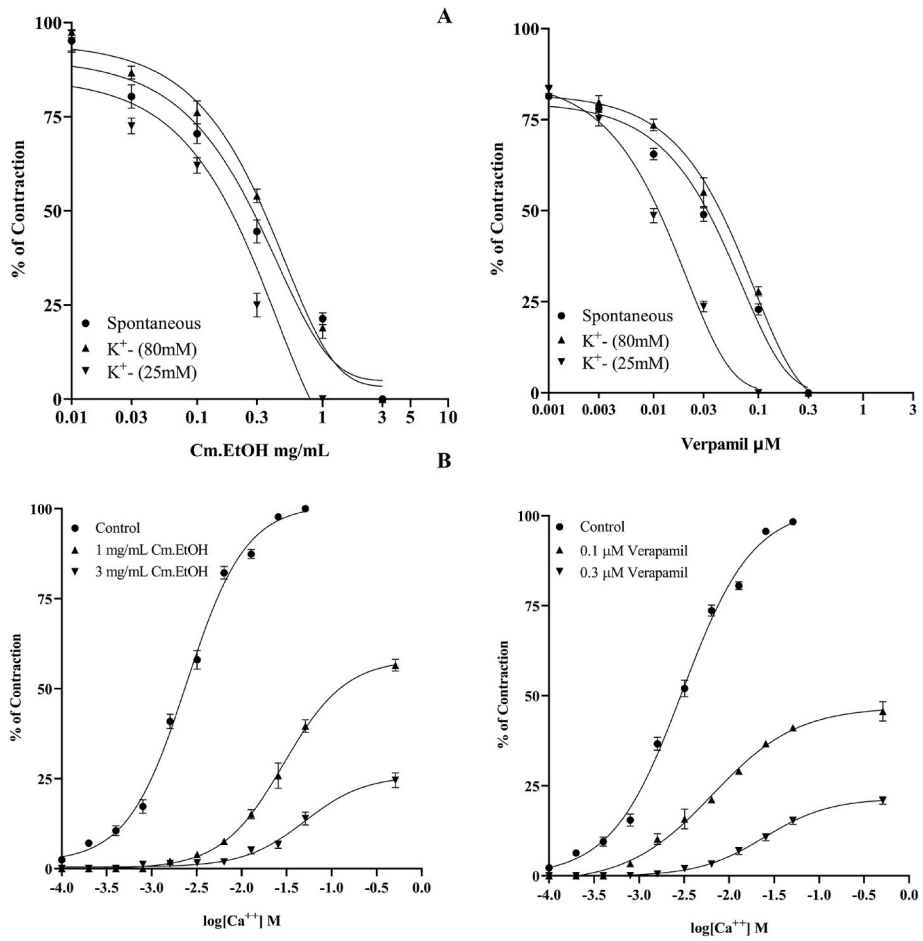

Fig. 1. In jejunal tissue preparations, Cm.EtOH and verapamil inhibit smooth muscle contraction. **A.** Verapamil and Cm.EtOH inhibits potassium chloride (K+; 80 mM and 25 mM)-induced spasms. **B.** DRCs of calcium in the presence and absence of verapamil and Cm.EtOH.

or the potassium channel opening [19]. The potassium chloride (80 mM) initiated the closing of the calcium ions channel, and the potassium ions channel was opened with potassium chloride (25 mM) [12,17]. The potassium chloride (80 mM) depolarizes the cells and induces a calcium ions influx, which may alter smooth muscle contraction. The extract may be categorized as a calcium channel blocker if it inhibits these contractions [20]—the doses of Cm.EtOH was successively administered to establish an inhibitory effect.

In addition, the calcium antagonistic properties of Cm.EtOH was examined. The preparation of jejunal tissue was pretreated with potassium chloride (80 mM), subsequently incubated in an EDTA Tyrode solution for 30 ± 7 min, and incubated for 55 ± 7 min in calcium-free Tyrode solution that is rich with potassium to reduce or diminish intracellular calcium concentrations. Following incubation, doses of calcium were gradually added to produce superimposable control calcium dose-response curves (DRCs), then calcium DRCs were produced in Cm.EtOH pretreated jejunal preparations [20].

2.4.2. Isolated rabbit tracheal preparations

We dissected the rabbit tracheal tissue, removed the adherent substances, formed the 2–3 mm wide rings, and each ring was incised longitudinally to produce sandwich smooth muscle tracheal strip preparation. Each preparation was placed in a Krebs buffer–filled tissue organ bath (pH 7.4) continuously circulated with carbogen at 37 ± 0.5 °C, under the tension of 1 g. Before administering Cm.EtOH, the tracheal preparation was stabilized for 55 ± 10 min. The bronchodilator activity of Cm.EtOH was studied with potassium chloride (80 and 25 mM) and CCh (1 µM). A dose-dependent inhibitory response was established by cumulative administration of Cm.EtOH. The preparation of tracheal tissue was treated with CCh (1 µM), then incubated for 55 ± 10 min in normal Kreb's solution. Following the incubation of the tissue preparation, carbachol was gradually administered to obtain carbachol dose-response curves (DRCs). Carbachol DRCs are produced after 55 ± 10 min of incubation with Cm.EtOH. To ascertain the presence of muscarinic receptor antagonism action, these carbachol DRCs of Cm. EtOH were compared to control carbachol DRCs [20].

2.4.3. Isolated urinary bladder preparations

We dissected rabbit urinary bladder tissue, removed the adherent substances, and formed 2–3 cm wide strips. Each preparation was placed in a Krebs buffer–filled tissue organ bath continuously gassed with carbogen at 37 ± 0.5 °C, under the tension of 1 g. Before administering the test drug, the tissue preparation was equilibrated for 55 ± 5 min—the dysuria activity of Cm.EtOH was studied with potassium chloride (80 and 25 mM) and CCh (1 µM). A dose-dependent inhibitory response was established by cumulative administration of Cm.EtOH. In addition, the calcium antagonistic properties of Cm.EtOH was examined. The preparation of bladder tissue was pretreated with potassium chloride (80 mM), subsequently incubated in an EDTA Tyrode solution for 30 ± 7 min, and incubated for 55 ± 7 min in calcium-free Tyrode solution that is rich with potassium to reduce or diminish intracellular calcium concentrations. Following incubation, doses of calcium were gradually added to produce superimposable control calcium dose-response curves (DRCs), then calcium DRCs were produced in Cm.EtOH pretreated bladder preparations [20].

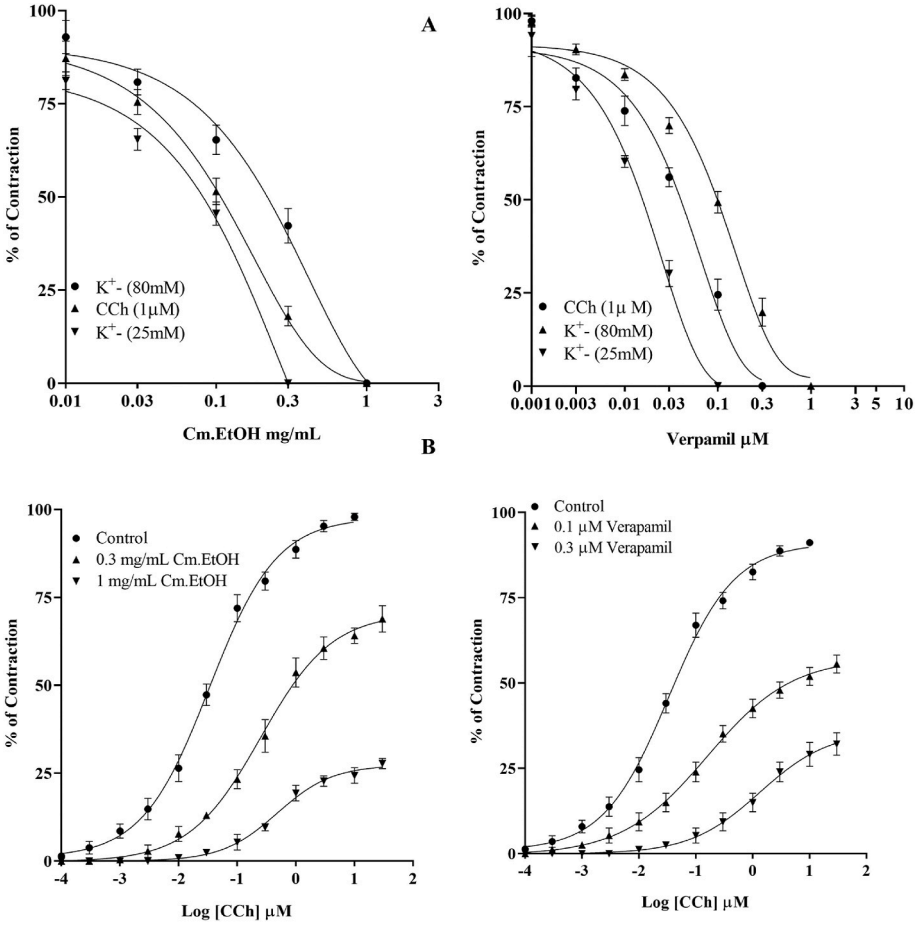

Fig. 2. In tracheal tissue preparations, Cm.EtOH and verapamil inhibit smooth muscle contraction. **A.** Verapamil and Cm.EtOH inhibits potassium chloride (K+; 80 mM and 25 mM)-induced spasms. **B.** DRCs of carbachol in the presence and absence of verapamil and Cm.EtOH.

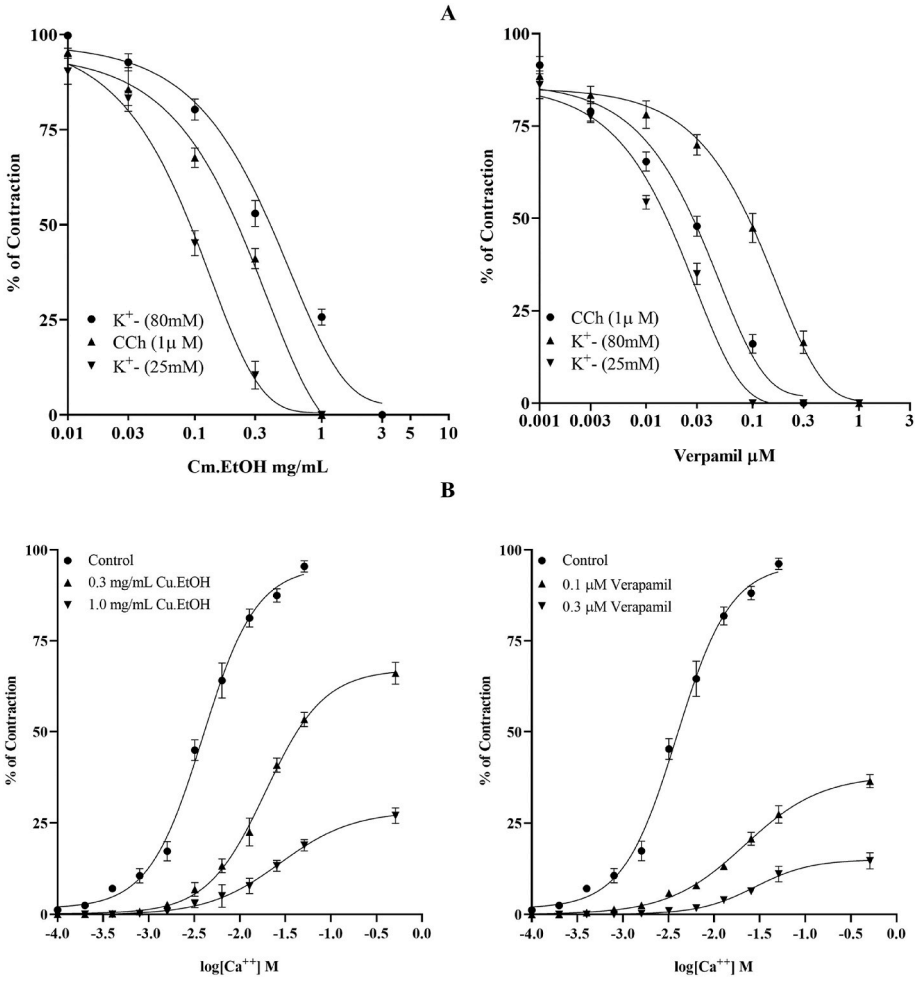

Fig. 3. In urinary bladder tissue preparations, Cm.EtOH and verapamil inhibit smooth muscle contraction. **A.** Verapamil and Cm.EtOH inhibits potassium chloride (K+; 80 mM and 25 mM)-induced spasms. **B.** DRCs of calcium in the presence and absence of verapamil and Cm.EtOH.

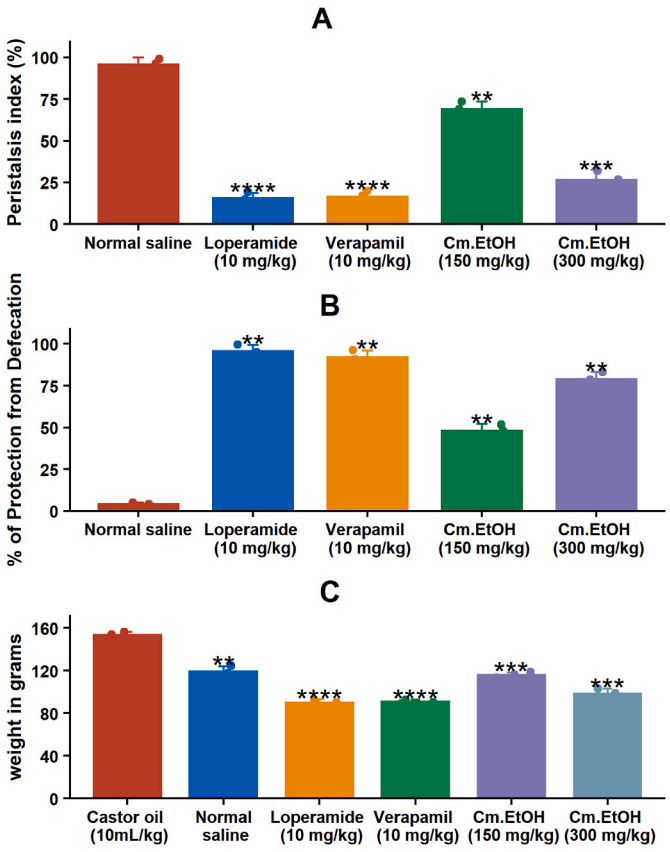

Fig. 4. Gastrointestinal activities of in-vivo activities of Cm.EtOH. **A.** Antiperistalsis, **B.** antidiarrheal activity, and **C.** G.I. fluid accumulation activity of verapamil, loperamide, and Cm.EtOH. Data are expressed as the mean ± S.D. (n = 4). Student t-test was performed to determine significance when compared to control; $p < 0.05$; *$p < 0.01$, **$p < 0.001$, ***$p < 0.0001$, ****$p < 0.00001$ were used to determine significance).

2.5. In vivo experimentation

2.5.1. Evaluation of maximum tolerated dose

In a study to determine the maximum tolerated dose, Cm.EtOH was administered orally to rats at doses of 50, 100, 150, 200, and 300 mg/kg per day for 28 days. The control rats were given saline. During the 28-day study, death rates, body weights, behavioral changes, and clinical signs of discomfort were all recorded [21].

2.5.2. Protocol and design

Mice were grouped randomly into six groups, five animals of either sex per group. Before the trial, water was freely available to all groups, but the food was withdrawn for 10 ± 3 h.

Group I was orally administrated with normal saline (10 mL/kg).

Group II was orally administrated with castor oil or charcoal meal.

Groups III and IV were orally administrated with 10 mg/kg of verapamil and loperamide.

Group V and VI were orally administrated with 150 and 300 mg/kg of Cm.EtOH.

2.5.3. Charcoal meal G.I. Transit test

The antiperistalsis activity [17] of Cm.EtOH, all animals received the charcoal meal orally after 15 min except Group I. Animals were sacrificed after 30 min, and their small intestines were excised to estimate the distance traveled by charcoal. The percentage of the peristaltic index was calculated.

2.5.4. Castor oil-induced diarrhea

Castor oil–induced diarrheal activity [16] of Cm.EtOH; all animals received the castor oil orally after 30 min except Group I. After 6–7 h, wet fecal spots were observed on white paper. The percentage of protection for defecation was calculated.

2.5.5. Castor oil–induces intestinal fluid accumulation

In the antisecretory activity [44] of Cm.EtOH, mice in all groups received the castor oil orally after 15 min except for Group I. Animals were sacrificed after 30 min and ligated pylorus and caecum ends of the small intestine before being removed. The weight of the small intestine with and without intestinal fluid was monitored. The amount of fluid accumulated (g) was determined by weighing the fluid accumulated in the intestine.

2.6. WGCNA and DEGs studies

2.6.1. Data download and preprocessing

Irritable bowel syndrome trait datasets GSE14841 and GSE14842 were acquired using the NCBI GEO (https://www.ncbi.nlm.nih.gov/geo/). The coefficient of variation was calculated after normalizing both datasets and eliminating the expression of genes with low expression levels.

2.6.2. Differentially expressed genes

We used R package "Limma" (v3.52) to evaluate differentially expressed genes (DEGs) for both datasets along with subsequent contrasts: diarrhea group versus healthy group for GSE14841, diarrhea group versus control group, and diarrhea group versus treated diarrhea group for GSE14842 with log2 fold-change thresholds of ≥0.2, & 1, and p-value of ≥0.05. We plotted results using the R package ggplot2(v3.3). In the following step, we determined the top 15 DEG genes and separated them into groups based on the *hclust* method.

2.6.3. Weighted correlation network analysis

Identification of modules: We used the R package WGCNA (v1.70) to analyze GSE14841 and GSE14842 datasets for coexpression networks. The expressions of all genes were grouped using hclust to eliminate outliers. A Pearson test was used to create an adjacency matrix, and a paired gene expression similarity matrix was generated. The scale-free gene coexpression topological approach was used to evaluate the adjacency matrix at the lowest possible soft-threshold values. We constructed dissimilarity TOM (dissTOM) and topological overlap matrices (TOM) to assess gene expression profiles. A minimum module size of 30 was calculated to define the co-expressed genes modules. The modules with high similarity scores are combined at a threshold of 0.25.

Construction of module–trait relationships: We identified modules with a strong correlation to clinical characteristics following Module Eigengene (ME). Gene expression for each module was associated with its primary component as an eigenvector. An eigengene is the average gene expression pattern that represents the central element of a module.

Detection of hub genes: We analyzed gene significance scores (GS) to identify asthma-associated gene expressions. Each gene expression was assigned a module membership (MM) to determine the correlation between ME and gene expression. The most significant genes in the modules are strongly associated with GS and MM, suggesting they are strongly associated with clinical characteristics. In addition, they can be used to identify module hub genes as well as create network diagrams.

2.6.4. Functional annotations and pathways enrichment

The functional gene ontology (GO) and pathways annotations of WGCNA modules and DEGs genes of each dataset were examined using the R package Cluster Profiler (v4.4) with an FDR of ≤0.05 threshold.

2.6.5. Gene set enrichment analysis (GSEA)

A GSEA analysis was conducted to determine the biological

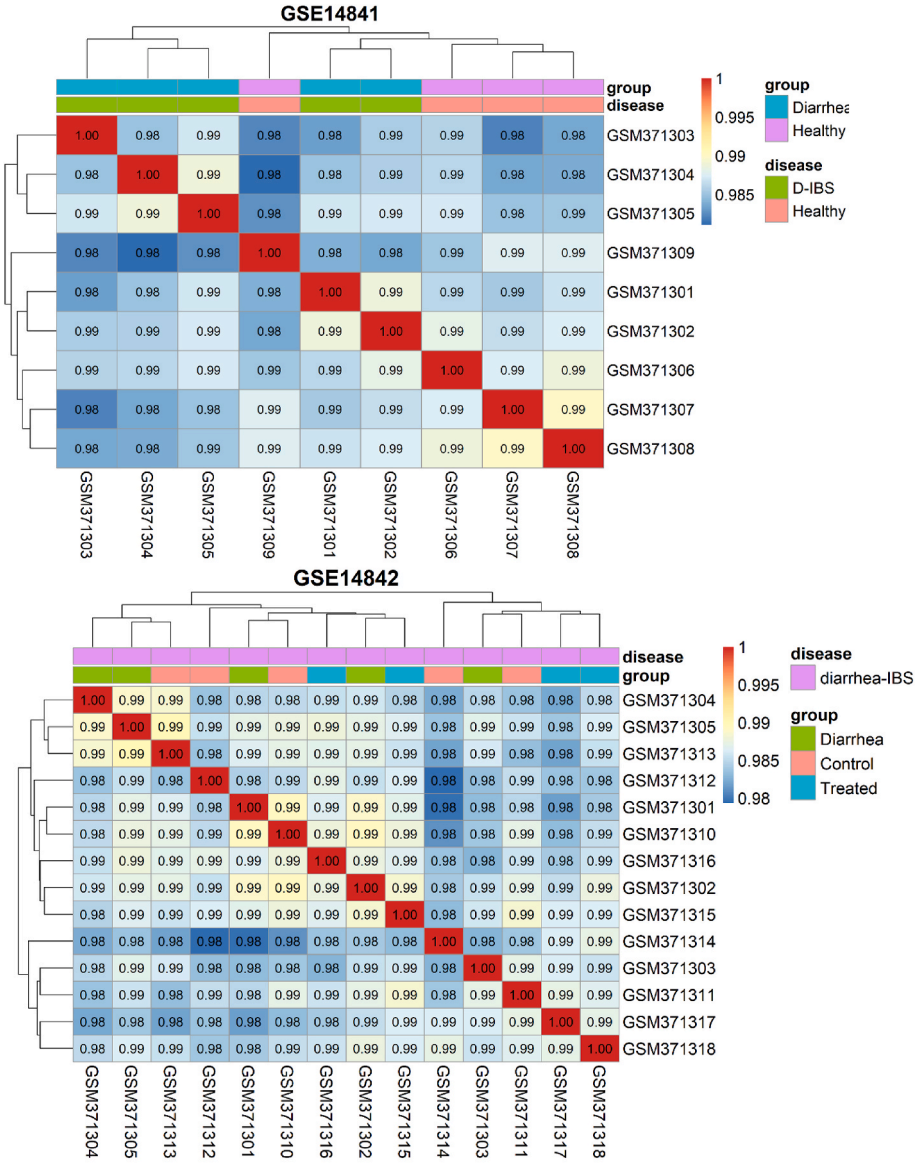

Fig. 5. Standardization and preprocessing of datasets (GSE14841 and GSE14842) for WGCNA and DEGs analysis. **A.** Pearson correlation between datasets. **B.** Principal component analysis (PCA) plot of datasets. **C.** Dimensional reduction MDS plots for dissimilarities in datasets.

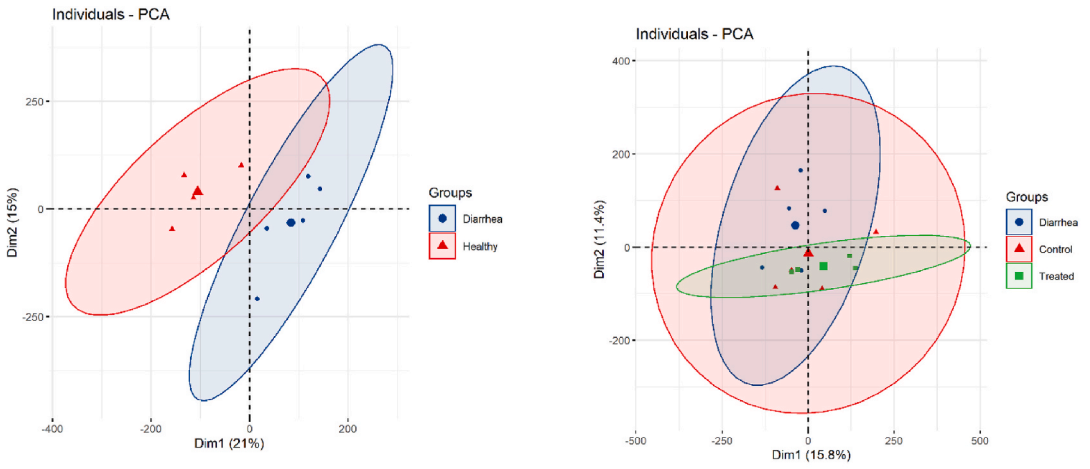

B. PCA Plots for identifications of outliners

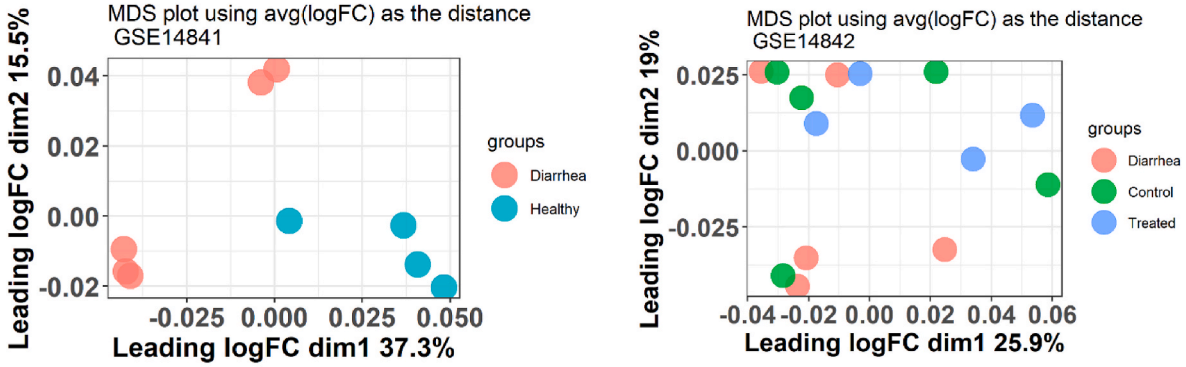

C. MDS plots of data dimensionality reduction

Fig. 5. (*continued*).

significance of significantly overlapping gene expressions between the WGCNA and DEGs genes of both datasets. Gene expression levels were considered as low and high categories based on the intensity of their expression. GSEA analysis of KEGG and GO biological processes was conducted with Cluster profiler software with an FDR ≤0.05 threshold.

2.6.6. Screening of disease and bioactive compounds associated with target genes

The potential genes associated with the bioactive substances of Cm. EtOH were acquired from the Drugbank (http://drugbank.com, accessed date: August 28, 2021) and the Swiss–target prediction tool (http://www/swisstargetprediction.ch, accessed date: August 28, 2021). The key terms "irritable bowel syndrome (IBS)," "constipation," and "diarrhea" were used to obtain the disease-associated genes on the Gene–card (https://www.genecards.org, accessed date: August 28, 2021), DisGeNET (http://www.disgenet.org/web/DisGeNET, accessed date: August 28, 2021), Pubmed (https://pubmed.ncbi.nlm.nih.gov, accessed date: August 28, 2021), and Online Mendelian Inheritance in Man (OMIM) (https://www.omim.org, accessed date: August 28, 2021).

2.6.7. Detection of key genes

We outlined the key genes based on the intersection of genes of bioactive substances, disease, WGCNA, and DEGs of both datasets using the VennDiagram (v1.7.3) R package. The relationship between bioactive chemicals, illness, WGCNA, and DEGs was represented through a Venn diagram.

2.6.8. Construction of PPI, bioactive compounds, and functional enrichment networks

Cytoscape 3.8.0 was used to construct and evaluate the bioactive compounds and disease–associated target genes (C–T–D), protein-protein interaction (PPI), bioactive compounds, disease-associated target proteins, and pathways (C–T–P) networks. PPI was constructed string plugin of Cytoscape.

2.7. Protein homology modeling and molecular docking

2.7.1. Protein homology modeling

We used the Uniprot database to obtain high-quality protein sequences (https://www.uniprot.org/, accessed date: August 27, 2021). Uniprot protein sequences were blasted against one or more PDB templates to identify the three-dimensional homology model (Maestro v11.8, Schrodinger suite 2018–4). In brief, we initially evaluated the Uniprot sequence in the Extasy ProtParam tool (http://www.web.expasy.org/protparam, accessed date: August 30, 2021) for physical and chemical characteristics [14,22]. Homology modeling involves the following steps: 1) import of Uniprot sequence, 2) BLAST the sequence in the PDB Database, 3) sequence alignment, and 4) model building. After modeling the protein, the model was tested and submitted for the protein reliability report. The Prime Refine-Loops and Prime Minimize modules were applied to refine the constructed model if protein reliability did not meet expectations. A Ramachandran plot using PROCHECK and SAVES v6 (https://saves.mbi.ucla.edu/, accessed date: August 30, 2021) was used to validate the minimized protein model [23,24].

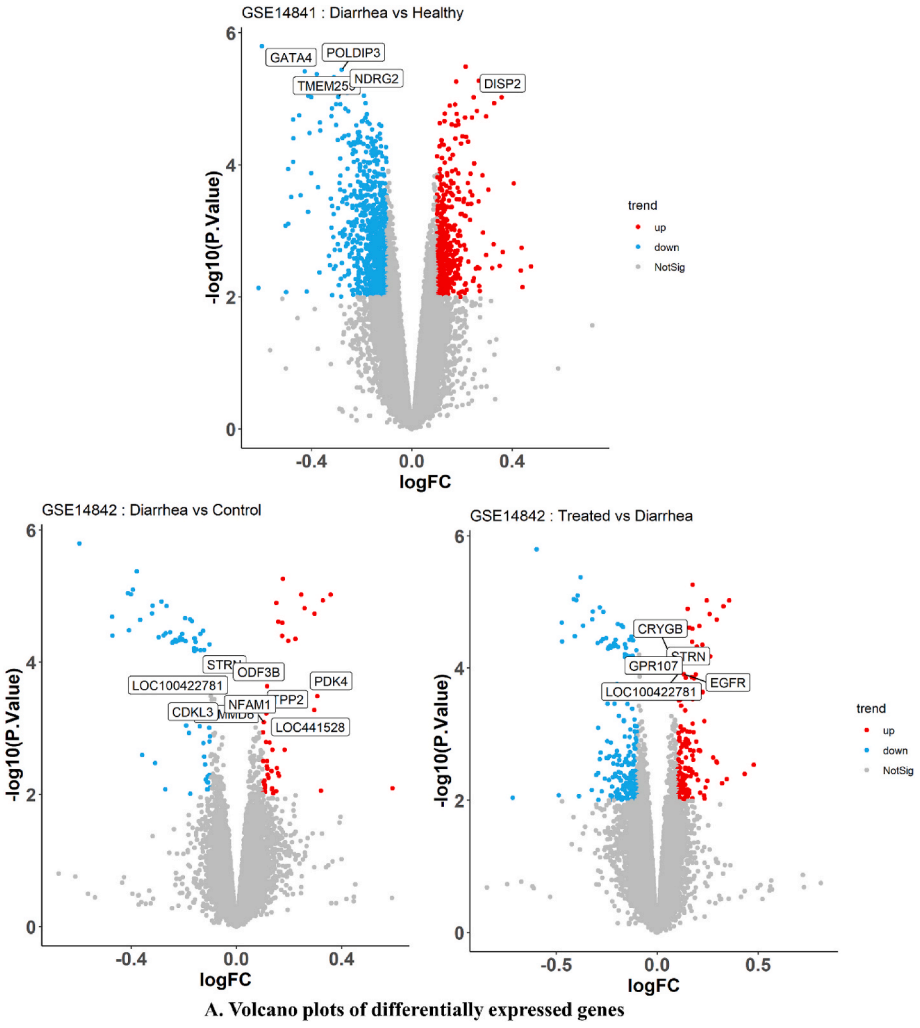

Fig. 6. Contrast-dependent identification of differentially expressed genes (DEGs) of GSE14841 and GSE14842. **A.** DEGs Volcano plots of datasets. **B.** Top 15 DEGs of datasets. Contrasts: GSE14841: *Diarrhea vs. Healthy*, GSE14842: *Diarrhea vs. Control*, *Treated vs. Diarrhea.*

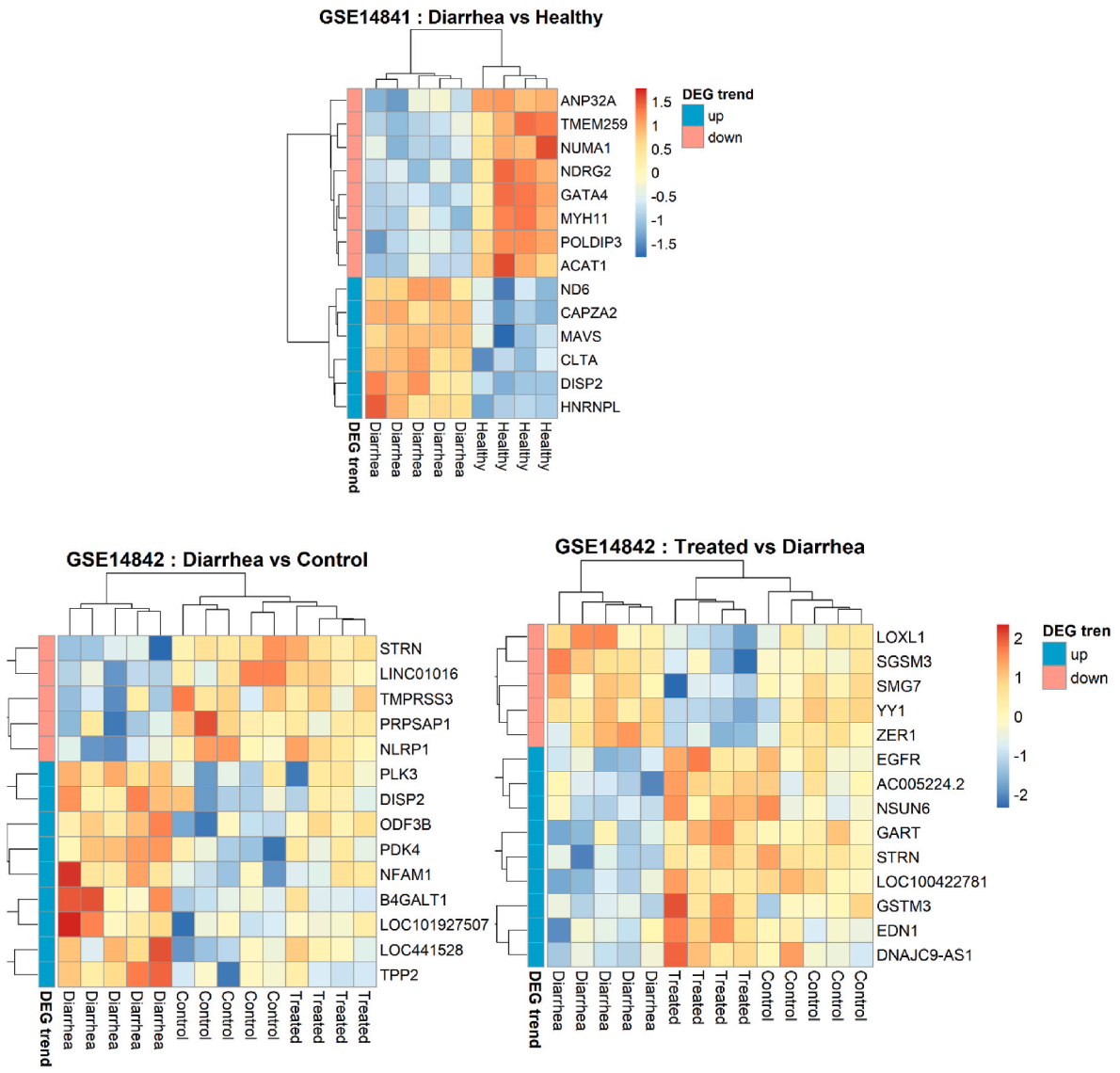

Fig. 6. (*continued*).

2.7.2. Molecular docking

The various modules of Maestro and BIOVIA Discovery Studio 2021 were used to carry out molecular docking according to the previously mentioned parameters and thresholds [14]. 2D ligands from NCBI PubChem (https://pubchem.ncbi.nlm.nih.gov, accessed date: August 28 28, 2021) were optimized, minimized, and ionized using the LigPrep module. The protein preparation module was then employed for assigning hydrogen bonds, minimization of het–states, reducing zero-order, disulfide bonds formation, ionization, and optimization of 3D structures of the protein model. Furthermore, structural gaps were filled with the help of the prime tool, and het groups were protonated at a pH of 7.0 ± 2.0 using the Epik tool. At a pH of 7.0, PROPKA was employed for the optimal arrangement of hydrogen bonds in protein models, and OPLS3e was used for constraint energy minimization. To facilitate ligand interaction, the sitemap module was utilized to identify the coordinates for the protein binding pockets and the cubic grid box of the receptor grid generation module. The molecular docking was performed with Glide's extra precision using prepared ligands, proteins, and receptor grid files. The Epik tool was utilized to apply penalties to the docking score. The Prime MM–GBSA module calculated the binding energies of Glide ligand-protein complexes. As reported in earlier studies, the predicated inhibition constant (Ki) was calculated [23,24].

2.8. Molecular dynamics simulations

The stability of the docked binding complex was determined by molecular dynamics simulations (MDS) using GROMACS 2022.3 (http://www.gromacs.org). Swiss-param (https://www.swissparam.ch/) server was used to generate the topology of the ligand, and a GROMACS and CHARMM36 force field was used to generate the topology of the protein. The TIP3P water solution was then applied for the solvation of protein-ligand complexes. After placing it in the box, we neutralized the ligand-protein complex by adding 0.15 mM Na and Cl ions to a 1 nm cubic box. This system minimized its energy consumption by using the steep-descent approach with 50,000 steps. Using NVT and NPT, we performed an ensemble equilibration for 200 ps. The temperature was set to 310 K with a modified Berendsen thermostat, and the pressure was set to 1 atm with the Berendsen technique. The particle-mesh-Ewald approach and van der Waals approach were applied to determine electrostatic interactions and van der Waals interactions at a 1 nm threshold.

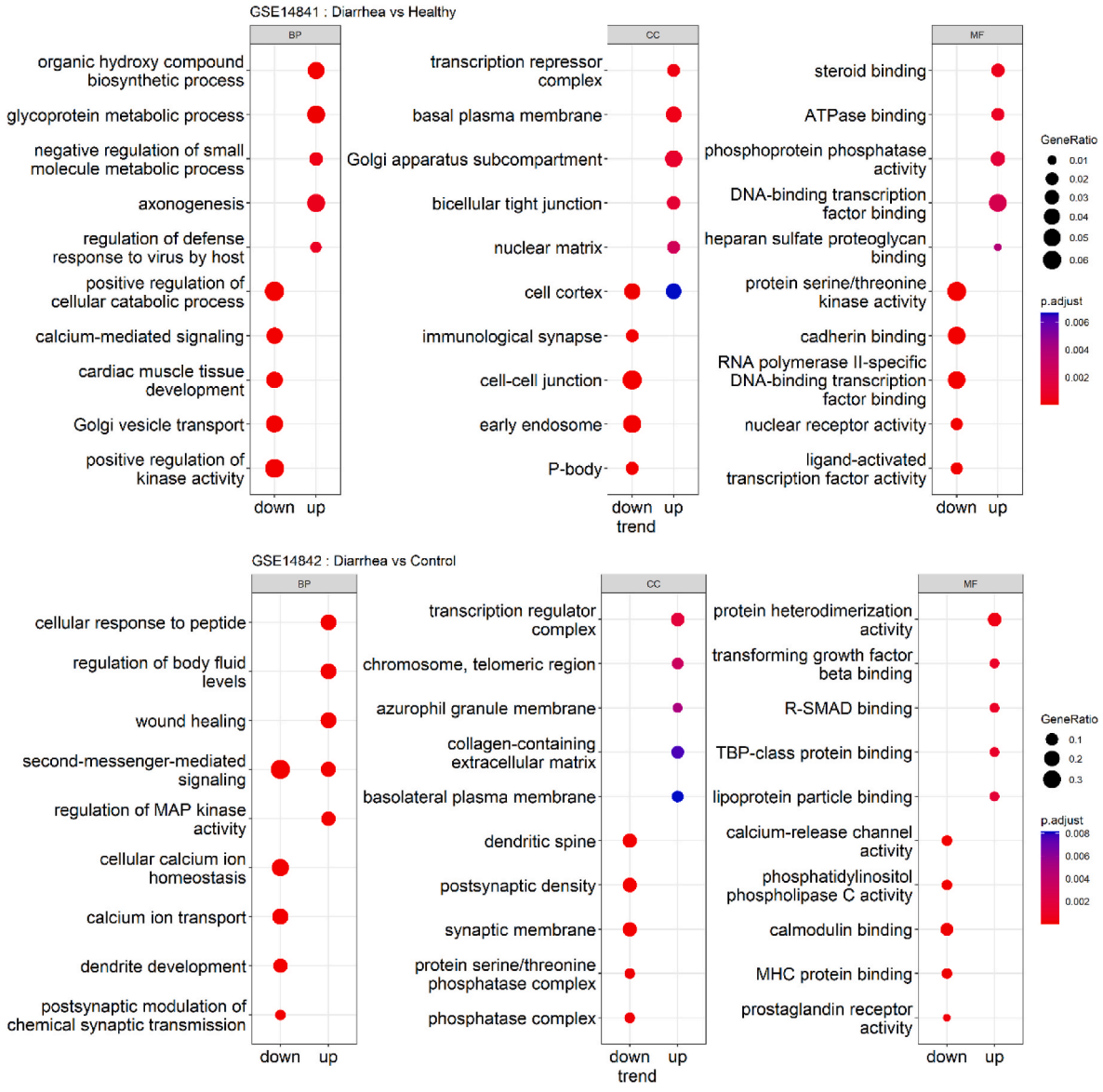

Fig. 7. Functional enrichments of up-regulated and down-regulated DEGs of datasets. **A.** Gene Ontology. **B.** KEGG pathways enrichment. GO: Gene Ontology; BP: Biological process; CC: cellular compartment; MF: molecular functions.

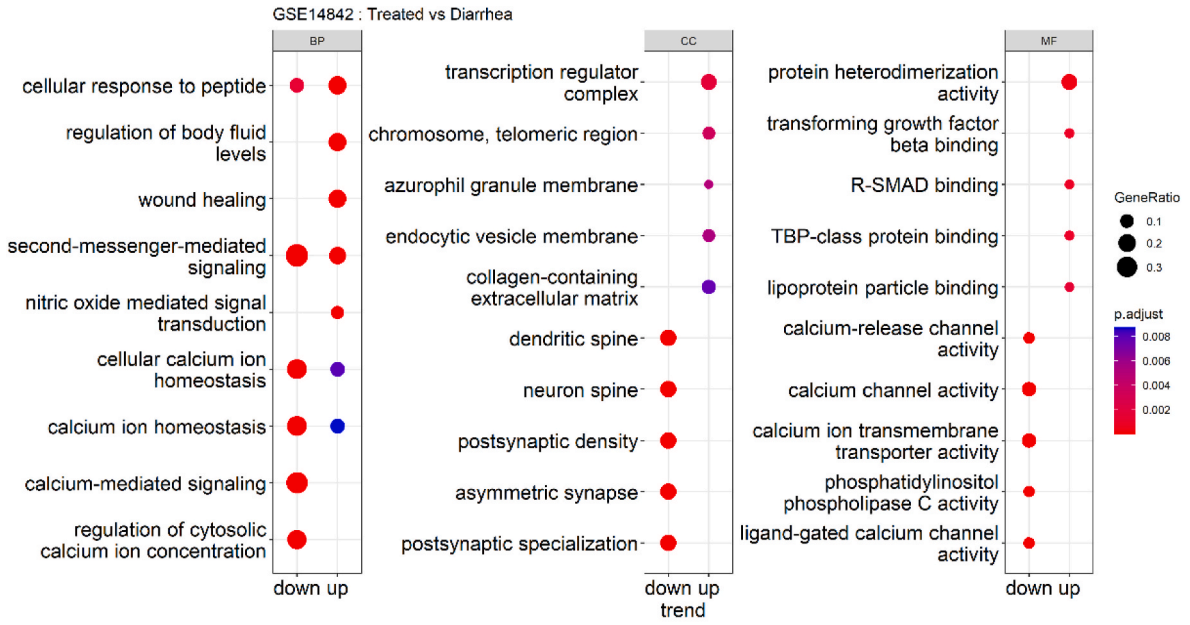

A. Gene Ontology (GO) enrichment of differentially expressed genes.

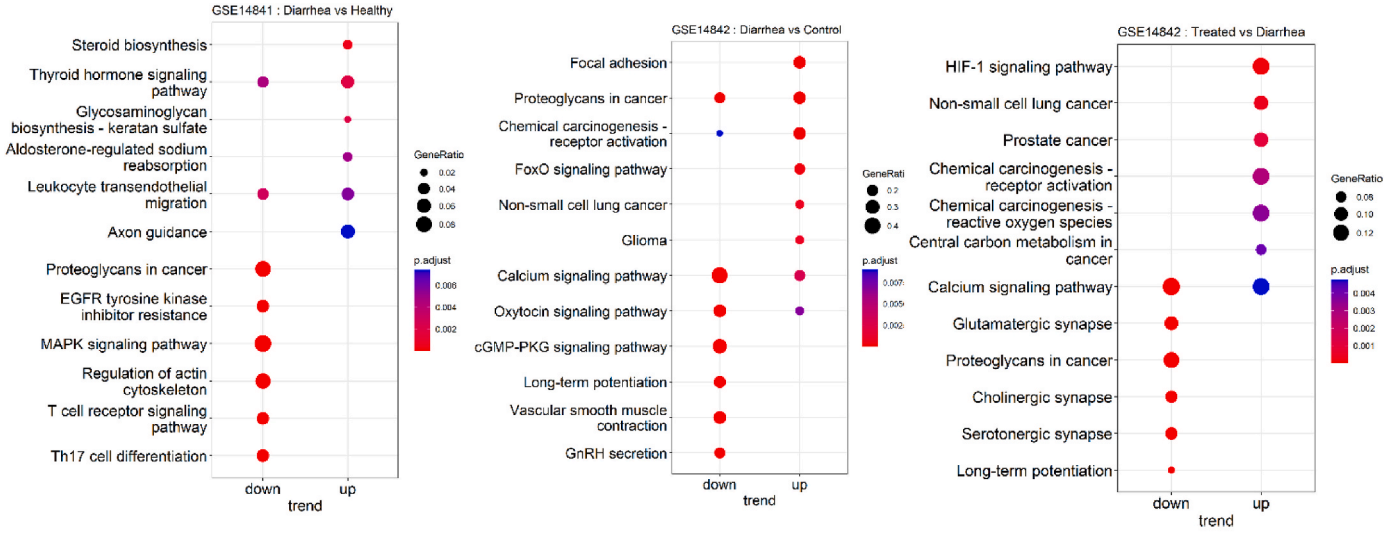

B. KEGG pathways enrichment.

Fig. 7. (*continued*).

Finally, the trajectory was saved every 10 ps after a simulation of the system for 10 ns with a time step of 2 fs. We measured root mean square deviation (RMSD), root mean square fluctuation (RMSF), the radius of gyration (Rg), solvent-accessible surface area (SASA), and hydrogen bond interactions using simulated trajectory acquisitions.

2.8.1. *Binding energies*

Calculating free binding energies between proteins and their ligands is necessary to study reciprocal recognition and binding. The free energy of protein receptors reflects the strength of their interaction with ligands, so the positive and negative values of the free energy represent the possibility of interactions. The MM-PBSA approach was used to determine the binding free energy of a ligand-protein complex. In order to calculate the free binding energy, the gmx_MMPBSA module of GROMACS was used [25]. The last 20 frames of trajectory was used for analysis.

2.8.2. *Principal component analysis and free energy landscape*

In high-dimensional data, principal component analysis (PCA) is frequently used for finding patterns. This method can explain these changes by demonstrating concerted atomic displacements in MD trajectories and significant conformational changes between structures. This coordinated movement of atoms and conformational changes determines the structure and function of proteins. The data covariance matrix C is diagonalized to determine the primary components of the MD simulation trajectory. A principal component analysis was conducted using the GROMACS tools gmx_covar and gmx_anaeig.

GROMACS tool gmx sham was used to compute free energy landscapes (FEL). The following equation was used to calculate FEL:

$$\Delta G\ (PC1, PC2) = -KBTlnP\ (PC1, PC2)$$

PC1 and PC2 represent the reaction coordinates, KB represents the Boltzmann constant, and P (PC1, PC2) represents the probability distribution. OriginPro software was used to plot FEL.

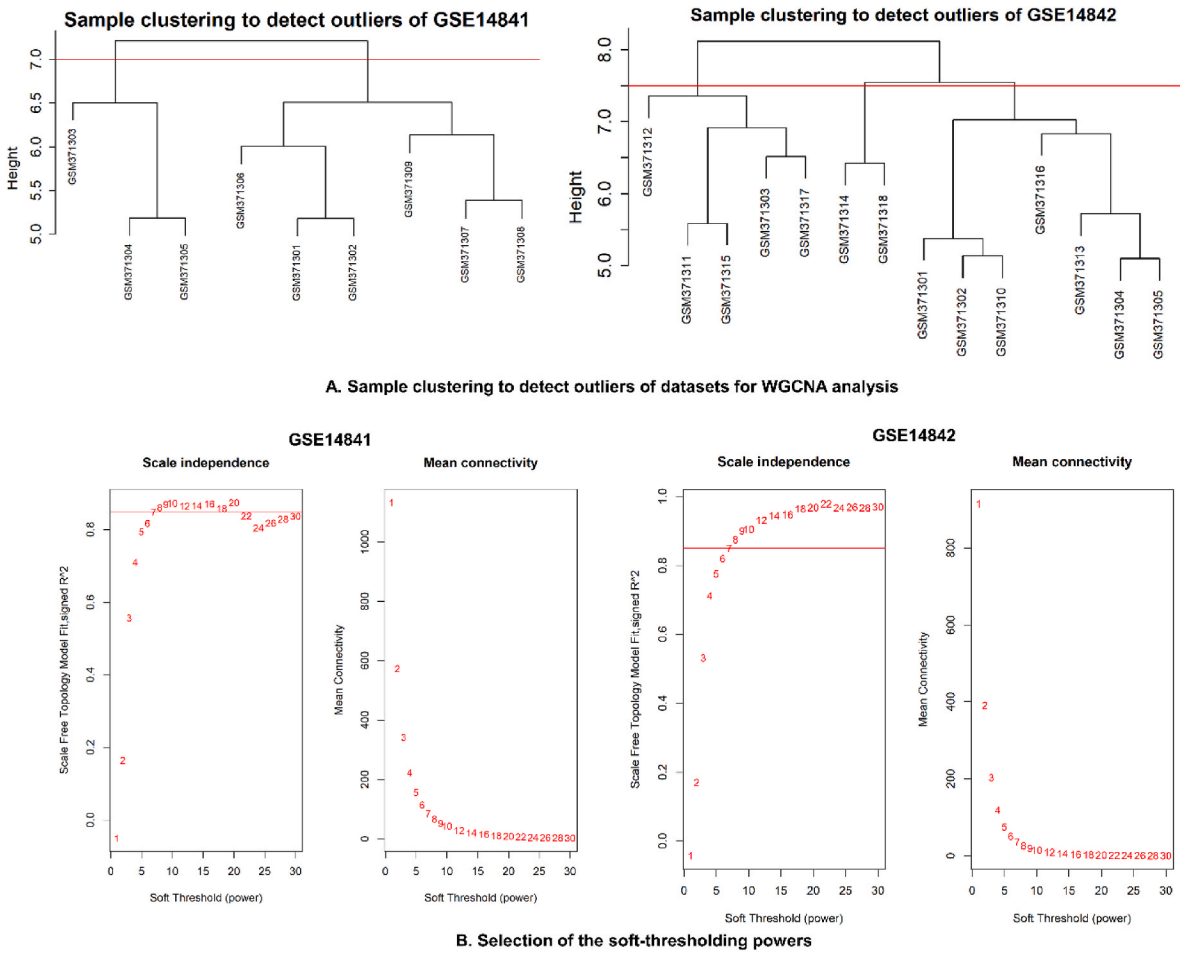

Fig. 8. A. The clustering of samples to identify outliners **B.** Scale-free fit index (left) and mean connectivity analysis (right) were used in the soft-threshold power selection process.

2.9. Softwares

Physiological responses of tissues were recorded using LabChart Pro 7. Molecular docking was carried out using Maestro v11.8 (Schrodinger suite 2018-4) and BIOVIA Discovery Studio 2021. The statistical analysis was done by GraphPad Prism 8, OriginPro 2022 and RStudio (version 2021.02.3), and the network was constructed using Cytoscape 3.8.0.

3. Results

3.1. Identification of bioactive compounds

Twenty phytoconstituents were identified in the LC ESI-MS/MS study of Cm.EtOH. Table 1 lists the fragmentations of the major phytochemicals responsible for the biological activities.

3.2. Method validation and parameters optimization for HPLC

We adjusted HPLC settings to achieve maximum separation of phytoconstituents and noticeable peaks in Cm.EtOH. Phytoconstituents were separated using a binary mobile phase system with an 0.8 mL/min flow rate. Different wavelengths of 320, 280, and 250 nm were used to identify separation peaks for Cm.EtOH. In the next step, the peaks were compared to external standards (Table 2 and Fig. S2). Table 2 lists the separation peaks for phytochemicals from Cm.EtOH at wavelengths of 200, 280, and 320 nm.

3.3. Quantification of phytochemical compounds

Using linear regression, phytoconstituents were quantified by comparing them to external standards. Table 2 listed the quantification of phytoconstituent in Cm.EtOH.

3.4. Isolated tissue experimentation

3.4.1. Effects on isolated rabbit jejunum preparation

To investigate the smooth muscle relaxant efficacy of the *C. melo*, Cm.EtOH was added to the spontaneous contraction of jejunal preparations. Cm.EtOH at the dose of 3.0 mg/mL and 1.0 mg/mL completely inhibited potassium chloride (80 and 25 mM)–induced spasm, respectively. These effects were dose-dependent spasmolytic effects. Cm.EtOH inhibited the spontaneous rhythmic spasm dose–dependently with an EC_{50} of 0.3350 mg/mL (0.2121–0.5374; CI 95%). Potassium chloride (80 mM) had an EC_{50} of 0.4519 mg/mL (0.3402–0.6041; CI 95%), and potassium chloride (25 mM) had an EC_{50} of 0.1986 mg/mL (0.09849–0.4092; CI 95%) (Fig. 1). The DRCs of calcium were produced in cytosolic calcium–free jejunal preparation to establish the calcium ions channel antagonistic response of Cm.EtOH in both the presence and absence of Cm.EtOH. Cm.EtOH produced a rightward shift by suppressing calcium DRCs at 1 and 3 mg/mL doses, significantly suppressing calcium contractile response DRCs at 3 mg/mL. Verapamil, a calcium channel blocker, was used to confirm these findings of Cm. EtOH. Verapamil reduced spontaneous concentrations of jejunal preparations, potassium chloride (80 and 25 mM)–elicited spasm at corresponding doses of 0.1, 1, and 0.1 μM with EC_{50} of 0.05876 μM

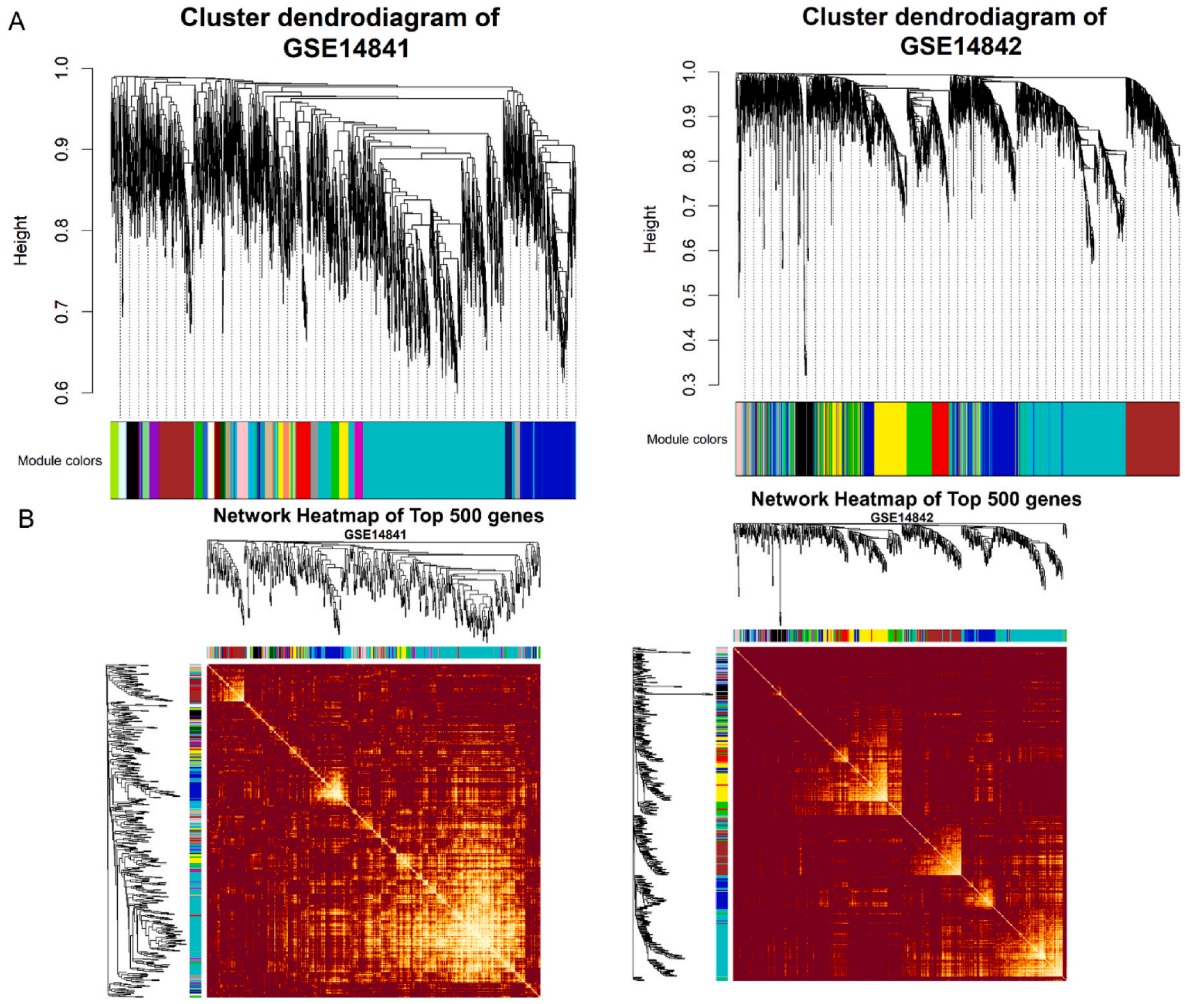

Fig. 9. Module identification of weight gene co-expressed networks in datasets. **A.** Cluster dendrogram and module assignment; The branches represent highly interconnected groups of genes. The horizontal bar shows the colors of the modules. **B.** Heatmap of top 500 genes of weight gene co-expressed network.

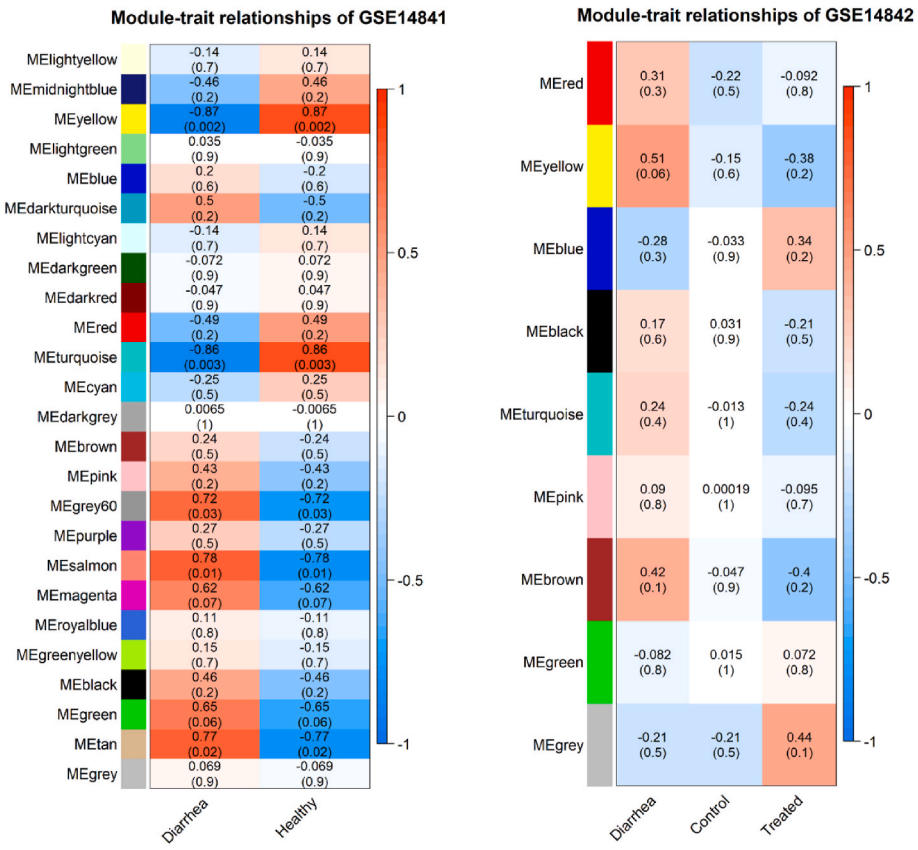

Fig. 10. Pearson's correlation heatmap between datasets groups and color modules.

(0.04740–0.07326; CI 95%), 0.09154 μM (0.06903–0.1233; CI 95%), and 0.01623 μM (0.01289–0.02051; CI 95%). Additionally, calcium DRCs were constructed, resulting in calcium DRCs blocked at a dose of 0.3 μM equivalent to Cm.EtOH, indicating antagonistic extract action towards the calcium channels (Fig. 1).

3.4.2. *Effect on isolated rabbit tracheal preparations*

Cm.EtOH was administered to tracheal preparations of rabbits in order to study the bronchodilator activity. Cm.EtOH exhibited dose–dependent dilatory effect when exposed to potassium chloride (80 mM) and carbachol (1 μM) sustained contraction at dosages of 1 mg/mL, with EC_{50} of 0.4632 mg/mL (0.2565–0.9517; CI 95%) and 0.1420 mg/mL (0.1014–0.1992; CI 95%), respectively. However, Cm.EtOH relaxed potassium chloride (25 mM) at a concentration of 0.3 mg/mL with an EC_{50} of 0.3657 mg/mL (0.1910–1.088; CI 95%) (Fig. 2). The carbachol DRCs were formed in both the presence and absence of Cm.EtOH (0.3 and 1.0 mg/mL) on tracheal preparation and their suppression resulted in a non-competitive shift to the right. In tracheal preparations, verapamil inhibited spastic spasm of potassium chloride (80 and 25 mM) and carbachol (1 μM) in a dose–dependent manner at respective doses of 1.0, 0.3, and 0.1 μM with EC_{50} of 0.1199 μM (0.08991–0.1601; CI 95%), 0.05451 μM (0.03380–0.08990; CI 95%) and 0.02205 μM (0.01496–0.03297; CI 95%). Verapamil inhibited DRCs for carbachol at a dose of 1 μM, similar to Cm.EtOH (Fig. 2).

3.4.3. *Effect on isolated rabbit urinary bladder preparations*

When Cm.EtOH was tested on potassium chloride (80 mM and 25 mM) and carbachol (1 μM)to induce spastic spasm in urinary bladder preparations. It exhibited a dose–dependent relaxant response. Potassium chloride (80 mM) contraction was relaxed at a dose of 3.0 mg/mL, with an EC_{50} of 0.4497 mg/mL (0.3682–0.5520; CI 95%). Carbachol (1 μM) and potassium chloride (25 mM)–induced spasms were relaxed at dose 1.0 mg/mL with EC_{50} 0.4048 mg/mL (0.2724–0.6291; CI 95%) and 0.09897 mg/mL (0.06971–0.1401; CI 95%) respectively (Fig. 3). The DRCs of calcium were produced in both the presence and absence of Cm.EtOH (1 and 3 mg/mL) and their suppression resulted in a noncompetitive right shift. Verapamil reduced potassium chloride (80 and 25 mM) and carbachol (1 μM)–induced spasm at corresponding doses of 1, 0.3, and 0.1 μM with EC_{50} 0.1425 μM (0.1162–0.1750; CI 95%), 0.03686 μM (0.02783–0.04901; CI 95%) and 0.01692 μM (0.01161–0.02446; CI 95%), respectively. Verapamil inhibited the calcium DRCs at a concentration (1 μM) similar to Cm.EtOH (Fig. 3).

3.5. *In vivo experiments*

3.5.1. *Maximum tolerated dose*

It was determined after 28 days of observation that Cm.EtOH was safe after the maximum tolerable extract dose was administered to rats. There was no change in body weight, clinical symptoms of discomfort, behavioral alterations, or mortality among rats after this period.

3.5.2. *Effect on GI charcoal meal intestinal Transit*

Cm.EtOH reduced the propulsive movements with the peristalsis index of Cm.EtOH was 62.86 ± 4.30% and 24.08 ± 5.5% at respective doses 150 and 300 mg/kg in comparison to loperamide (14.28 ± 2.8%) and verapamil (15.1 ± 3.7%) at dose 10 mg/kg (Fig. 4).

3.5.3. *Effect on castor Oil–Induced diarrhea*

Cm.EtOH protects the animals from defecation was 47.99 ± 3.9% and 78.91 ± 4.1% at respective doses of 150 and 300 mg/kg in comparison to loperamide (95.38 ± 3.5%) and verapamil (92.81 ± 3.8%) at dose 10 mg/kg (Fig. 4).

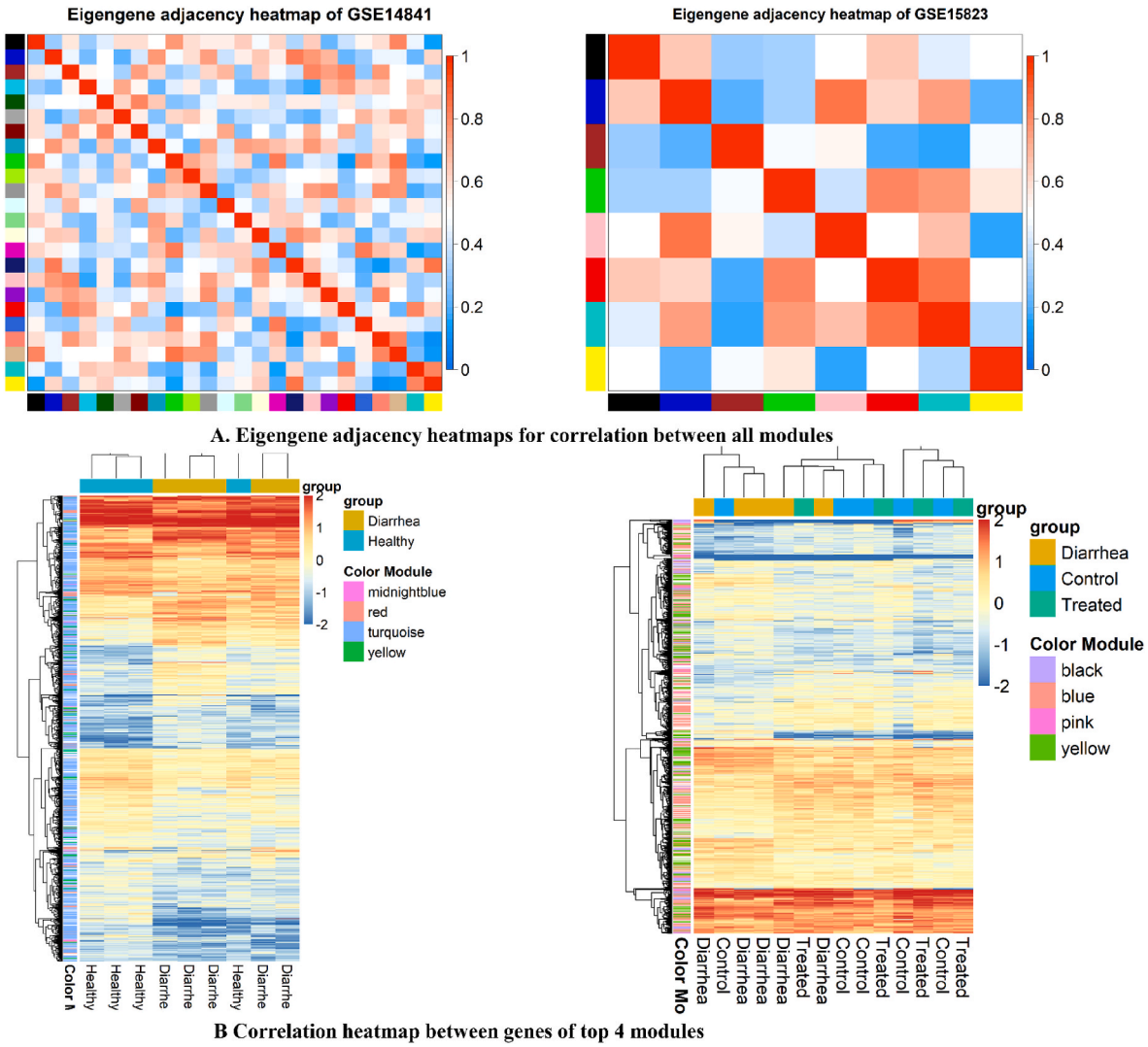

Fig. 11. Correlation association between WGCNA modules. **A.** Eigengene adjacency heatmaps for correlation between WGCNA modules. **B.** Correlation heatmap between of top four modules.

3.5.4. *Effect on intestinal fluid accumulation*

Cm.EtOH demonstrated a dose–dependent reduction in the intestinal fluid with weight 112.71 ± 2.3 g and 94.46 ± 3.7 g at respective doses 150 and 300 mg/kg in comparison to loperamide (89.87 ± 2.9 g) and verapamil (90.65 ± 1.7 g) (Fig. 4).

3.6. *WGCNA and DEGs studies*

3.6.1. *Data preprocessing and standardization*

GSE14841 and GSE14842, two genes associated with IBS–predominant diarrhea IBS (IBS–D) phenotype, were obtained from the GEO database. GSE14841 included nine samples with two groups, IBS-D and healthy, expressing 54,613 genes. 54,613 gene expressions were obtained from GSE14842 with three groups: IBS-D treated and control. Following unsupervised analysis, the pairwise correlation was used for scaling the data. For further analysis, 28,467 and 29,102 gene expressions were retrieved for GSE14841 and GSE14842, respectively, after removing genes with low expression using the coefficient of variance (Fig. 5).

3.6.2. *DEGs identification and enrichment analyses*

DEGs analysis was performed using Limma R for datasets GSE14841 and GSE14842, resulting in the identification of 1108 and 838 important genes, respectively. Among the genes included in GSE41841, 463 exhibited upregulation, and 647 displayed downregulation (Fig. 6A). The gene expression levels of 524 genes were downregulated, while 314 genes were up-regulated in GSE41842. We conducted the hierarchical clustering of GSE14841 and GSE14842, identifying the genes with the most remarkable differences between GSE14841 and GSE14842 (Fig. 6B). Cluster-profiler R package was also used to compare down-regulated and up-regulated genes in both datasets to determine GO and KEGG enrichment. Fig. 7 shows the most significant GO BP and KEGG terms for GSE14841 and GSE14842.

The most significant GO BP terms of GSE14841and GSE14842 are the regulation of oxidative stress-induced neuron death, inositol phosphate–mediated signaling, calcium–mediated signaling, stress-activated MAPK cascade, and modulation of cardiac muscle cell action potential. Several genes of GSE14841 and GSE14842 were also significantly associated with KEGG pathways: thyroid hormone signaling, aldosterone–regulated sodium reabsorption, MAPK signaling, calcium signaling, cGMP–PKG signaling, PI3K–Akt signaling, and vascular smooth muscle contraction.

3.6.3. *Identification of WGCNA modules*

An expression matrix was constructed based on GSE14841 and GSE14842 preprocessed data. A total of 3195 genes were included in the

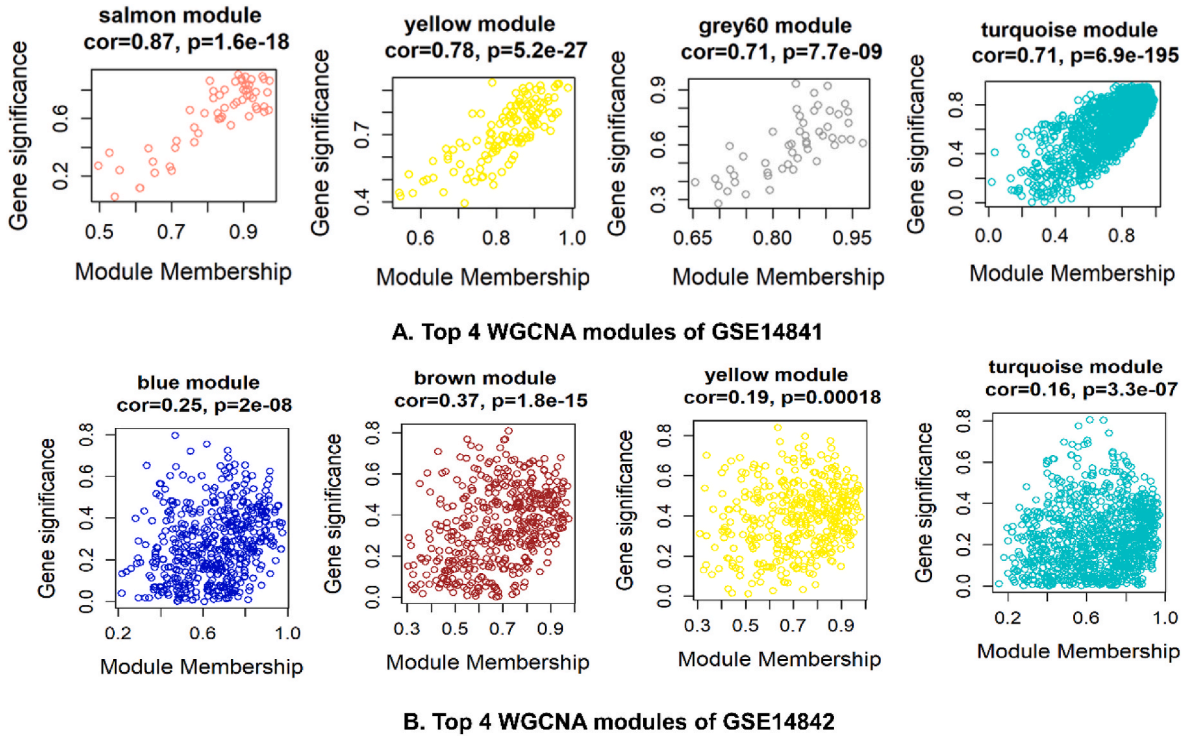

Fig. 12. Identification of WGCNA modules of GSE14841.

top 25% of variants for GSE14841 and 3203 genes for GSE14842 for WGCNA analysis. The cut height for GSE14841 and GSE14842 was set at 7.0 and 7.5, respectively, to omit the most apparent outliers (Fig. 8A). A gene expression matrix was created when GSE14841 and GSE14842 samples were standardized, background-corrected, and polymerized. We choose a soft threshold of $\beta = 8$ to verify the attributes of the scale-free network when the fitting coefficient R^2 approaches 0.90; to build a gene coexpression network. (Fig. 8B).

A clustering dendrogram can be drawn by merging modules with high similarity using dynamic tree cutting and the hclust function. A clustering dendrogram (Fig. 9A) was drawn by combining highly similar modules with dynamic tree cutting and hclust. A total of 25 gene modules were found for GSE14841, and 9 gene modules were found for GSE14842.

3.6.4. Correlation between modules and diarrhea

The correlation result of GSE41841 and GSE14842 are illustrated in Fig. 10, which shows the association between clinical features and module characteristics. According to the heatmap, the positively correlated modules of GSE41841 with control were positively significant correlated modules with diarrhea were salmon (cor = 0.78, p-value = 0.01), tan (cor = 0.77, p-value = 0.02), grey60 (cor = 0.72, p-value = 0.03), green (cor = 0.6 5, p-value = 0.06), and magenta (cor = 0.62, p-value = 0.07).

In GSE41842, positively significant correlated modules with diarrhea were yellow (cor = 0.51, p-value = 0.06), brown (cor = 0.42, p-value = 0.13), red (cor = 0.31, p-value = 0.29), and turquoise (cor = 0.24, p-value = 0.41). In contrast, positively significant modules with the treated group were grey (cor = 0.44, p-value = 0.11), blue (cor = 0.34, p-value = 0.24), and green (cor = 0.07, p-value = 0.81).

3.6.5. Hub–gene detection and functional pathway enrichment

Fig. 11 illustrates the correlation between modules in the heatmap of eigengene adjacency. In GSE14841, the modules with positive correlation were yellow, turquoise, salmon, and grey60; in GSE14842, the modules were yellow, turquoise, blue, and brown (Fig. 11A). Fig. 11B illustrates the relationship between these four modules and gene expression. Mostly genes have a positive correlation association.

All modules were utilized to identify hub genes highly linked to diarrhea pathogenesis to analyze the relationship between gene significance (GS) and module membership (MM). We calculated correlations between MM and GS and analyzed the data (Fig. S3, Fig. 12). It was determined that the most correlated modules for GSE41841 were salmon, yellow, turquoise, and grey60 with 57, 126, 1267, and 114 hub genes, respectively. GSE41842 had four correlated modules: brown, blue, yellow, and turquoise. These modules contained 432, 491, 383, and 1007 hub genes.

Functional pathway enrichment was conducted using Cluster Profiler R package on both datasets of hub genes. The results of the functional enrichment of both datasets are depicted in Fig. 13. GSE14841 and GSE14842 were enriched in GO biological terms; the ERK1, ERK2 positive regulation cascade, cardiac muscle relaxations, membrane depolarization during action potentials, glutamatergic synapses, calcium–mediated signaling and phosphatidylinositol binding. KEGG pathways for top WGCNA modules in GSE14841 and GSE14842 were AMPK and phospholipase D, the calcium and MAPK signaling, the JAK-STAT, the PI3K–Akt pathway, ErbB signaling, and dopaminergic synapses.

3.6.6. GSEA analysis of common genes

We performed GSEA analysis on the common genes of DEG lists and the top modules of both datasets to identify related gene expressions based on the DEG list. GSE14841 and GSE14842 genes were identified as related to GO BP, actin filament-based displacement, MAPK signaling, the ERK1, and ERK2 signaling, calcium ion homeostasis, and control of cardiac muscle contractions. The GSEA KEGG included were the ErbB signaling pathway, the PI3K–Akt signaling pathway, the calcium signaling pathway, and the cGMP–PKG signaling pathway (Fig. 14, Fig. 15).

3.6.7. Identification of smooth muscle contraction pathways

We used a cross-functional pathway screening to enhance findings

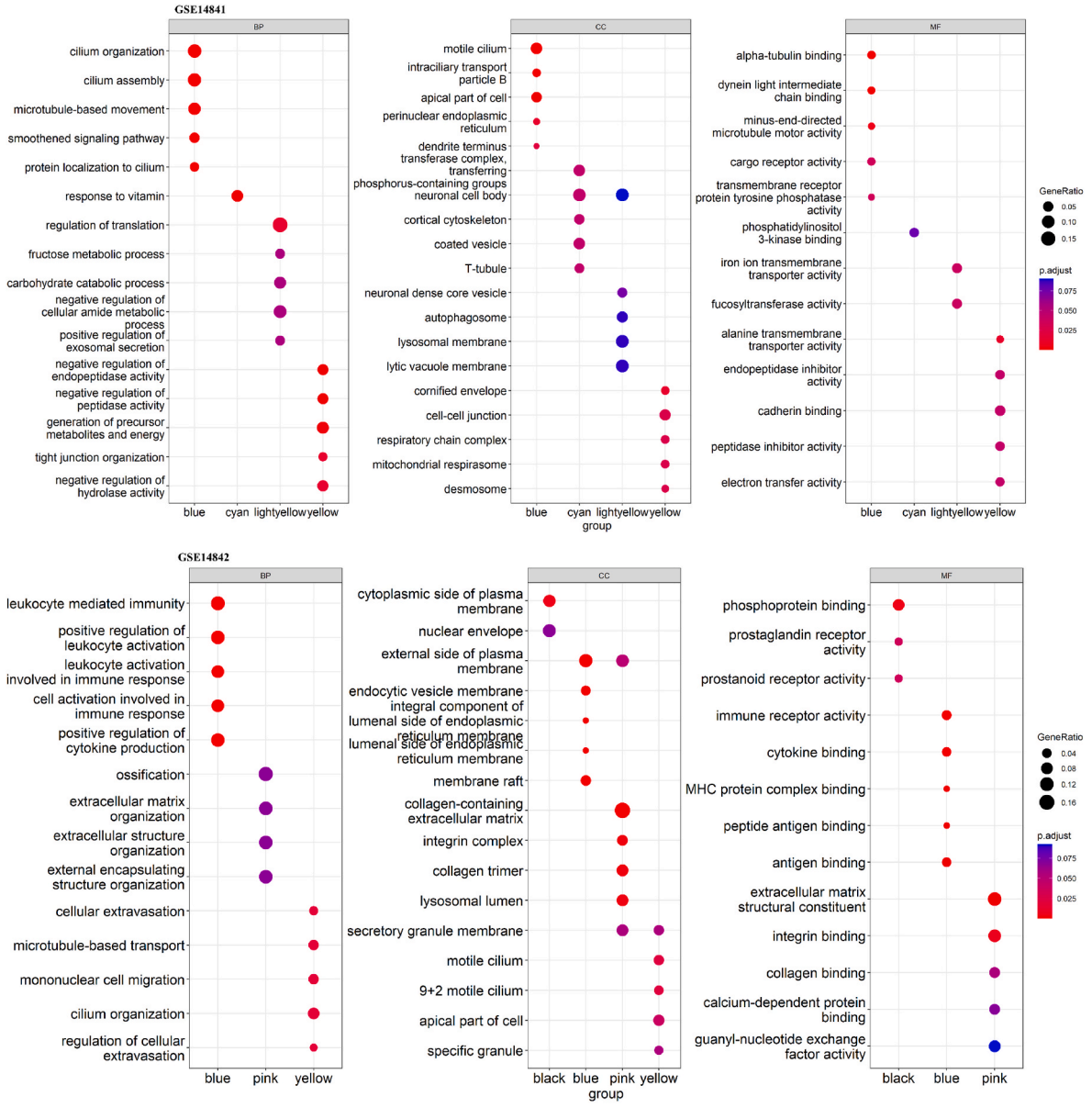

A. GO enrichment of top 4 modules

Fig. 13. The functional enrichment of top 4 WGCNA modules of GSE14841 and GSE14842. **A.** Gene Ontology (GO) enrichment in biological process (BP), cellular compartment (CC), and molecular functions (MF). **B.** KEGG pathways enrichment.

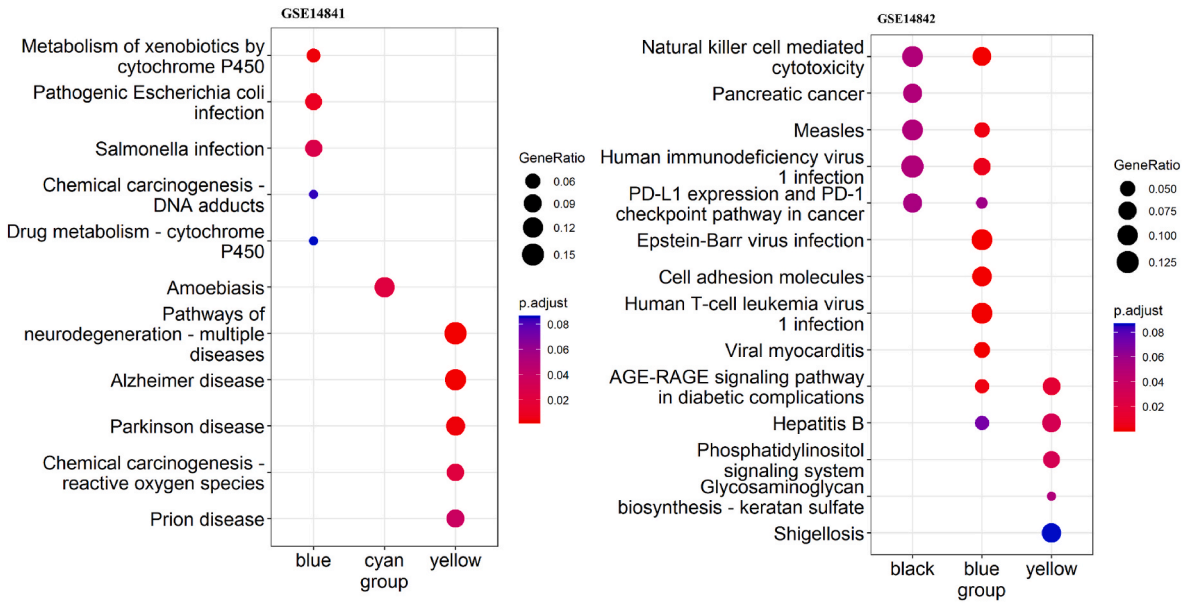

B. KEGG pathways enrichment of top 4 modules

Fig. 13. (*continued*).

from both datasets related to calcium-mediated signaling and smooth muscle contraction. Using the *hclust* function, genes and functional terms obtained from a particular sample were examined for expression and clustering in various DEGs and WGCNA modules. Fig. 16A shows the expressions of GO biological terms in the different groups of GSE14841 and GSE14842.

There are many genes in GSE41841 involved in calcium signaling and muscle contraction, including were *PLCG2, PLCG1, CX3CR1, PLCE1, CHRM3, PPP1R9B, PPP1R9A, AVPR1A, ACKR4, BHLHA15, CXCR6, PTGDR2, EDN2,* and *SGCD*. Several genes were involved in smooth muscle contraction and calcium-mediated signaling for GSE41842 *CXCR4, CHRM3, PLCE1, PLCG2, PLCG1, CCR2, CCR9, CCR10, CAMKK2, BHLHA15, AVPR1A, PPP1R9B, PPP1R9A, MCTP1, PTGDR2* and *SGCD* (Fig. 16B).

3.6.8. *Identification of potentially active genes for bioactive compounds and disease*

A threshold score of more than 50 or a probability greater than 0.5 was used to extract the most likely target profiles for every bioactive molecule from the TCMSP, Swiss-target prediction, and Drugbank databases. The total number of genes found for Cm.EtOH was 317 after removing duplicates. The gastrointestinal disease genes with key terms "diarrhea," "constipation," and "irritable bowel syndrome" were retrieved from Gene card, DisGeNET, Pubmed, and OMIM databases. The target genes were rectified using Uniprot and then validated with the VarElect tool. These targets were used to identification of key genes.

3.6.9. *Identification of key genes*

The DEG list, bioactive compounds target genes, disease–associated genes, and WGCNA genes were intersected for comparison, and common target genes were considered key genes for network construction (Fig. 17A). GSE14841 had 17 overlapped genes, including *AVPR2, EGFR, ACE, MAPK1, ACHE, PPARA, SRC, APP, ALOX5, ITPR1, BCL2L1, PLCG1, PIK3CG, PTGER4, DISP2, CHRM3,* and *GPR82*. GSE14842 had 20 overlapped genes: *EGFR, MMP9, INPP5E, CHRM3, CACNA1A, ERK1, PIK3R2, CAV1, ESR2, PARP1, MAPK1, CACNA1D, PLCG1, CDK2, RORA, PDK4, ADORA3, CAMK2B, TMPRSS3* and, *PIK3CG*. The common genes in GSE14841 and GSE1482 were *EGFR, MAPK1, PIK3CG,* and *CHRM,* and they were considered as most common key genes for both datasets. Genes from both data sets were pooled and considered for network pharmacology investigations.

3.6.10. *PPI and CTP network construction with key genes*

Protein–protein interactions (PPI) of all retained key genes were investigated using Cytoscape's STRING plugin. The key genes network contained 33 nodes and 89 edges. According to network analysis, *ACHE* (degree = 33) has the highest degree with correspondence to *PPARA* (degree = 26), *CACNA1D* (degree = 25), *CHRM3* (degree = 20), *SRC* (degree = 18), and *EGFR* (degree = 16).

Between bioactive chemicals and disease–associated target genes, a C–T–D network with 40 nodes and 112 edges was built in Cytoscape. According to network analysis, apigenin had the most favorable impact on target genes with a degree of 27; subsequent, quercetin (degree = 23), kaempferol (degree = 19), luteolin (degree = 17), and rutin (degree = 11) (Fig. 16B, Table S3). Based on its interactions with gene ontology biological processes (GO–BP) terms and KEGG signaling pathways, a compound target pathway (C–T–P) network was built (Fig. 16C, Table S4). It contained 86 nodes and 169 edges. In C–T–P, the degree score of GO biological process terms was intracellular receptor signaling pathway (degree = 12), calcium–mediated signaling (degree = 12), cell growth (degree = 11), sodium ion homeostasis (degree = 9), and muscle system process (degree = 6). Similarly, for KEGG pathways, the degree score were proteoglycans in cancer (degree = 23), cGMP–PKG signaling pathway (degree = 18), and calcium–mediated signaling pathway (degree = 12).

3.7. *Protein homology and validation*

We used the Uniprot sequence to build the protein models: Q13976 for cGMP-dependent protein kinase 1, P48736 for phosphoinositide 4,5-bisphosphate 3-kinase (PI3KC), P28482 for mitogen-activated protein kinase 1 (MAPK1, ERK2), and Q02641 for voltage-dependent calcium channel subunits.

3.7.1. *Physicochemical characteristics*

We used ProtParam to analyze cGMP-dependent protein kinase, PI3KCγ, MAPK1 or ERK2, and VGCAB1. Table 3 summarizes the results.

3.7.2. *Validation of homology modeling*

BLAST searches were conducted to identify homology modeling

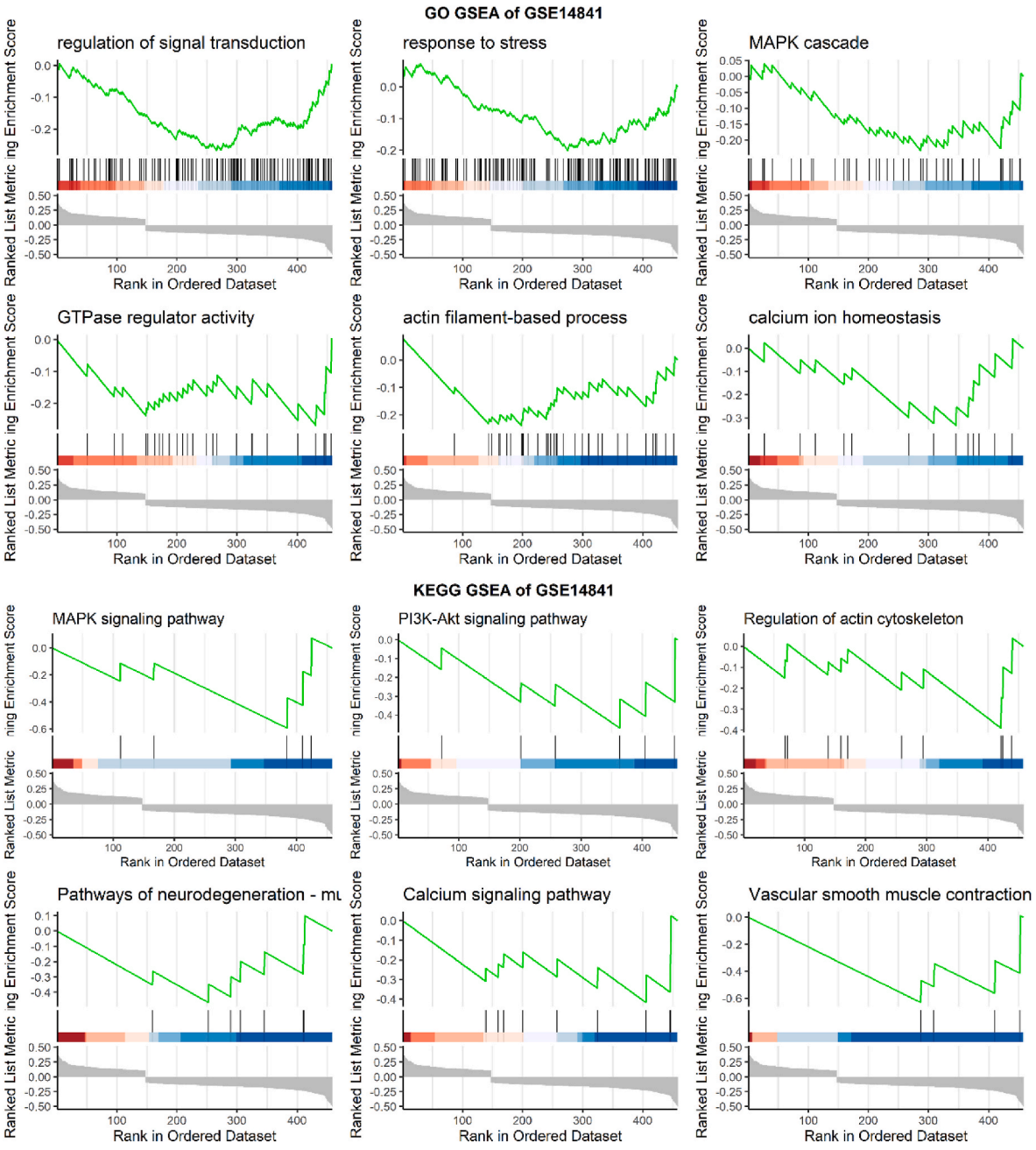

Fig. 14. GO and KEGG gene set enrichment analysis of GSE14841.

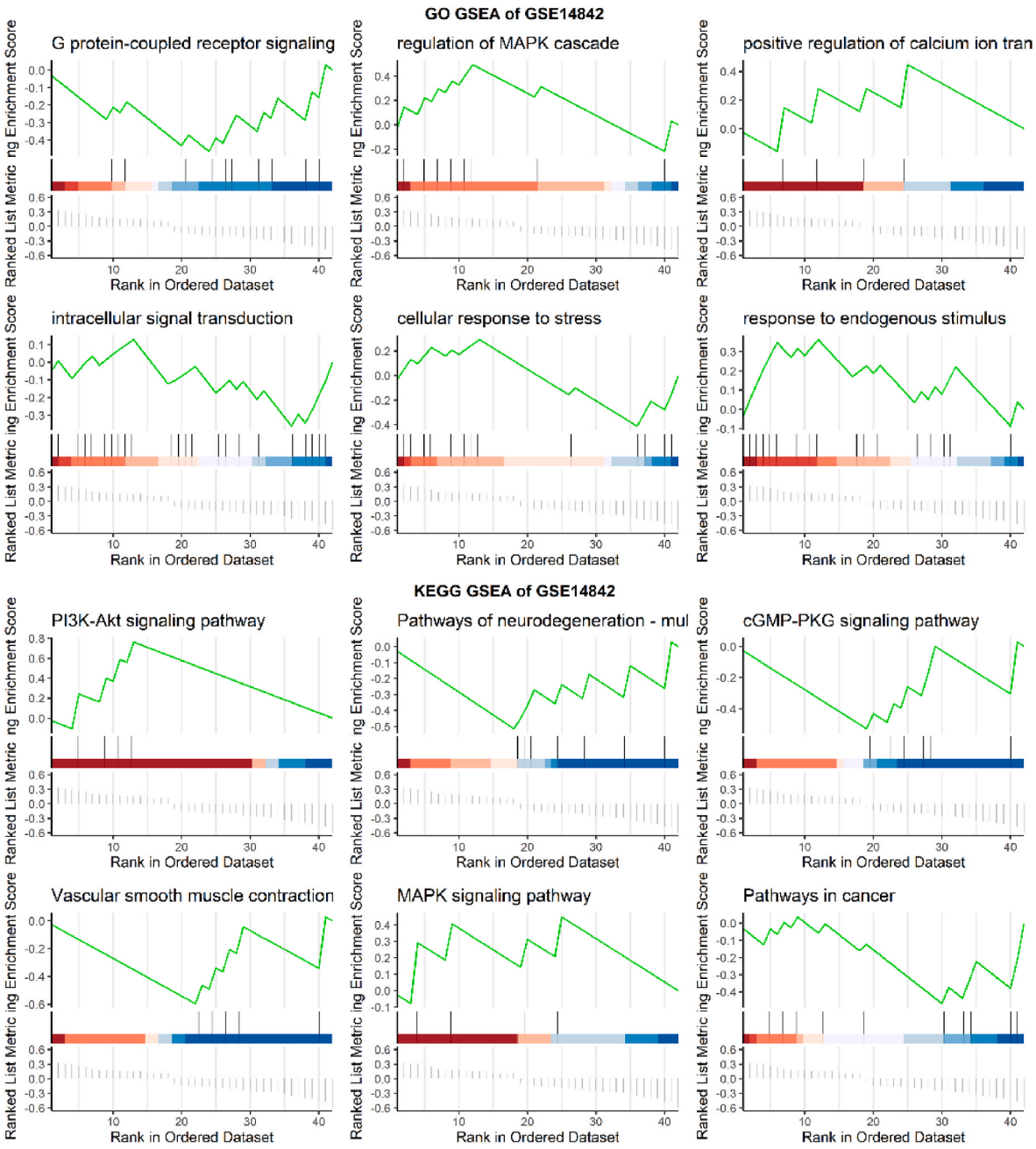

Fig. 15. GO and KEGG gene set enrichment analysis of GSE14842.

templates for the cGMP-dependent protein kinase, PI3KCγ, MAPK1, and VGCAB (Fig. 16). cGMP-dependent protein kinase template 6BDL scored 1780 for 84% identity, 16% gaps, and 84% gaps based on 84% identity, 16% gaps, and 84% gaps. A template with 90% identity, 10% gaps, and 5247 overall scores was used for the template 7MEZ. 91% of identical sequences in template 4FV6, 8%, and 1760 scores for MAPK1 in template 4FV6. VGCB1 had 7896 overall scores and 76% identity in template 7VFS.

In order to verify the accuracy of our protein models (Fig. 18A), we used a Ramachandran plot to illustrate amino acid distributions in phi and psi angles. According to the study, amino acid residue distributions for cGMP-dependent protein kinase, PI3KC, MAPK1, and VGCAB1 were 89.3% in favorable areas, 87.6% in favorable areas, 86.5% in favorable areas, and 89.7% in prohibited and disallowed areas, respectively. The model quality is then identified by calculating the z-score based on the separation energy between native and misfolded protein structures. Results showed that z–the score of cGMP–dependent protein kinase, PI3KCγ, MAPK1, and VGCAB1 protein models was −8.03, −14.17, −8.89, and −8.39, respectively (Fig. 18B).

3.8. Molecular docking

In order to determine where the ligand should be placed in the target protein's binding site, molecular docking calculations can be performed. An appropriate force field and physical energy components improve the accuracy of compound docking models [14,26,27]. In the docking experiment, the cGMP-dependent protein kinase model, PI3KC model, MAPK1 model, and VGCAB1 model were docked with the bioactive chemicals shown to positively influence target genes (Table 4, Fig. 19).

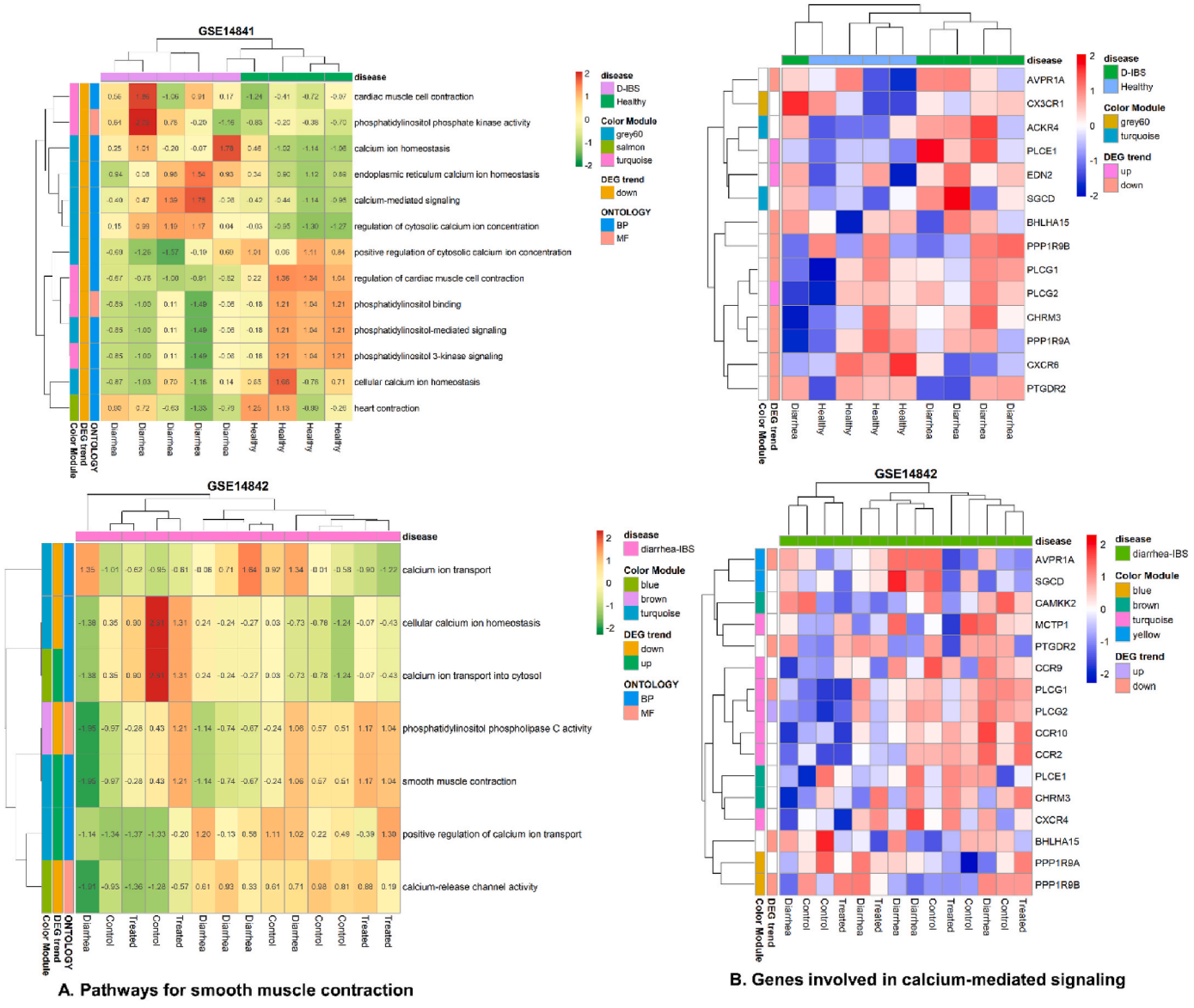

Fig. 16. Identification of calcium regulatory genes and functional pathways for smooth muscle contraction in DEGs and top 4 WGCNA modules of GSE14841 and GSE14842. **A.** Gene Ontology (GO) functional pathways for smooth muscle contraction. **B.** Regulatory genes involved in the calcium–mediated signaling pathway.

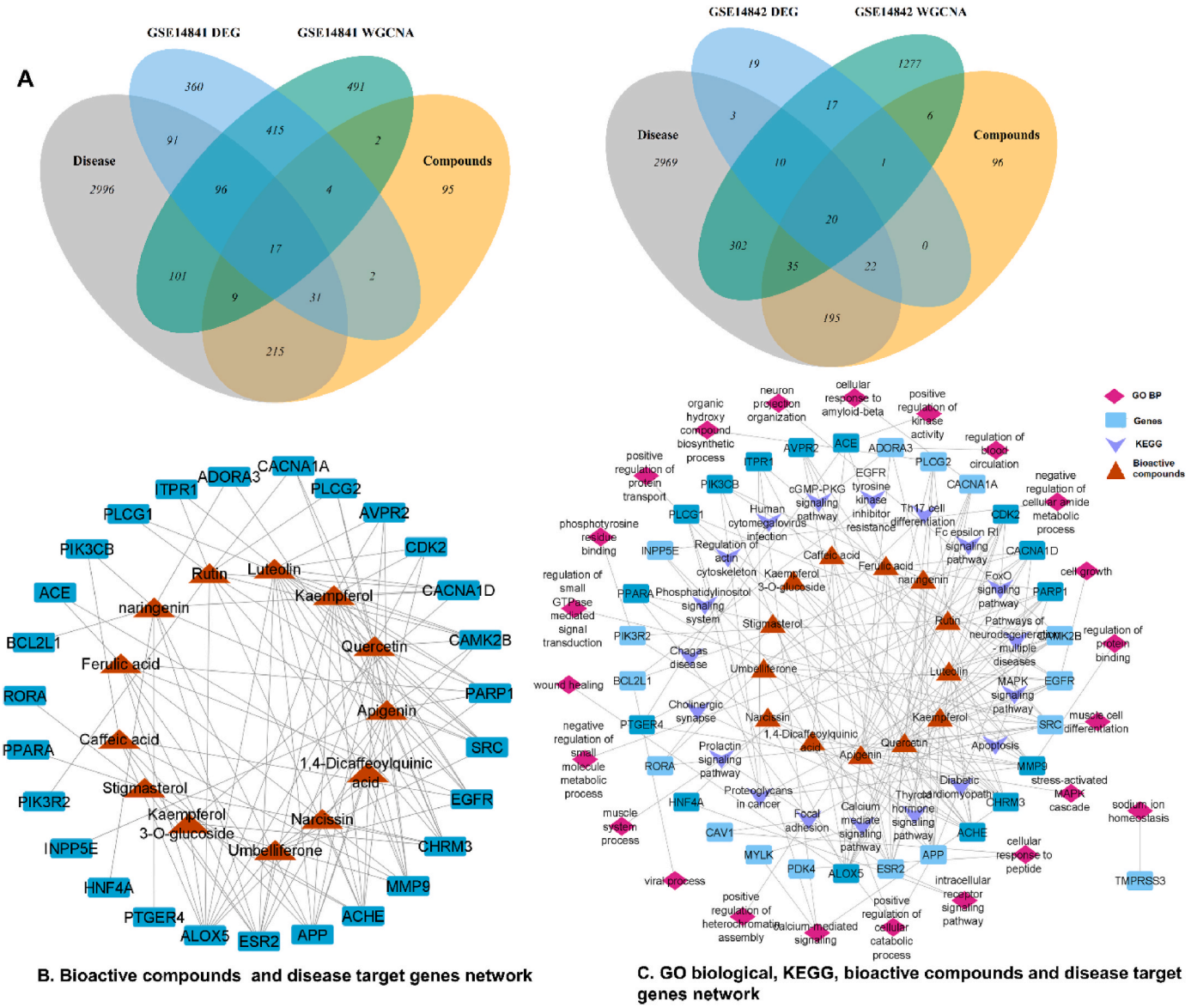

Fig. 17. Identification of key genes and network construction. **A.** Venn diagram of overlapped genes in disease–associated genes, compounds target genes, differentially expressed genes and WGCNA top 4 modules genes of GSE14841 and GSE14842. **B.** Compound and disease target genes network **C.** GO biological process and KEGG pathway network of bioactive compounds and target genes.

3.9. Molecular dynamics simulation

It is common to study protein-ligand complexes using MD simulations to determine their stability. In MD simulation, a dynamic change in binding modes was observed over time in protein-ligand complexes. In traditional MD simulations, a force field governs the forces between atoms and molecules. The protein-ligand complex was calculated throughout the simulation process for its total energy, potential energy, pressure, and temperature. The stability of complex systems of compounds and proteins, the stability of proteins after small molecule additions, and the hydrophobicity of amino acids, can be determined by measuring MD values such as RMSD, RMSF, Rg value, and SASA. Therefore, the protein-ligand complexes of rutin and cGMP-dependent protein kinase, PI3KCγ, MAPK1, were selected for MD simulations. The results are shown in Fig. 20.

3.9.1. RMSD

RMSD is a quantitative feature for evaluating the stability of the protein-ligand system. The RMSD of the protein backbone atoms in each complex remained low throughout the MD simulation, as shown in (Fig. 20 A). The averaged RMSD values were 0.3480 ± 0.04002, 0.5558 ± 0.08717, and 0.8197 ± 0.014 nm for the cGMP-dependent protein kinase-Rutin, MAPK1-Rutin, and PI3KCγ-Rutin docked complexes respectively.

3.9.2. RMSF

RMSF is an analytical method that can measure the fluctuation of each amino acid residue in protein in the overall period. The higher RMSF value shows that the residue has a significant fluctuation; on the contrary, a smaller RMSF value represents a small volatility of the residue. We evaluated the effect of rutin on the fluctuation of each protein residue by calculating the RMSF of backbone atoms for each protein residue in the complex. The averaged RMSF values were 0.1317 ± 0.07229, 0.1281 ± 0.06913, and 0.1531 ± 0.09328 nm for the cGMP-dependent protein kinase-Rutin, MAPK1-Rutin and PI3KCγ-Rutin docked complexes, respectively (Fig. 20 B). Significant conformational

Table 3
Physiochemical properties of homology models.

Parameters	cGMP–dependent protein kinase 1	PI3KCγ	MAPK1	VGCAB1
Molecular Weight	76364.48	126453.64	41389.71	212029.25
Number of amino acids residues	671	1102	360	1873
Maximum amino acids residues	8.9% Leu, 8.8% Lys, 8.8% Glu	11.1% Leu, 7.3% Lys, 6.6% Glu	11.9% Leu, 6.9% Ala, 6.7% Asp	11.5% Leu, 7.0% Ala, 7.0% Ile
Negatively charged residues (Asp + Glu)	104	137	45	199
Positively charged residues (Arg + Lys)	92	136	42	185
theoretical isoelectric point (pI)	5.74, indicating it is acidic	7.23	6.50	6.16
Instability index*	42.69	45.5	39.71	44.02
Aliphatic index	83.99	73.45	95.94	98.39
GRAVY score	−0.387	−0.457	−0.287	0.076
Extinction coefficient ($M^{-1}cm^{-1}$)	75915	156285	45185	229150

Instability index:≥40 is considered unstable.

fluctuations in the active sites were not found, and the binding residues with rutin were relatively stable.

3.9.3. Radius of gyration (Rg)

The gyratory radius is a physical parameter that measures the compactness of protein structures. A lower gyratory radius in a protein indicates a more compact structure associated with a more stable protein structure. The averaged Rg values were 2.089 ± 0.01038, 2.199 ± 0.01662, and 3.272 ± 0.01105 nm, respectively, for cGMP-dependent protein kinase-Rutin, MAPK1-Rutin and PI3KCγ-Rutin docked complexes. The radius of gyration trajectory is not aberrant since there are no significant variations (Fig. 20 D).

3.9.4. Solvent accessible surface area (SASA)

SASA measures the hydrophobicity of a protein, with larger SASA values indicating a larger protein volume and fewer simulation time fluctuations. It is possible to alter SASA by adding tiny compounds, sometimes significantly altering the structure of proteins. During the 10-ns simulation, compound-protein docked complexes were relatively stable, with average SASA areas were 175.4 ± 2.497, 181.9 ± 2.713, and 494.6 ± 6.215 nm^2 for the complexes involving cGMP-dependent protein kinase, MAPK1, and PI3KCγ. (Fig. 20 E).

3.9.5. Hydrogen bond

Hydrogen bond plays a vital role in maintaining the interaction of ligand and protein and aid in ligand recognition of the active site. To study the hydrogen bonding interaction between three protein-rutin complexes during the 10 ns MD simulation, the number, length, and angle of hydrogen bonds were analyzed using the gmx_hbond module in GROMACS. The average number of hydrogen bonds formed during 10ns MD were 5.193 ± 1.413, 2.737 ± 1.158, and 3.647 ± 1.327 bonds for the cGMP-dependent protein kinase-Rutin, MAPK1-Rutin, and PI3KCγ-Rutin docked complexes, respectively (Fig. 20C). The hydrogen bond interaction between the rutin and proteins remained relatively stable and continuous over simulation.

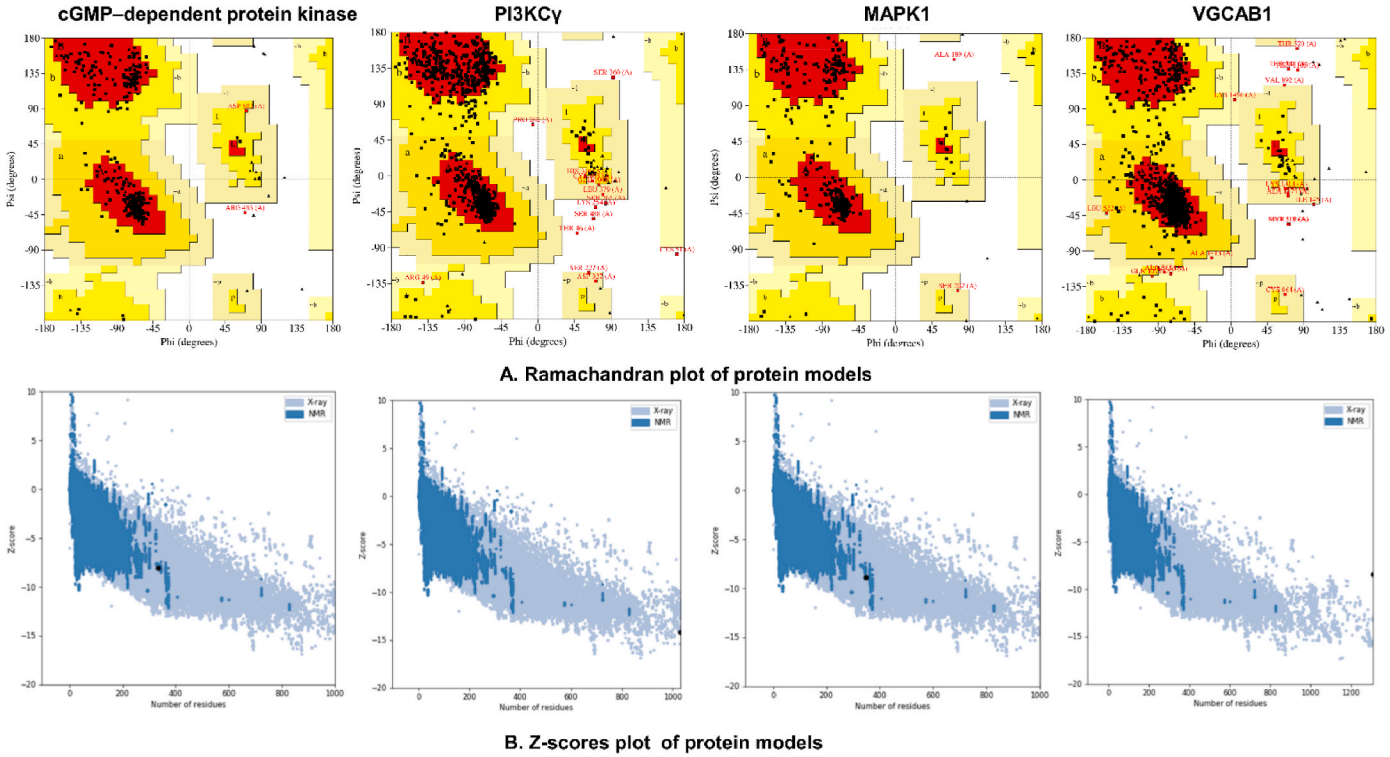

Fig. 18. Validation of cGMP–dependent protein kinase, PI3KCγ, MAPK1, and VGCAB1 models. **A.** Ramchandran plot of proteins to identify the distribution of amino acid residues. **B.** Z–scores plot of protein models.

Table 4
The binding energies (kcal/mol) of docked ligand–protein complex calculated with Prime MM–GBSA.

Compounds	Docking score (kcal/mol)	Glide energy kcal/mol)	ΔG Bind (kcal/mol)	pKi (μM)	ΔG Coulomb (kcal/mol)	ΔG Covalent (kcal/mol)	ΔG Hbond (kcal/mol)	ΔG Lipo (kcal/mol)	ΔG Packing (kcal/mol)	ΔG Solv GB (kcal/mol)	ΔG vdW (kcal/mol)	Residue–Ligand Interactions with Distance (Å)	
												Hydrogen Bonds	Electrostatic/Hydrophobic Bonds
cGMP–dependent protein kinase I α													
Rutin	−6.87 ± 0.26	−57.39 ± 1.69	−34.42 ± 0.44	−11.72 ± 1.17	−6.87 ± 0.26	3.94	−4.43	−14.36	−0.2	73	−50.39	Conventional Hydrogen Bond: Gly370 (2.76 Å), Asp484 (2.40 Å), Asn489 (2.90 Å), Asp502 (2.47 Å), Asp502 (2.10 Å), Gln402 (2.31 Å), Asp502 (2.35 Å), Glu445 (2.12 Å), Carbon–hydrogen Bond: Gly504 (2.80 Å), Asp502 (2.89 Å),	Pi–Anion: Asp502 (3.97 Å), Pi–Donor Hydrogen Bond: Phe505 (2.64 Å), Alkyl:Ile397 (5.00 Å), Pi–Alkyl:His396 (5.37 Å),
Verapamil	−6.18 ± 0.01	−49.97 ± 0.65	−20.89 ± 0.41	−5.84 ± 0.30	−6.18 ± 0.01	15.8	−2.02	−26.03	−0.75	93.35	−35.48	Conventional Hydrogen Bond: Gly370 (1.98 Å), Gly370 (2.20 Å), Carbon–hydrogen Bond: Glu488 (2.98 Å), Asp502 (2.66 Å), Glu488 (2.98 Å), Glu445 (2.79 Å), Glu439 (2.28 Å), Cys441 (2.49 Å),	Salt Bridge; Attractive Charge: Glu445 (2.28 Å), Attractive Charge: Asp502 (4.44 Å), Pi–Sigma: Val374 (2.56 Å), Alkyl: Ala388 (4.06 Å), Ala388 (4.03 Å), Val422 (3.73 Å), Cys441 (3.96 Å), Ile491 (4.14 Å), Val501 (4.77 Å), Leu366 (3.92 Å), Ile491 (4.83 Å), Pi–Alkyl: Phe371 (5.34 Å), Phe649 (4.49 Å), Ala388 (4.53 Å),
Quercetin	−5.64 ± 0.63	−51.07 ± 1.05	−26.27 ± 1.43	−8.18 ± 0.92	−5.64 ± 0.63	5.05	−4.36	−4.6	−2.21	40.28	−29.39	Conventional Hydrogen Bond: Gly370 (2.26 Å), Gly370 (2.09 Å), Phe371 (2.90 Å), Lys486 (2.40 Å), Glu445 (1.89 Å), Asp484 (1.87 Å), Asp484 (2.06 Å), Carbon–hydrogen Bond: Gly369 (2.77 Å),	Pi–Anion: Asp502 (3.71 Å),
Umbelliferone	−5.16 ± 1.00	−20.70 ± 0.28	−22.98 ± 0.58	−6.75 ± 1.56	−5.16 ± 1.00	0.58	−1.52	−12.87	−0.02	23.43	−12.38	Conventional Hydrogen Bond: Cys441 (1.93 Å), Asp502 (1.79 Å), Carbon–hydrogen Bond: Ala440 (2.65 Å),	Pi–Alkyl: Leu366 (4.84 Å), Val374 (4.62 Å), Ala388 (3.94 Å), Ile491 (4.47 Å), Val374 (4.15 Å), Ala388 (5.14 Å), Met438 (5.48 Å), Ile491 (5.26 Å), Val501 (4.12 Å),
Luteolin	−4.41 ± 0.40	−35.23 ± 1.37	−21.59 ± 0.30	−6.15 ± 0.85	−4.41 ± 0.40	5.17	−3.88	−3.51	−2.51	29.43	−25.64	Conventional Hydrogen Bond: Trp447 (1.94 Å), Lys486 (2.22 Å), Asp484 (1.92 Å), Asp484 (2.02 Å), Carbon–hydrogen Bond: Gly369 (2.87)	Pi–Anion: Asp502 (3.49 Å), Pi–Pi T–Shaped: Phe371 (5.26 Å),
Kaempferol	−4.36 ± 0.88	−37.48 ± 1.18	−16.41 ± 1.83	−3.90 ± 0.93	−4.36 ± 0.88	2.6	−2.13	−6.01	−2.1	37.45	−30.4	Conventional Hydrogen Bond: Lys390 (2.13 Å), Trp447 (1.96 Å), Lys486 (2.97 Å), Lys486 (3.00 Å), Lys486 (2.27 Å), Asp484 (2.91 Å),	Pi–Anion: Asp502 (3.10 Å), Asp502 (3.80 Å), Pi–Pi Stacked: Phe371 (4.75 Å),
Ferulic acid	−3.57 ± 0.42	−24.60 ± 1.49	−8.59 ± 0.77	−0.50 ± 1.59	−3.57 ± 0.42	1.83	−2.51	−8.56	−0.35	−51.43	−20.22		Salt Bridge; Attractive Charge: Lys486 (2.42 Å), Lys390 (2.24 Å), Lys390 (2.75 Å), Glu409 (2.01 Å), Pi–Alkyl: Phe371 (3.60 Å),
Apigenin	−3.51 ± 0.97	−32.14 ± 1.22	−11.45 ± 0.83	−1.74 ± 0.56	−3.51 ± 0.97	4.18	−0.98	−11.63	−0.51	33.84	−26.2		Pi–Anion: Glu445 (4.94 Å), Pi–Pi T–Shaped: Trp447 (5.83 Å), Pi–Alkyl: Val374 (4.96 Å), Val374 (4.01 Å), Ala388 (5.10

(*continued on next page*)

Table 4 (*continued*)

Compounds	Docking score (kcal/mol)	Glide energy kcal/mol)	ΔG Bind (kcal/mol)	pKi (μM)	ΔG Coulomb (kcal/mol)	ΔG Covalent (kcal/mol)	ΔG Hbond (kcal/mol)	ΔG Lipo (kcal/mol)	ΔG Packing (kcal/mol)	ΔG Solv GB (kcal/mol)	ΔG vdW (kcal/mol)	Residue–Ligand Interactions with Distance (Å)	
												Hydrogen Bonds	Electrostatic/Hydrophobic Bonds
													Å), Ile491 (5.13 Å), Val501 (4.40 Å),
Phosphoinositide 3–kinase gamma (PIK3CG)													
Rutin	−13.00 ± 0.90	−66.81 ± 1.62	−46.18 ± 0.77	−16.83 ± 0.63	−61.32	13.36	−4.92	−18.17	−1.51	70.66	−44.29	Conventional Hydrogen Bond: Ser806 (2.05 Å), Val882 (1.94 Å), Lys890 (2.77 Å), Lys890 (2.36 Å), Asp964 (2.33 Å), Asp950 (2.91 Å), Ala885 (1.73 Å), Glu880 (1.77 Å), Carbon–hydrogen Bond:Lys833 (2.98 Å), Lys890 (2.41 Å), Asp964 (2.53 Å), Asp950 (2.41 Å),	Pi–Sigma: Trp812 (2.79 Å), Pi–Sulfur:Met953 (3.94 Å), Pi–Lone Pair:Tyr867 (2.87 Å), Pi–Pi T–Shaped:Trp812 (5.26 Å), Trp812 (4.70 Å), Tyr867 (5.57 Å), Alkyl:Ala805 (4.06 Å), Alkyl: Met804 (5.37 Å), Pi–Alkyl: Met804 (5.48 Å), Met953 (5.21 Å), Ile831 (5.12 Å), Ile879 (5.34 Å),
Quercetin	−11.52 ± 0.45	−60.40 ± 1.69	−44.04 ± 0.55	−15.90 ± 1.45	−38.48	5.87	−4.04	−8.31	−1.04	47.38	−45.41	Conventional Hydrogen Bond: Lys802 (2.53 Å), Ser806 (2.52 Å), Val882 (1.99 Å), Asp964 (2.07 Å), Asp950 (2.05 Å), Asp964 (2.82 Å), Glu880 (1.80 Å), Ala885 (1.93 Å), Carbon–hydrogen Bond:Ser806 (2.64 Å),	Pi–Cation: Lys890 (3.98 Å), Pi–Sulfur: Met953 (3.81 Å), Pi–Sulfur: Met953 (3.77 Å), Alkyl: Met804 (5.21 Å), Pi–Alkyl: Ile831 (5.25 Å), Ile963 (5.23 Å), Ile831 (5.12 Å), Ile963 (4.71 Å),
Luteolin	−9.19 ± 0.68	−42.32 ± 1.94	−36.10 ± 1.23	−12.45 ± 0.40	−25.11	4.77	−2.38	−11.56	−0.07	34.11	−35.86	Conventional Hydrogen Bond: Ser806 (2.59 Å), Lys833 (3.02 Å), Val882 (1.93 Å), Asp950 (2.12 Å), Glu880 (1.85 Å), Carbon–hydrogen Bond: Lys833 (2.62 Å),	Pi–Anion: Asp964 (4.09 Å), Pi–Sulfur: Met953 (3.90 Å), Pi–Alkyl: Ile963 (4.97 Å), Ile831 (5.01 Å), Ile963 (4.67 Å),
Kaempferol	−9.06 ± 0.97	−44.93 ± 1.63	−35.54 ± 0.72	−12.21 ± 0.93	−22.81	3.89	−2.29	−12.82	−0.08	33.76	−35.19	Conventional Hydrogen Bond: Ser806 (2.61 Å), Lys833 (3.07 Å), Val882 (1.94 Å), Asp950 (2.11 Å), Glu880 (1.79 Å), Carbon–hydrogen Bond:Lys833 (2.68 Å),	Pi–Anion: Asp964 (4.10 Å), Pi–Sulfur:Met953 (5.51 Å), Met953 (3.89 Å), Pi–Pi T–Shaped:Tyr867 (5.82 Å), Pi–Alkyl:Ile963 (4.93 Å), Ile831 (5.05 Å), Ile963 (4.65 Å),
Apigenin	−8.69 ± 0.49	−34.12 ± 2.07	−35.45 ± 0.39	−12.17 ± 1.97	−17.52	3.78	−1.51	−11.53	−0.04	22.05	−30.69	Conventional Hydrogen Bond: Val882 (1.92 Å), Glu880 (1.72 Å), Carbon–hydrogen Bond: Lys833 (2.61 Å),	Pi–Anion: Asp964 (4.04 Å), Pi–Sulfur: Met953 (3.77 Å), Pi–Alkyl: Ile963 (5.20 Å), Pro810 (5.44 Å), Ile831 (5.15 Å), Ile963 (4.86 Å),
Umbelliferone	−6.84 ± 1.12	−26.16 ± 1.50	−31.32 ± 1.83	−10.37 ± 0.39	−16.59	2.58	−1	−12.05	−0.2	17.8	−21.86	Conventional Hydrogen Bond: Val882 (1.95 Å), Glu880 (1.81 Å),	Pi–Sulfur:Met953 (3.99 Å), Pi–Pi T–Shaped:Tyr867 (5.51 Å), Pi–Alkyl:Ile831 (4.72 Å), Met953 (5.41 Å), Ile963 (4.85 Å), Ile831 (5.12 Å), Ile879 (5.29 Å), Ile963 (4.50 Å),
Ferulic acid	−6.14 ± 0.89	−25.22 ± 1.56	−13.22 ± 0.95	−2.51 ± 1.24	44.96	3.72	−1.05	−16.58	−0.49	−16.38	−27.39	Conventional Hydrogen Bond: Val882 (2.45 Å), Glu880 (1.95 Å), Carbon–hydrogen Bond: Lys833 (2.58 Å),	Attractive Charge: Lys833 (3.78 Å), Pi–Sulfur: Met953 (4.27 Å), Pi–Pi T–Shaped:Tyr867 (5.19 Å), Alkyl:Ile881 (4.09 Å), Met953 (5.18 Å), Pi–Alkyl:Trp812 (5.40 Å), Ile831 (5.13 Å), Ile879 (4.85 Å), Ile963 (4.15 Å),
Verapamil	−5.87 ± 0.78	−40.67 ± 1.88	−12.08 ± 0.38	−2.02 ± 1.45	−5.44	17.32	−0.55	−24.26	−0.15	27.64	−26.65	Conventional Hydrogen Bond: Val882 (2.93 Å), Carbon–hydrogen Bond: Asp950 (2.55 Å), Asp950	Salt Bridge; Attractive Charge: Asp964 (3.10 Å), Attractive Charge: Asp950 (4.42 Å),

(*continued on next page*)

Table 4 (*continued*)

Compounds	Docking score (kcal/mol)	Glide energy kcal/mol)	ΔG Bind (kcal/mol)	pKi (μM)	ΔG Coulomb (kcal/mol)	ΔG Covalent (kcal/mol)	ΔG Hbond (kcal/mol)	ΔG Lipo (kcal/mol)	ΔG Packing (kcal/mol)	ΔG Solv GB (kcal/mol)	ΔG vdW (kcal/mol)	Residue–Ligand Interactions with Distance (Å)	
												Hydrogen Bonds	Electrostatic/Hydrophobic Bonds
												(2.46 Å), Asp950 (2.44 Å), Asp964 (3.07 Å), Asp964 (2.89 Å), Ala805 (2.67 Å),	Pi–Anion: Asp950 (4.38 Å), Pi–Donor Hydrogen Bond: Ser806 (2.37 Å), Pi–Sulfur: Met953 (3.84 Å), Alkyl: Met804 (5.15 Å), Ile831 (4.01 Å), Ile881 (4.24 Å), Met953 (5.18 Å), Val882 (3.96 Å), Met953 (4.30 Å), Ile963 (4.98 Å), Lys807 (4.83 Å), Leu1090 (5.39 Å), Pi–Alkyl: Trp812 (4.71 Å), Tyr867 (4.76 Å), His967 (5.14 Å), Ile831 (5.04 Å), Ile879 (5.49 Å), Ile963 (4.28 Å),
Mitogen-Activated Protein Kinase 1 (ERK2)													
Rutin	−11.54 ± 0.39	−67.59 ± 2.02	−68.97 ± 0.71	−26.72 ± 0.71	−75.66	10.66	−6.13	−14.04	−0.1	52.05	−35.76	Conventional Hydrogen Bond: Glu33 (2.76 Å), Lys54 (2.02 Å), Ser153 (2.00 Å), Asp167 (2.49 Å), Asn154 (1.83 Å), Ser153 (1.80 Å), Tyr30 (1.92 Å), Gln105 (1.59 Å), Met108 (1.78 Å), Met108 (1.88 Å), Carbon–hydrogen Bond: Gly32 (2.77 Å), Gly32 (2.72 Å), Thr110 (2.94 Å), Ser153 (3.08 Å), Tyr30 (2.95 Å), Tyr30 (2.80 Å), Glu33 (2.59 Å),	Pi–Sulfur: Cys166 (3.76 Å),
Quercetin	−10.38 ± 0.11	−50.90 ± 1.51	−35.99 ± 0.69	−12.40 ± 1.00	−36.17	6.31	−4.38	−6.81	−0.05	46.22	−41.11	Conventional Hydrogen Bond: Gln105 (3.02 Å), Lys114 (2.03 Å), Ser153 (2.01 Å), Asp167 (2.33 Å), Glu33 (1.91 Å), Asn154 (1.95 Å), Asp111 (1.84 Å), Met108 (1.78 Å), Carbon–hydrogen Bond: Ser153 (2.74 Å), Ser153 (2.86 Å), Glu33 (2.95 Å), Ser153 (2.44 Å),	Attractive Charge: Lys54 (4.46 Å), Pi–Sigma: Val39 (2.90 Å), Pi–Sulfur: Cys166 (3.87 Å), Pi–Alkyl: Cys166 (4.88 Å), Val39 (5.13 Å), Lys54 (4.81 Å), Ile31 (4.87 Å), Leu156 (4.50 Å),
Luteolin	−8.06 ± 0.53	−45.41 ± 1.46	−52.62 ± 1.99	−19.62 ± 1.98	−40.97	−4.77	−3.33	−9.32	−0.22	30.05	−24.06	Conventional Hydrogen Bond: Lys54 (1.94 Å), Met108 (2.14 Å), Glu33 (1.85 Å), Asp106 (1.71 Å), Asp106 (1.76 Å),	Pi–Sigma: Val39 (2.81 Å), Pi–Sulfur: Cys166 (4.27 Å), Pi–Alkyl: Val39 (4.89 Å), Val39 (5.37 Å), Ala52 (3.84 Å), Leu156 (4.32 Å),
Kaempferol	−6.75 ± 0.61	−41.04 ± 2.11	−36.21 ± 0.97	−12.50 ± 0.53	−33.29	2.99	−2.16	−10.29	−1.05	36.7	−29.1	Conventional Hydrogen Bond: Lys54 (1.99 Å), Met108 (2.34 Å), Gln105 (2.77 Å), Ser153 (2.98 Å), Asp106 (1.63 Å),	Pi–Sulfur: Cys166 (3.77 Å), Pi–Alkyl: Val39 (4.84 Å), Val39 (5.45 Å), Ala52 (3.93 Å), Leu156 (4.25 Å), Cys166 (5.17 Å),
Apigenin	−6.38 ± 0.93	−41.24 ± 1.69	−51.27 ± 0.53	−19.04 ± 0.96	−40.96	−3.81	−2.8	−9.41	−0.19	29.02	−23.11	Conventional Hydrogen Bond: Lys54 (1.95 Å), Met108 (2.18 Å), Glu33 (1.82 Å), Asp106 (1.67 Å),	Pi–Sigma: Val39 (2.83 Å), Pi–Sulfur: Cys166 (4.24 Å), Pi–Alkyl: Lys54 (5.47 Å), Val39 (4.83 Å), Val39 (5.42 Å), Ala52 (3.81 Å), Leu156 (4.31 Å),
Ferulic acid	−5.86 ± 0.75	−27.68 ± 1.94	−24.25 ± 1.90	−7.30 ± 1.49	27.42	0.22	−1.92	−12.54	0	−12.83	−24.58	Conventional Hydrogen Bond: Met108 (2.24 Å), Asp106 (1.76 Å), Carbon–hydrogen Bond: Met108 (2.66 Å),	Salt Bridge; Attractive Charge: Lys54 (2.19 Å), Alkyl: Ile31 (5.21 Å), Leu156 (4.26 Å), Pi–Alkyl: Val39 (5.26 Å), Ala52 (3.92 Å), Leu156 (4.34 Å),
Umbelliferone					−17.85	0.29	−1.05	−8.44	0	13.72	−20.22		

(*continued on next page*)

Table 4 (*continued*)

Compounds	Docking score (kcal/mol)	Glide energy kcal/mol)	ΔG Bind (kcal/mol)	pKi (μM)	ΔG Coulomb (kcal/mol)	ΔG Covalent (kcal/mol)	ΔG Hbond (kcal/mol)	ΔG Lipo (kcal/mol)	ΔG Packing (kcal/mol)	ΔG Solv GB (kcal/mol)	ΔG vdW (kcal/mol)	Residue–Ligand Interactions with Distance (Å)	
												Hydrogen Bonds	Electrostatic/Hydrophobic Bonds
	−5.71 ± 0.83	−26.50 ± 1.63	−33.56 ± 0.73	−11.35 ± 1.11								Conventional Hydrogen Bond: Met108 (1.88 Å), Gln105 (1.66 Å), Carbon–hydrogen Bond: Leu107 (2.71 Å),	Pi–Sigma: Leu156 (2.72 Å), Pi–Sulfur: Cys166 (4.42 Å), Pi–Alkyl: Ile31 (5.26 Å), Val39 (5.25 Å), Ala52 (4.36 Å), Val39 (4.36 Å), Ala52 (5.11 Å), Leu156 (5.09 Å),
Verapamil	−4.59 ± 1.23	−44.64 ± 2.07	−33.19 ± 1.10	−11.19 ± 0.99	−2.29	7.91	−2.6	−15.6	−0.62	20.58	−40.56	Conventional Hydrogen Bond: Glu33 (2.10 Å), Lys54 (2.43 Å), Lys54 (2.50 Å), Lys151 (2.45 Å), Lys151 (2.32 Å), Carbon–hydrogen Bond: Gly32 (2.70 Å), Ile31 (2.65 Å), Ile31 (2.76 Å), Ser153 (2.49 Å), Ser153 (2.79 Å), Ser153 (2.94 Å), Asp167 (2.93 Å), Glu71 (2.57 Å), Gln105 (2.62 Å), Gln105 (2.50 Å),	Salt Bridge; Attractive Charge: Asp111 (2.86 Å), Pi–Sulfur: Cys166 (3.84 Å), Pi–Pi T–Shaped: Tyr113 (5.16 Å), Alkyl: Lys151 (4.55 Å), Lys54 (4.53 Å), Cys166 (4.50 Å), Pi–Alkyl: Val39 (4.59 Å), Lys54 (5.36 Å),
Voltage–dependent L–type calcium channel subunit α													
Rutin	−11.14 ± 1.50	−68.22 ± 1.50	−31.35 ± 0.22	−10.39 ± 0.45	−34.79	4.19	−2.82	−19.01	−3.47	80.26	−55.72	Conventional Hydrogen Bond: Asn649 (1.79 Å), Glu292 (2.12 Å), Gly613 (2.71 Å), Met291 (2.94 Å), Glu292 (2.57 Å), Thr1321 (1.78 Å), Carbon–hydrogen Bond: Asn649 (2.48 Å), Thr612 (2.51 Å), Asn649 (2.76 Å), Thr612 (2.53)	Pi–Pi T–Shaped: Phe656 (5.31 Å), Phe1013 (4.91 Å), Pi–Alkyl: Ala1053 (4.43 Å), Ala1053 (4.60 Å), Leu652 (4.58 Å), Ala1053 (5.03 Å),
Kaempferol	−9.53 ± 0.87	−33.79 ± 1.56	−32.42 ± 0.36	−10.85 ± 0.37	−5.47	0.72	−0.16	−13.18	−1.14	21.44	−34.63		Pi–Alkyl: Leu566 (5.01 Å), Ile1050 (3.97 Å), Leu566 (4.82 Å), Ile1050 (4.44 Å), Leu652 (4.43 Å), Ala1053 (5.39 Å),
Luteolin	−9.44 ± 0.47	−32.96 ± 2.04	−25.48 ± 0.39	−7.84 ± 0.20	−5.03	1.32	−0.19	−9.34	−1.16	23.01	−34.09	Conventional Hydrogen Bond: Phe608 (2.79 Å), Pi–Donor Hydrogen Bond: Phe567 (3.06 Å),	Pi–Sigma: Ile1050 (2.90 Å), Pi–Alkyl: Leu566 (5.31 Å), Leu652 (5.04 Å), Leu652 (4.43 Å), Leu566 (4.88 Å), Ile1050 (4.89 Å),
Apigenin	−8.93 ± 1.04	−31.61 ± 0.40	−30.27 ± 0.44	−9.92 ± 1.98	−4.12	0.34	0	−11.55	−1.1	20.04	−33.88	Carbon–hydrogen Bond: Thr612 (2.56 Å),	Pi–Alkyl: Leu566 (4.96 Å), Ile1050 (4.00 Å), Leu566 (4.84 Å), Ile1050 (4.47 Å), Leu652 (4.51 Å), Ala1053 (5.34 Å),
Quercetin	−7.03 ± 0.88	−55.01 ± 1.28	−13.12 ± 0.41	−2.47 ± 0.53	−48.67	6.02	−3.72	−8.11	−1.39	82.25	−39.52	Conventional Hydrogen Bond: Tyr1365 (2.18 Å), Thr1321 (2.01 Å), Thr1012 (1.92 Å), Leu611 (2.07 Å), Asn649 (2.55 Å), Glu614 (2.94 Å), Glu1014 (2.06 Å), Glu292 (1.90 Å), Carbon–hydrogen Bond: Glu614 (2.74 Å),	Pi–Pi T–Shaped: Phe1013 (4.99 Å), Phe1013 (5.06 Å),
Verapamil	−6.36 ± 0.80	−50.14 ± 1.50	−58.94 ± 1.43	−22.37 ± 0.96	10.3	7.49	−0.16	−30.35	−1.34	7.06	−51.95	Conventional Hydrogen Bond: Asn649 (2.70 Å), Carbon–hydrogen Bond: Leu611 (2.56 Å), Asn649 (2.69 Å), Thr612 (2.85 Å), Asn649 (2.55 Å), Ile289 (2.50 Å), Ile289 (2.98 Å),	Pi–Pi T–Shaped: Phe645 (5.13 Å), Alkyl: Ala1053 (4.34 Å), Ile289 (4.86 Å), Ile570 (5.43 Å), Leu611 (4.25 Å), Leu652 (4.85 Å), Ile1050 (4.10 Å), Pi–Alkyl: Phe608 (4.33 Å), Phe645 (4.83 Å), Phe656 (5.42 Å), Leu652 (4.25 Å), Ala1053 (5.03 Å),
Umbelliferone					−5.72	1.46	−0.48	−13.06	−0.91	12	−22.61		

(*continued on next page*)

Table 4 (*continued*)

Compounds	Docking score (kcal/mol)	Glide energy kcal/mol)	ΔG Bind (kcal/mol)	pKi (μM)	ΔG Coulomb (kcal/mol)	ΔG Covalent (kcal/mol)	ΔG Hbond (kcal/mol)	ΔG Lipo (kcal/mol)	ΔG Packing (kcal/mol)	ΔG Solv GB (kcal/mol)	ΔG vdW (kcal/mol)	Residue–Ligand Interactions with Distance (Å)	
												Hydrogen Bonds	Electrostatic/Hydrophobic Bonds
	−5.97 ± 0.57	−22.49 ± 0.73	−29.33 ± 0.58	−9.51 ± 1.49								Conventional Hydrogen Bond: Leu611 (2.33 Å),	Pi–Alkyl: Leu652 (4.58 Å), Ile1050 (5.05 Å), Ala1053 (5.02 Å), Leu652 (4.12 Å),
Ferulic acid	−5.69 ± 0.58	−19.82 ± 1.05	−20.57 ± 0.30	−5.70 ± 1.11	41.39	1.01	−0.08	−16.99	−1.16	−17.71	−27.02		Alkyl: Ala1053 (4.01 Å), Pi–Alkyl: Phe656 (5.15 Å), Leu652 (4.62 Å),

Values are expressed as Mean ± SD, $n = 3$. ΔGBinding: Binding free energy; pKi: Logarithmic of Inhibition Constant (Ki); ΔGCoulomb: Coulomb binding energy; ΔGCovalent: Covalent binding energy; ΔGH: Hydrogen bonding energy; ΔGLipophilic: Lipophilic binding energy; ΔGSolv GB: Generalized born electrostatic solvation energy; ΔGvdW: Van der Waals forces energy; These energies all contribute to Binding free energy (ΔGBinding).

3.9.6. Binding energies

The binding free energy of the complex system was computed using MM-PBSA in gmx-MMPBSA tools to determine which configuration is more advantageous for binding to protein and study the interaction between PI3KCγ, MAPK1, and cGMP-dependent protein kinase and rutin. In the case of negative Gibbs free energy and enthalpy values, ligand binding is exothermic, and the complexes formed are thermodynamically stable (Table 5). In Table 5, rutin exhibit a stronger bond with MAPK1, and has the highest Gibbs free energy (8.5 kcal/mol). Gibbs free energy contains a considerable amount of entropy, so neglecting it may change the stability of complexes.

3.9.7. Principal component analysis and free energy landscape (FEL)

The PCA technique often reduces dimensionality in massive datasets to extract significant observations. We analyzed the mobility modes of docked complexes of PI3KCγ, MAPK1, and cGMP-dependent protein kinase using PCA analysis. PCA plots of docked complexes of PI3KCγ-Rutin, MAPK1-Rutin, and cGMP-dependent protein kinase are shown in Fig. 21A. As a result of the binding of rutin, stable complexes were formed. An analysis of the dynamic covariance matrix of docked protein complexes was conducted to find residues associated with Rutin or anti-correlated in motion. Fig. 21B presents the covariance matrix for PI3KCγ-Rutin, MAPK1-Rutin, and cGMP-dependent protein kinase complexes. The correlation runs from −1 to 1, according to the color intensities.

In order to examine the low energy conformations in the test systems, free energy landscape studies were performed on cGMP-dependent protein kinase-Rutin, PI3KCγ-Rutin, and MAPK1-Rutin. We plotted the free energy graphs in 3D and 2D using the first and second primary components. Fig. 21C presents the free energy landscapes of cGMP-dependent protein kinase-Rutin, PI3KCγ-Rutin, and MAPK1-Rutin. Blue dots indicate energetically suitable conformations on the free energy landscape, while red dots indicate energetically unfavorable conformations. MAPK1-Rutin's free energy landscape, which exhibited more intense blue dots than cGMP-dependent protein kinase and PI3KCγ, suggests that rutin decreased the energy of the MAPK1 complex by binding to its active site.

4. Discussion

It is necessary to have a comprehensive understanding of drugs and targets in order to discover new drugs, as well as comparative agents and targets. These include poor binding agents and nonbinding agents that facilitate discovery tools, prodrugs that improve therapeutics, co-targets of therapeutic targets used in multi-target strategies and off-target studies. The databases available do not adequately cover such valuable data. When metabolic or genome profiling is conducted using case-control studies, there is the possibility of confounding experimental or biological variations that may negatively affect the validity of the results. Therefore, the normalization of metabolic or genome profiles in case-control studies has been achieved through a variety of methods [28,29].

Data from the World Health Organization indicate that infectious diarrhea is the leading cause of death globally [30]. Several immunological indicators in the stools of patients suffering from IBD, IBS, or diarrhea indicate intestinal inflammation. The IBS datasets also revealed a high expression of genes involved in inflammatory and proinflammatory pathways. MAPK, AMPK, EGFR, and JAK-STAT were the most frequently enriched signaling pathways. Activating MAPK signaling requires the activation of transcription factors in the nucleus and cytoplasm by the toll-like receptor (TLR) expressed on cell surfaces. Thus, inflammatory cytokines and costimulatory elements could trigger inflammation [31]. The MAPK signaling pathway, therefore, dramatically influences IBD pathogenesis. The expression of EGFR and MAPK1 is associated with inflammation associated in the GSE14841 and GSE14842 datasets of IBS. Several recent studies have demonstrated

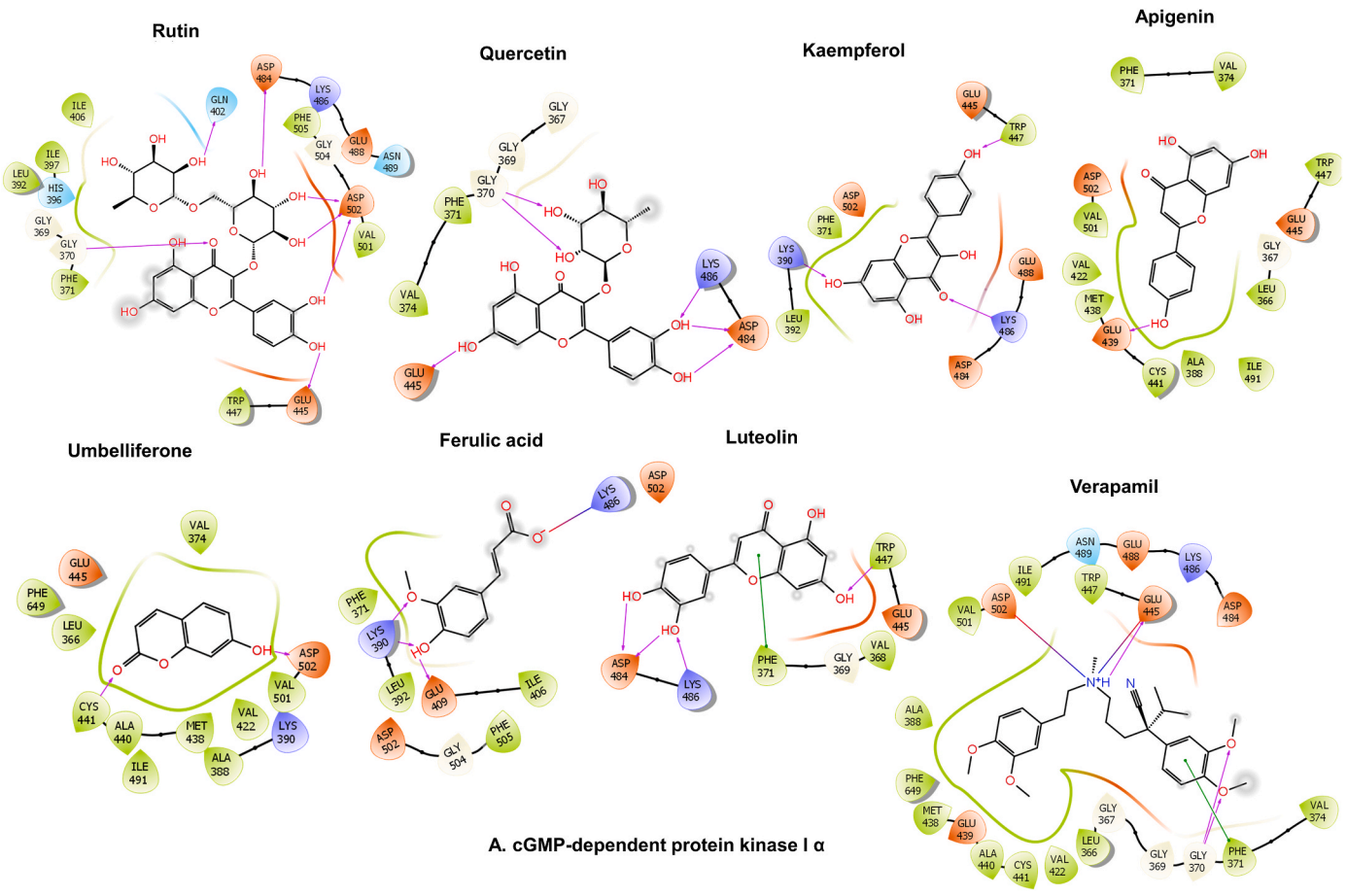

Fig. 19. 2D ligand–protein interaction between bioactive compounds of Cm.EtOH and proteins; **A.** cGMP–dependent protein kinase I α**B.** Phosphoinositide 3–kinase gamma (PIK3CG) **C.** Mitogen-Activated Protein Kinase 1 (ERK2) **D.** Voltage–dependent L–type calcium channel subunit α.

that plant extracts inhibit MAPK to reduce inflammation in the body [32].

In 2007, Hopkins [33] argued that by evaluating drug or ligand cellular processes, network pharmacology elucidates the link between bioactive ingredients, various targets, and pathways of complex diseases [34]. Network pharmacology has recently evolved as a new tool for identifying cellular pathways and emphasizing the active compounds of herbs [35]. In computational investigations, bioactive compounds were predicted to interfere with calcium mediated signaling for antispasmodic action. According to KEGG and GO pathway analyses, the bioactive compounds interacted with target genes involved in smooth muscle contraction through calcium-mediated signaling, cGMP-dependent protein kinase, PI3KC and MAPK1 pathways. In molecular docking, rutin was found with high binding affinity with these proteins. Consequently, the significant antispasmodic activity of Cm.EtOH may be related to the high binding affinity of compounds for target proteins, which blocks the contraction-causing signal transduction.The detail mechanism of these proteins in calcium smooth muscle contraction is illustrated in Fig. 22.

IBS–D has been associated with several pathologies, including abnormal intestinal motility, visceral hypersensitivity, and immunological activation [1]. It has been shown in numerous animal studies that hypertensive contractions of the intestinal smooth muscle cause the primary symptoms of IBS-D [36,37]. The preparation of tracheal tissues, urinary bladders, and jejunum was examined to determine the mechanism by which Cm.EtOH reduces smooth muscle tension. These target genes directly or indirectly have a pivotal role in smooth muscle contraction with calcium-mediated signaling and smooth muscle contraction. In molecular docking, rutin and quercetin had a binding affinity with L-type voltage-gated calcium ion channel (genes: CACNA1C, CACNA1D) and phosphoinositide phospholipase C (gene: PLCB, PLCE), myosin light chain kinase (genes: MYLK, MYL9), and calcium/-calmodulin kinase (CAMK2B). Hence, it can be assumed that strong antispasmodic activity of *C. melo* was due to the strong binding affinity of quercetin and rutin towards target proteins, i.e., L type voltage-gated calcium ion channel and phosphoinositide phospholipase C, myosin light chain kinase, and calcium/calmodulin kinase. It blockaded the signal transduction responsible for contraction. These proposed GSEA, GO and KEGG pathways were verified with *in vitro* and *in vivo* experimentation. Both experiments were testified on jejunum, trachea, and urinary bladder for calcium signal transduction pathway on K^+ (80 mM) and calcium concentration-response curves. We investigated the impact of calcium ions to determine how Cm.EtOH alleviated muscle tension. A well-known physiological process, "excitation-contraction," is essential for maintaining intracellular calcium homeostasis, which is essential for relaxed and contracted smooth muscles [19].

Numerous physiological mediators mediate the stimulatory effects in the gut by increasing cytosolic calcium levels, either through extracellular calcium influx or release from cytosolic stores to elicit depolarization of the resting action potential of tissue preparations. L-type voltage-dependent calcium channels regulate calcium homeostasis and smooth muscle contraction through calcium inward currents [38]. Calcium entry from extracellular fluid or calcium release from the endoplasmic reticulum causes the smooth muscle of the intestinal wall to contract spontaneously. These physiological mediators mediate the stimulatory effects in the gut. Increases in cytosolic calcium levels,

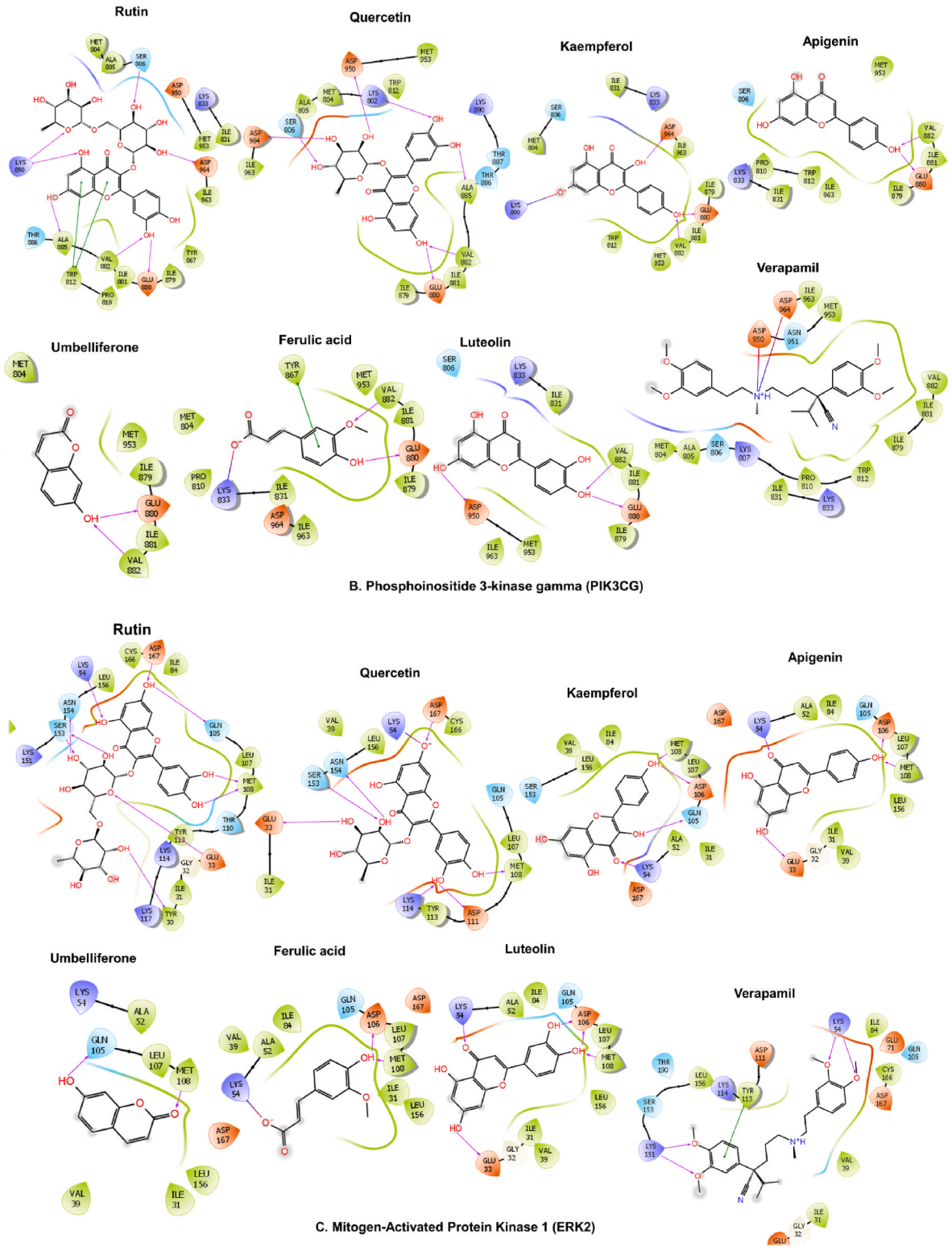

Fig. 19. (*continued*).

whether from external calcium influx or calcium release from cytosolic endoplasmic reticulum storage, elicit depolarization of the resting action potential of jejunum preparations and spontaneous contractions. In hyperactive gastrointestinal illnesses, any drug that can inhibit this mechanism is considered an active treatment agent [17,39] and a known antispasmodic agent [20]. Cm.EtOH was tested for its antidiarrheal and antispasmodic activity at isolated tissue contractions in a tissue organ bath. Cm.EtOH eases smooth muscle spasms by reducing contractions and inhibiting calcium ions influx into the cell [40,41]. The smooth muscle relaxant potential of Cm.EtOH was further examined against potassium chloride (80 and 25 mM) spastic contractions to ascertain whether it interfered with calcium ions channel inhibition or potassium ions channel activation. The potassium chloride (80 mM) triggered an intense depolarization of the membrane action potential of the cells,

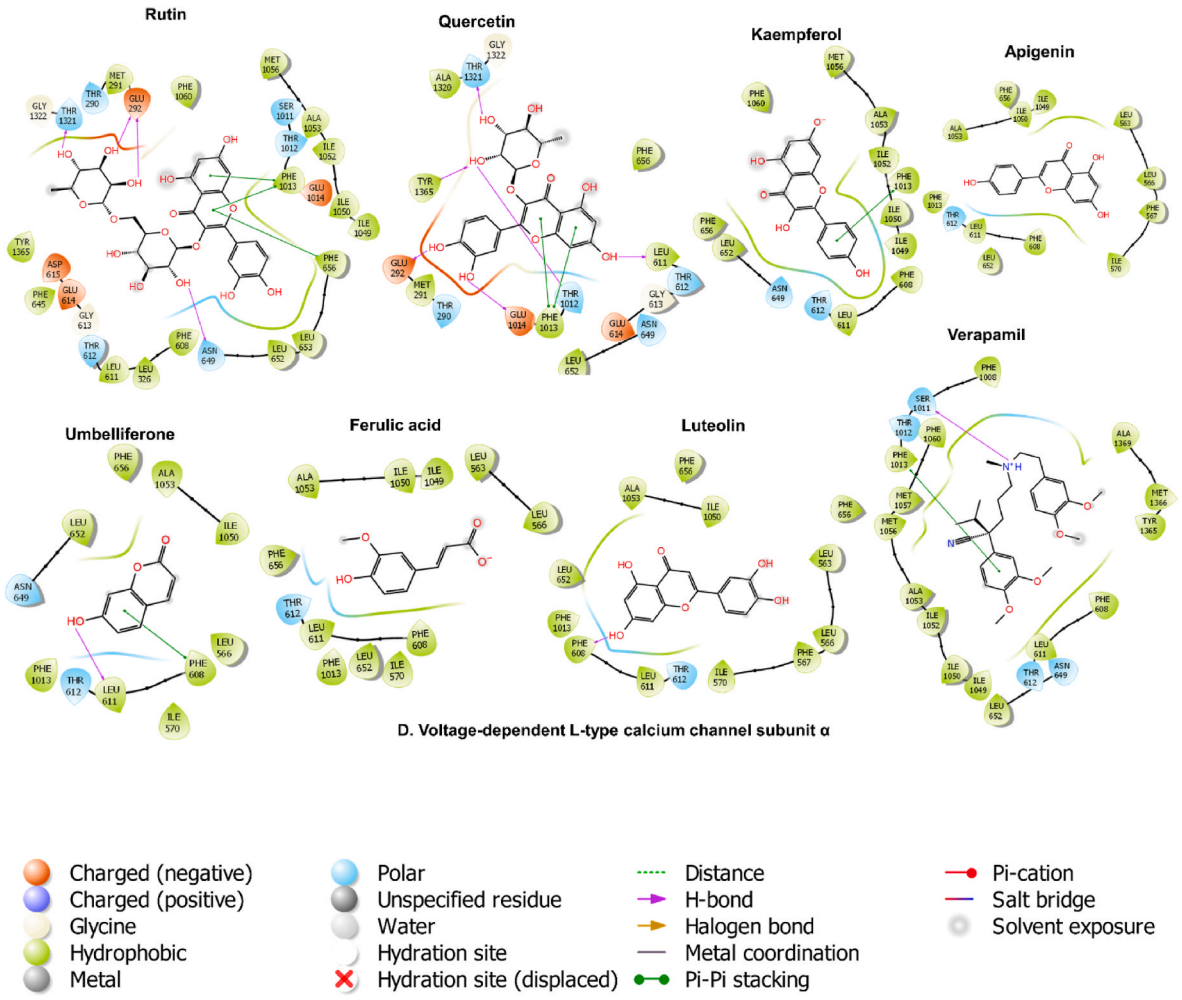

Fig. 19. (*continued*).

associated with increases in calcium inward current that produced a prolonged contractile response [17]. Cm.EtOH repolarized this intense depolarization of membrane action potential to relax smooth muscle and obstruct the influx of calcium current. It was predicted that the following chronicle events would be interrupted [19,39], i.e., 1) the concentration of cytosolic calcium ions was reduced due to a reduction in calcium inward current, 2) Because there was insufficient interaction with regulatory protein phosphokinase C, with this calcium–calmodulin complex was not formed, 3) in the absence of calcium–calmodulin, myosin light chain kinase (MLCK) failed to activate, which resulted in a reduction in myosin light chain (MLCs) phosphorylation and 4) This reduction decreased the availability of phosphorylated MLCs, resulting in the loss of myosin and actin filament crosslinking and the absence of a contractile response [20]. The pretreatment of the jejunum and urinary bladder tissue with Cm.EtOH suppressed calcium CRCs and induced a rightward shift comparable to verapamil [42], indicating that Cm.EtOH repolarized the membrane action potential by blocking calcium ion channels [17]. The potassium ions channel also had a critical role in smooth muscle contraction. Cm.EtOH was studied for potassium ion channels. In GI smooth muscles, a range of potassium ion channels is present, including voltage-gated potassium ion channels, K_A channels, calcium-activated potassium ion channels, and ATP–sensitive potassium ion channels [37,43]. However, voltage-gated potassium ion channels are among the most important channels that may regulate the resting potential of a cell [37]. Potassium ion channel openers are substances that reduce potassium chloride (25 mM) elicited contractions. In comparison, calcium channel blockers also have the propensity to inhibit potassium chloride (80 and 25 mM) elicited induced contractions [44]. Therefore, Cm.EtOH and verapamil effectively relax both spastic contractions [45]. It is known that muscarinic agonists (Ach, carbachol) cause muscular contractions by triggering the inflow of calcium ions into the cell or intracellular cellular calcium release. Thus, we assumed that Cm.EtOH reduced carbachol (1 μM) induced contraction may be mediated through the calcium signaling pathway. The muscarinic receptors share the same calcium mediate signaling pathway for smooth muscle contractile response [17,46]—hence, we determined antispasmodic activities of Cm.EtOH by causing depolarization of the action potential tracheal and urinary bladder tissue preparation with carbachol (1 μM) and K^+(80 mM)-induced contractions [47]. The pretreatment of Cm. EtOH on tracheal preparations caused a rightward shift in carbachol DRCs, such as the verapamil validated hypothesis [18]. This antimuscarinic response was produced due to the blockade of phosphoinositide phospholipase C (PLC), an active member in calcium mediates signaling. Phosphoinositide phospholipase C, a key enzyme present under cell members, promotes signal transduction of M_3 muscarinic receptor to induce contraction in smooth muscles. The activation of the M_3 muscarinic receptor stimulates the PLC, which hydrolyzes phosphatidylinositol 4,5-bisphosphate into two secondary messengers; inositol 1,4,5-trisphosphate (IP_3) and diacylglycerol (DAG). IP_3 stimulates inositol 1,4,5-trisphosphate receptors (IP_3R) on the sarcoplasmic reticulum to release calcium ions, increasing cytosolic calcium levels. DAG, along with calcium, activates a regulatory protein kinase C (PKC, gene: PRKCA), through which phosphorylation of calmodulin occurs to form a calcium/calmodulin complex. This calcium/calmodulin complex

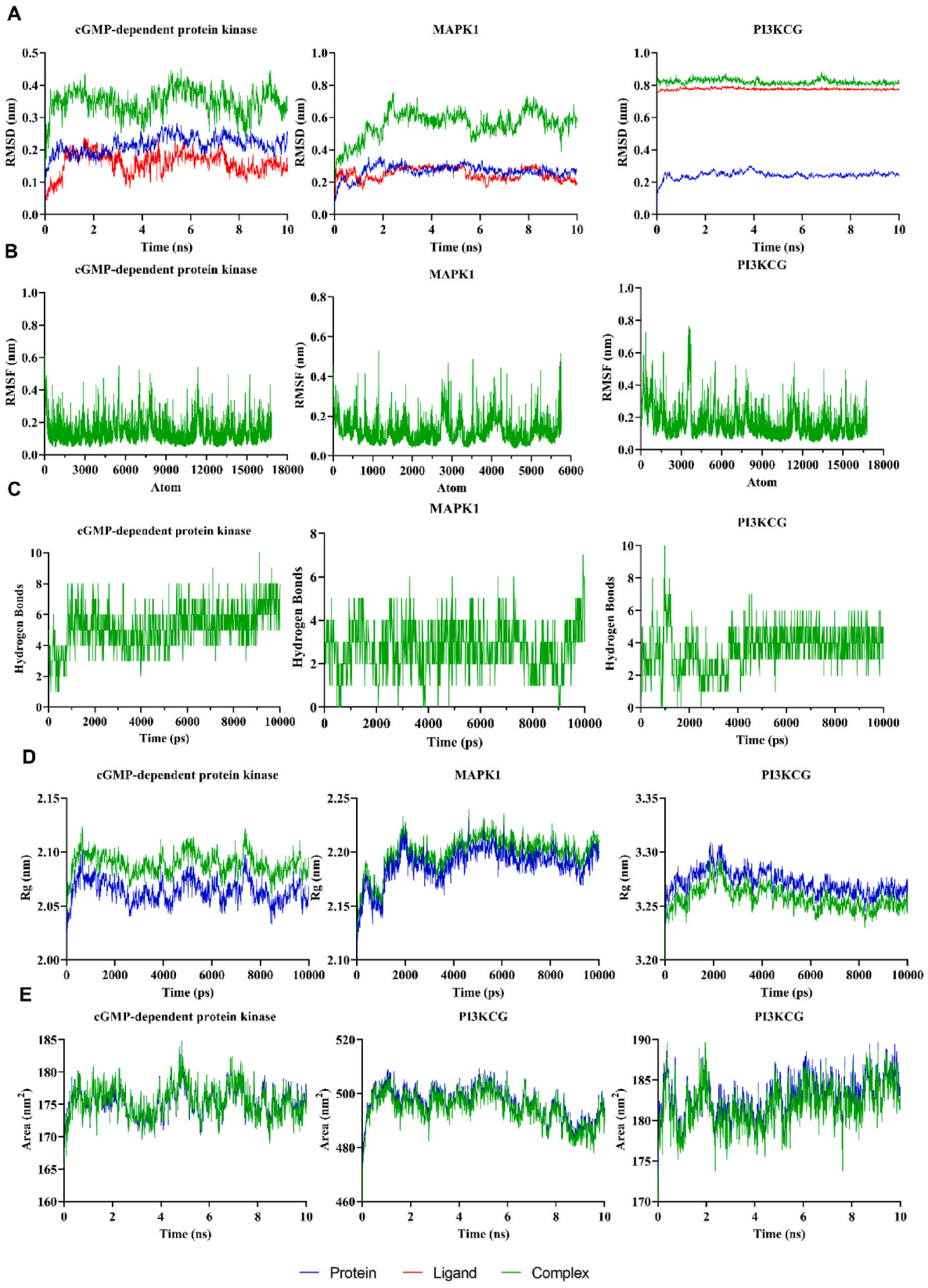

Fig. 20. The MD simulation trajectory analysis of cGMP-dependent protein kinase-Rutin, MAPK1-Rutin, and PI3KCγ-Rutin docked complexes for 10 ns. **A.** RMSD **B.** RMSF **C.** numbers of hydrogen Bonds **D.** Radius of gyration (Rg) **E.** Solvent accessible surface area (SASA).

Table 5
The MMPBSA binding energy of MD simulation trajectories over 10 ns.

	cGMP-dependent kinase	MAPK1	PI3KCG
ΔE_{VDW}	−27.05 ± 3.77	−38.54 ± 2.32	−39.88 ± 3.33
ΔE_{EL}	−108.37 ± 7.38	−47.77 ± 10.21	−70.93 ± 9.18
ΔE_{PB}	116.25 ± 9.8	67.86 ± 7.42	81.34 ± 8.59
$\Delta E_{NONPOLAR}$	−28.68 ± 1.24	−31.56 ± 1.93	−31.42 ± 1
ΔE_{DISPER}	55.36 ± 1.58	58.51 ± 1.38	60.32 ± 1.45
ΔG_{GAS}	−135.42 ± 6.71	−86.31 ± 10.74	−110.81 ± 9.5
ΔG_{SOLV}	142.93 ± 9.87	94.81 ± 6.9	110.23 ± 8.86
ΔTotal	7.51 ± 7.04	8.5 ± 6.36	−0.57 ± 4.22

E_{VDW}: van der waals, E_{EL}: electrostatic interactions, EPB: Polar contribution to solvation energy by PB method. $E_{NONPOLAR}$: non-polar contribution to solvation energy from repulsive solute-solvent interactions for PB. E_{DISPER}: non-polar contribution to solvation energy from attractive solute-solvent interactions for PB.G_{GAS}: Gas phase MM energy, including all bonded and non-bonded terms. G_{SOLV}: solvation energy.

activates another myosin light chain kinase (MLCK) that causes phosphorylation of myosin light chains (MLCs), phosphorylated MLCs, and actin form an interaction network to produce a contractile respons [17,19,38]. Hence, Cm.EtOH exerted its bronchodilator and dysuria action by decreasing cytosolic calcium release from sarcoplasmic reticulum and blockade the signal transduction of muscarinic receptor pathway of contractile response. Amira et al. [52] reported that the six flavonoids (apigenin, genistein, quercetin, rutin, naringenin, and catechin) had an antispasmodic effect (at dose 30 μM) by regulating the regulation of the gastric tone of the stomach. Thus, the antispasmodic and antidiarrheal activity of Cm.EtOH may be attributed to the abundant presence of quercetin, epicatechin, rutin, and apigenin.

Diarrhea is characterized as abnormal expulsion of low consistency stool due to disturbance in electrolytes and water transport in the intestine. Castor oil induces changes in electrolyte and water transport in the intestine to cause diarrhea and increase peristaltic movements [48]. Our present study studied antidiarrheal, antiperistalsis, and fluid intestinal accumulation activities of Cm.EtOH. When Cm.EtOH was administered at 150 and 300 mg/kg, it significantly decreased peristalsis, diarrhea, and electrolyte imbalance. These antispasmodic properties of Cm.EtOH prevented charcoal meal from moving further due to its antiperistaltic effects. Cm.EtOH blocked the castor oil–induced diarrhea and fluid secretion in animals [49]. The antiperistalsis, antisecretory,

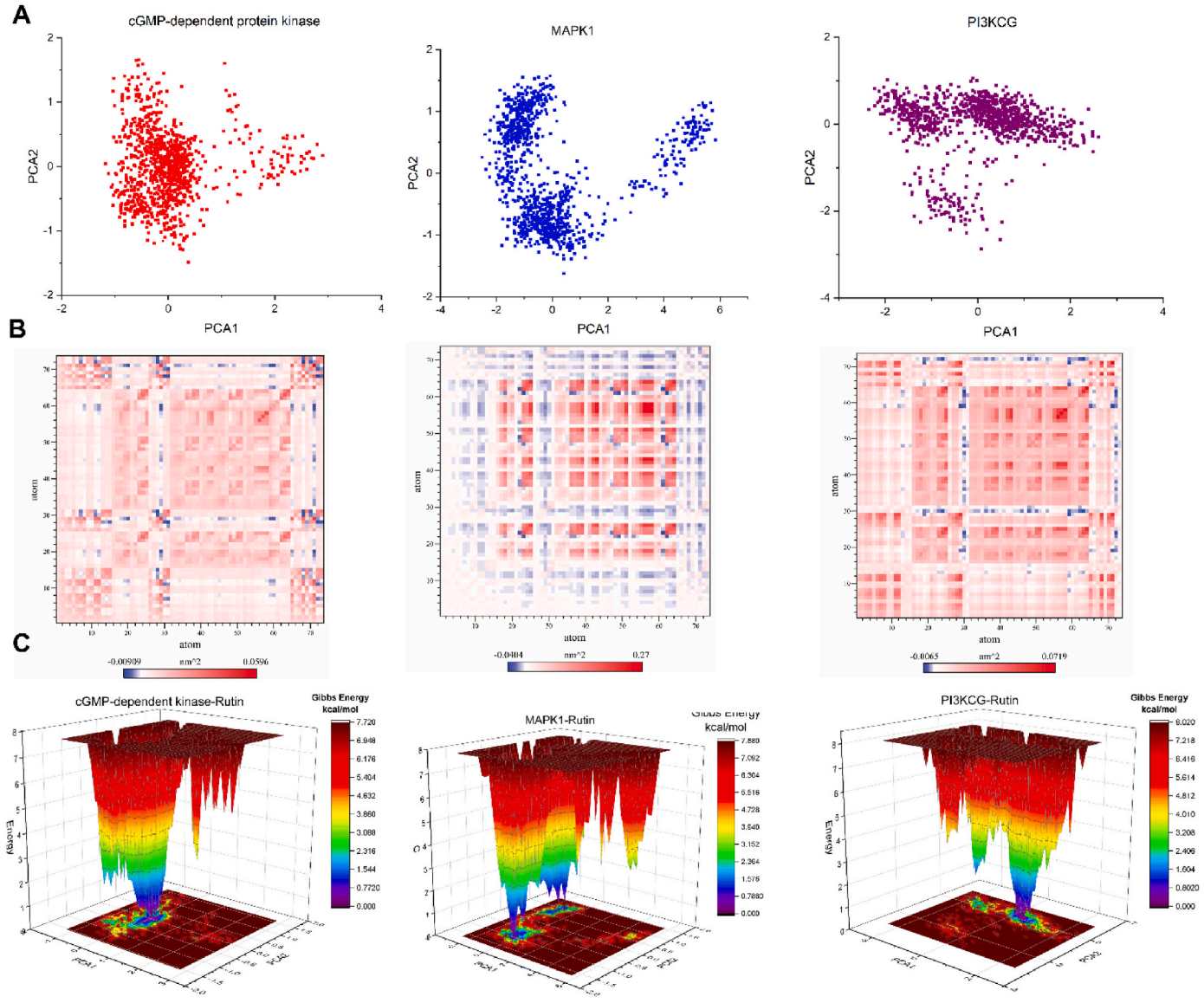

Fig. 21. Principal component analysis (PCA), Covariance, and free energy landscape (FEL) of cGMP-dependent protein kinase-Rutin, MAPK1-Rutin, and PI3KCγ-Rutin docked complexes for 10 ns. **A.** 2D PCA plots **B.** Covariance plots for residues of proteins. **C.** 3D FEL of docked complexes.

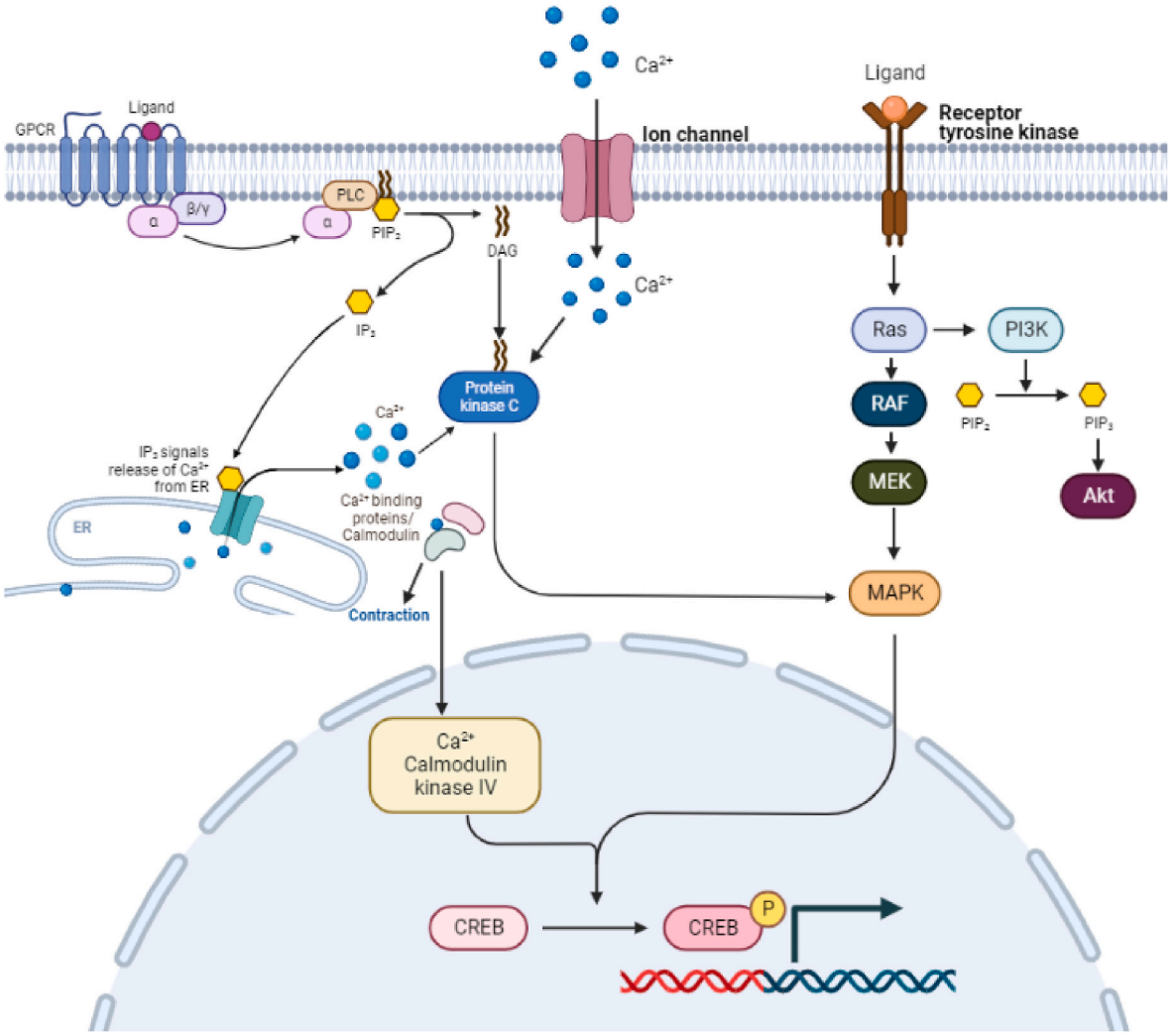

Fig. 22. Mechanistic insights of key genes calcium mediated smooth muscle contractions.

and antidiarrheal effects of Cm.EtOH was mediated by the involvement of calcium channel inhibition mechanisms like loperamide and verapamil [50,51]. Our findings indicate that *C. melo* seeds might be used to treat diarrhea and enhance D–IBS and feces indices. The calcium–mediated signaling pathway was responsible for the contribution of Cm.EtOH to intestinal motility. In addition, we discovered that Ca^{2+}/K^{+} ion channels suppress intestinal contraction through modulating Ca^{2+} and potassium chloride channels and costimulatory proteins. Our findings provide preliminary evidence to aid in elucidating the underlying treatment mechanism of Cm. EtOH for diarrhea and IBS–D.

5. Conclusion

An integrated approach of DEGs and WGCNA of IBS along with LC ESI MS/MS and HPLC analysis of *C. melo* was used in this study to identify (1) phytoconstituents and (2) probable regulatory genes network involved in calcium mediate smooth muscles. In conclusion, *C. melo* seeds exerted antispasmodic, antiperistaltic, antidiarrheal, dysuric, and antiasthmatic properties by modulating the contractile response via calcium–mediated signaling to the repolarize membrane action potential. Furthermore, the presence of rutin, kaempferol, quercetin, apigenin, and luteolin in Cm.EtOH may be regarded interesting bioactive substance. More research is needed to understand and corroborate the putative modes of action and pathways responsible for the medicinal benefits of *C. melo* seeds.

Funding

This research did not obtain any particular grant from the public, commercial, or not–for–profit funding agencies.

Ethical approval

Ethical approval was attained from the Ethical Committee Department of Pharmacology, Faculty of Pharmacy, Bahauddin Zakariya University, Multan (EC/04PhDL–S2018), dated March 26, 2018. Researchers agreed to use the approved informed consent documented before their enrolment into the study.

CRediT authorship contribution statement

Fatima Saqib and Muqeet Wahid: Conceptualization, Muqeet Wahid and Anam Ali: Methodology, Software, Software – original draft. Fatima Saqib and Saeed Akhtar: Writing – review & editing. Jesus Simal–Gandara and Trina Ekawati Tallei : Writing – review & editing.

Declaration of competing interest

The authors declare that they have no known competing financial interests or personal relationships that could have appeared to influence the work reported in this paper.

Acknowledgments

The author (s) are very thankful to folk healers from Punjab Province for sharing their knowledge regarding folkloric use. The author(s) are very thankful to the Chairman Department of Pharmacology, Dr. Imran, for the provision of animal houses and lab–related facilities. We would like to thank the funding for the open access charge: University of Vigo (Spain)/CISUG.

Appendix A. Supplementary data

Supplementary data to this article can be found online at https://doi.org/10.1016/j.compbiomed.2023.106596.

References

[1] B.E. Lacy, F. Mearin, L. Chang, W.D. Chey, A.J. Lembo, M. Simren, R. Spiller, Bowel disorders, Gastroenterology 150 (2016) 1393–1407.e5, https://doi.org/10.1053/J.GASTRO.2016.02.031.
[2] B.E. Lacy, J.C. Moreau, Diarrhea-predominant irritable bowel syndrome: diagnosis, etiology, and new treatment considerations, J. Am. Assoc. Nurse Pract. 28 (2016) 393–404, https://doi.org/10.1002/2327-6924.12387.
[3] D.J. Cangemi, B.E. Lacy, Management of irritable bowel syndrome with diarrhea: a review of nonpharmacological and pharmacological interventions, Therap. Adv. Gastroenterol. 12 (2019), 175628481987895, https://doi.org/10.1177/1756284819878950.
[4] J.A. Duke, Melon (Cucumis melo L.), in: Duke's Handb. Med. Plants Bible, CRC press, New York, 2008, pp. 148–151.
[5] M.A. Silva, T.G. Albuquerque, R.C. Alves, M.B.P.P. Oliveira, H.S. Costa, Melon (Cucumis melo L.) by-products: potential food ingredients for novel functional foods? Trends Food Sci. Technol. 98 (2020) 181–189, https://doi.org/10.1016/j.tifs.2018.07.005.
[6] A.A. Mariod, M.E. Saeed Mirghani, I. Hussein, Cucumis melo var. cantalupo Cantaloupe, Unconv. Oilseeds Oil Sources (2017) 107–111, https://doi.org/10.1016/b978-0-12-809435-8.00019-6.
[7] E. Erhirhie, N. Ekene, Medicinal values on Citrullus lanatus (Watermelon): pharmacological review, Int. J. Res. Pharm. Biomed. Sci. 4 (2014) 1305–1312.
[8] H.M. Asif, N. Akhtar, S. Sultana, S.U. Rehman, M. Akram, U.J. Rehman, Medicinal properties of Cucumis melo Linn, J. Pharm. Pharmaceut. Sci. 2 (2014) 58–62.
[9] S. Patel, A. Rauf, Edible seeds from Cucurbitaceae family as potential functional foods: immense promises, few concerns, Biomed. Pharmacother. 91 (2017) 330–337, https://doi.org/10.1016/j.biopha.2017.04.090.
[10] B. Salehi, E. Capanoglu, N. Adrar, G. Catalkaya, S. Shaheen, M. Jaffer, L. Giri, R. Suyal, A.K. Jugran, D. Calina, A.O. Docea, S. Kamiloglu, D. Kregiel, H. Antolak, E. Pawlikowska, S. Sen, K. Acharya, Z. Selamoglu, J. Sharifi-Rad, M. Martorell, C. F. Rodrigues, F. Sharopov, N. Martins, R. Capasso, Cucurbits plants: a key emphasis to its pharmacological potential, Molecules 24 (2019), https://doi.org/10.3390/molecules24101854.
[11] Y. Dixit, A. Kar, Protective role of three vegetable peels in alloxan induced diabetes mellitus in male mice, Plant Foods Hum. Nutr. 65 (2010) 284–289, https://doi.org/10.1007/s11130-010-0175-3.
[12] M. Wahid, F. Saqib, M. Qamar, Z.M. Ziora, Antispasmodic activity of the ethanol extract of Citrullus lanatus seeds: justifying ethnomedicinal use in Pakistan to treat asthma and diarrhea, J. Ethnopharmacol. 295 (2022), 115314, https://doi.org/10.1016/j.jep.2022.115314.
[13] M. Wahid, A. Ali, F. Saqib, A. Aleem, S. Bibi, K. Afzal, A. Ali, A. Baig, S.A. Khan, M. H.H. Bin Asad, Pharmacological exploration of traditional plants for the treatment of neurodegenerative disorders, Phyther. Res. 34 (2020) 3089–3112, https://doi.org/10.1002/ptr.6742.
[14] M. Wahid, F. Saqib, S. Akhtar, A. Ali, P. Wilairatana, M.S. Mubarak, Possible mechanisms underlying the antispasmodic, bronchodilator, and antidiarrheal activities of polarity–based extracts of Cucumis sativus L. Seeds in in silico, in vitro, and in vivo studies, Pharmaceuticals 15 (2022) 641, https://doi.org/10.3390/ph15050641.
[15] M. Wahid, F. Saqib, Scientific basis for medicinal use of Citrullus lanatus (Thunb.) in diarrhea and asthma: in vitro, in vivo and in silico studies, Phytomedicine 98 (2022), 153978, https://doi.org/10.1016/j.phymed.2022.153978.
[16] M. Wahid, F. Saqib, H.T. Ahmedah, C.M. Gavris, V. De Feo, M. Hogea, M. Moga, R. Chicea, Cucumis sativus l. Seeds ameliorate muscular spasm-induced gastrointestinal and respiratory disorders by simultaneously inhibiting calcium mediated signaling pathway, Pharmaceuticals 14 (2021) 1197, https://doi.org/10.3390/ph14111197.
[17] F. Saqib, K.H. Janbaz, Rationalizing ethnopharmacological uses of Alternanthera sessilis: a folk medicinal plant of Pakistan to manage diarrhea, asthma and hypertension, J. Ethnopharmacol. 182 (2016) 110–121, https://doi.org/10.1016/j.jep.2016.02.017.
[18] K.H. Janbaz, M. Zaeem Ahsan, F. Saqib, I. Imran, M. Zia-Ul-Haq, M. Abid Rashid, H.Z.E. Jaafar, M. Moga, Scientific basis for use of Pyrus pashia Buch.-Ham. ex D. Don. fruit in gastrointestinal, respiratory and cardiovascular ailments, PLoS One 10 (2015), e0118605, https://doi.org/10.1371/journal.pone.0118605.
[19] J.E. Hall, M.E. Hall, Excitation and contraction of smooth muscle, in: Guyt. Hall Textb. Med. Physiol., fourteenth ed., Elsevier Health Sciences, 2020, pp. 101–109.
[20] F. Saqib, K.H. Janbaz, Ethnopharmacological basis for folkloric claims of Anagallis arvensis Linn. (Scarlet Pimpernel) as prokinetic, spasmolytic and hypotensive in province of Punjab, Pakistan, J. Ethnopharmacol. 267 (2021), 113634, https://doi.org/10.1016/j.jep.2020.113634.
[21] S.E. Elasoru, P. Rhana, T. de Oliveira Barreto, D.L. Naves de Souza, J.E.R. Menezes-Filho, D.S. Souza, M.V. Loes Moreira, M.T. Gomes Campos, O.T. Adedosu, D. Roman-Campos, M.M. Melo, J.S. Cruz, Andrographolide protects against isoproterenol-induced myocardial infarction in rats through inhibition of L-type Ca2+ and increase of cardiac transient outward K+ currents, Eur. J. Pharmacol. 906 (2021), 174194.
[22] V. Chauhan, M.P. Singh, Immuno-informatics approach to design a multi-epitope vaccine to combat cytomegalovirus infection, Eur. J. Pharmaceut. Sci. 147 (2020), 105279, https://doi.org/10.1016/j.ejps.2020.105279.
[23] Z. Yu, L. Kang, W. Zhao, S. Wu, L. Ding, F. Zheng, J. Liu, J. Li, Identification of novel umami peptides from myosin via homology modeling and molecular docking, Food Chem. 344 (2021), 128728, https://doi.org/10.1016/j.foodchem.2020.128728.
[24] S. Subhani, A. Jayaraman, K. Jamil, Homology modelling and molecular docking of MDR1 with chemotherapeutic agents in non-small cell lung cancer, Biomed. Pharmacother. 71 (2015) 37–45, https://doi.org/10.1016/j.biopha.2015.02.009.
[25] M.S. Valdés-Tresanco, M.E. Valdés-Tresanco, P.A. Valiente, E. Moreno, Gmx_MMPBSA: a new tool to perform end-state free energy calculations with GROMACS, J. Chem. Theor. Comput. 17 (2021) 6281–6291, https://doi.org/10.1021/ACS.JCTC.1C00645/SUPPL_FILE/CT1C00645_SI_001.PDF.
[26] H. Sirous, G. Chemi, G. Campiani, S. Brogi, An integrated in silico screening strategy for identifying promising disruptors of p53-MDM2 interaction, Comput. Biol. Chem. 83 (2019), https://doi.org/10.1016/j.compbiolchem.2019.107105.
[27] B. Kuhn, P.A. Kollman, Binding of a diverse set of ligands to avidin and streptavidin: an accurate quantitative prediction of their relative affinities by a combination of molecular mechanics and continuum solvent models, J. Med. Chem. 43 (2000) 3786–3791, https://doi.org/10.1021/jm000241h.
[28] Q. Yang, B. Li, J. Tang, X. Cui, Y. Wang, X. Li, J. Hu, Y. Chen, W. Xue, Y. Lou, Y. Qiu, F. Zhu, Consistent gene signature of schizophrenia identified by a novel feature selection strategy from comprehensive sets of transcriptomic data, Briefings Bioinf. 21 (2020) 1058–1068, https://doi.org/10.1093/bib/bbz049.
[29] J. Fu, Y. Zhang, Y. Wang, H. Zhang, J. Liu, J. Tang, Q. Yang, H. Sun, W. Qiu, Y. Ma, Z. Li, M. Zheng, F. Zhu, Optimization of metabolomic data processing using NOREVA, Nat. Protoc. 17 (2022) 129–151, https://doi.org/10.1038/s41596-021-00636-9.
[30] N. Dong, C. Xue, L. Zhang, T. Zhang, C. Wang, C. Bi, A. Shan, Oleanolic acid enhances tight junctions and ameliorates inflammation in Salmonella typhimurium -induced diarrhea in mice via the TLR4/NF-κB and MAPK pathway, Food Funct. 11 (2020) 1122–1132, https://doi.org/10.1039/C9FO01718F.
[31] M.A. McGuckin, R. Eri, L.A. Simms, T.H.J. Florin, G. Radford-Smith, Intestinal barrier dysfunction in inflammatory bowel diseases, Inflamm. Bowel Dis. 15 (2009) 100–113, https://doi.org/10.1002/IBD.20539.
[32] C.P.R. Xavier, C.F. Lima, M. Fernandes-Ferreira, C. Pereira-Wilson, in: Salvia Fruticosa, Salvia Officinalis, and Rosmarinic Acid Induce Apoptosis and Inhibit Proliferation of Human Colorectal Cell Lines: the Role in MAPK/ERK Pathway, vol. 61, 2009, pp. 564–571, https://doi.org/10.1080/01635580802710733, 10.1080/01635580802710733.
[33] A.L. Hopkins, Network pharmacology, Nat. Biotechnol. 25 (2007) 1110–1111, https://doi.org/10.1038/nbt1007-1110.
[34] G.B. Zhang, Q.Y. Li, Q.L. Chen, S.B. Su, Network pharmacology: a new approach for Chinese herbal medicine research, Evidence-Based Complement, Altern. Med. 2013 (2013), https://doi.org/10.1155/2013/621423.
[35] M. Park, S.Y. Park, H.J. Lee, C.E. Kim, A Systems-level analysis of mechanisms of Platycodon grandiflorum based on a network pharmacological approach, Molecules 23 (2018) 2841, https://doi.org/10.3390/molecules23112841.
[36] L. Zhong, X. Hou, Pathophysiologic findings of irritable bowel syndrome in China, J Neurogastroenterol Motil 18 (2012) 19–33, https://doi.org/10.5056/JNM.2012.18.1.19.
[37] M. Jia, X. Lu, Z. Wang, L. Zhao, S. Zhang, Effects of fengliao-changweikang in diarrhea-predominant irritable bowel syndrome rats and its mechanism involving colonic motility, J. Neurogastroenterol. Motil. 24 (2018) 479, https://doi.org/10.5056/JNM17093.
[38] K.A. Sharkey, W.K. MacNaughton, Gastrointestinal motility and water flux, emesis, and biliary and pancreatic disease, in: L.L. Brunton, R. Hilal-Dandan, B. C. Knollmann (Eds.), Goodman Gilman's Pharmacol. Basis Ther., thirteenth ed., McGraw-Hill, New York, NY, USA, 2018, pp. 921–944. https://accesspharmacy.mhmedical.com/content.aspx?sectionid=102162555&bookid=1613. (Accessed 3 July 2021). accessed.
[39] J.L. Wallace, K.A. Sharkey, Pharmacotherapy of gastric acidity, peptic ulcers, and gastroesophageal reflux disease, in: L.L. Brunton, R. Hilal-Dandan, B.C. Knollmann (Eds.), Goodman Gilman's Pharmacol. Basis Ther., thirteenth ed., McGraw-Hill, New York, NY, USA, 2018, pp. 1309–1322.
[40] A.H. Gilani, A.U. Khan, M. Raoof, M.N. Ghayur, B.S. Siddiqui, W. Vohra, S. Begum, Gastrointestinal, selective airways and urinary bladder relaxant effects of Hyoscyamus Niger are mediated through dual blockade of muscarinic receptors and Ca2+ channels, Fundam. Clin. Pharmacol. 22 (2008) 87–99, https://doi.org/10.1111/j.1472-8206.2007.00561.x.
[41] A.H. Gilani, M.N. Ghayur, Z.S. Saify, S.P. Ahmed, M.I. Choudhary, A. Khalid, Presence of cholinomimetic and acetylcholinesterase inhibitory constituents in

betel nut, Life Sci. 75 (2004) 2377–2389, https://doi.org/10.1016/j.lfs.2004.03.035.
[42] A.H. Gilani, Q. Jabeen, M.N. Ghayur, K.H. Janbaz, M.S. Akhtar, Studies on the antihypertensive, antispasmodic, bronchodilator and hepatoprotective activities of the Carum copticum seed extract, J. Ethnopharmacol. 98 (2005) 127–135, https://doi.org/10.1016/j.jep.2005.01.017.
[43] F. Vogalis, Potassium channels in gastrointestinal smooth muscle, J. Auton. Pharmacol. 20 (2000) 207–219, https://doi.org/10.1046/J.1365-2680.2000.00183.X.
[44] A.H. Gilani, A. ullah Khan, M.N. Ghayur, Ca2+ antagonist and cholinergic activities explain the medicinal use of olive in gut disorders, Nutr. Res. 26 (2006) 277–283, https://doi.org/10.1016/j.nutres.2006.06.009.
[45] M.H. Mehmood, N. Anila, S. Begum, S.A. Syed, B.S. Siddiqui, A.H. Gilani, Pharmacological basis for the medicinal use of Carissa carandas in constipation and diarrhea, J. Ethnopharmacol. 153 (2014) 359–367, https://doi.org/10.1016/j.jep.2014.02.024.
[46] E. Miyazaki, H. Yabu, S. Sunano, Excitation and contraction of the smooth muscle, Jpn. J. Smooth Muscle Res. 7 (1971) 83–97, https://doi.org/10.1540/jsmr1965.7.83.
[47] K.H. Janbaz, M. Nisa, F. Saqib, I. Imran, M. Zia-Ul-Haq, V. De Feo, Bronchodilator, vasodilator and spasmolytic activities of methanolic extract of Myrtus communis L, J. Physiol. Pharmacol. 64 (2013) 479–484. http://www.ncbi.nlm.nih.gov/pubmed/24101394.
[48] G.A. Agbor, F. Longo, E.A. Makong, P.A. Tarkang, Evaluation of the antidiarrheal and antioxidant properties of Justicia hypocrateriformis, Pharm. Biol. 52 (2014) 1128–1133, https://doi.org/10.3109/13880209.2013.879189.
[49] M.T. Yakubu, S.S. Salimon, Antidiarrhoeal activity of aqueous extract of Mangifera indica L. leaves in female albino rats, J. Ethnopharmacol. 163 (2015) 135–141, https://doi.org/10.1016/j.jep.2014.12.060.
[50] I.J. Reynolds, R.J. Gould, S.H. Snyder, Loperamide: blockade of Calcium channels as a mechanism for antidiarrheal effects, J. Pharmacol. Exp. Therapeut. 231 (1984) 628–632. http://www.ncbi.nlm.nih.gov/pubmed/6502516. (Accessed 12 May 2020). accessed.
[51] A. Crowe, P. Wong, Potential roles of P-gp and calcium channels in loperamide and diphenoxylate transport, Toxicol. Appl. Pharmacol. 193 (2003) 127–137, https://doi.org/10.1016/S0041-008X(03)00372-7.
[52] S. Amira, A. Rotondo, F. Mulè, Relaxant effects of flavonoids on the mouse isolated stomach: Structure-activity relationships, Eur. J. Pharmacol. 599 (2008) 126–130. https://doi.org/10.1016/j.ejphar.2008.09.021.